EFFECT OF SURFACE TENSION ON DEFORMATION OF SOFT SOLIDS

A Dissertation

Presented to the Faculty of the Graduate School

of Cornell University

in Partial Fulfilment of the Requirements for the Degree of

Doctor of Philosophy

by

Xuejuan Xu

May 2016

EFFECT OF SURFACE TENSION ON DEFORMATION IN SOFT SOLIDS

Xuejuan Xu, Ph.D.

Cornell University 2016

Classical continuum mechanics often neglects the contribution of interfaces to the deformation of solids. This is usually reasonable for stiff (e.g. crystalline) materials, whose elastic energy of the bulk almost always overwhelms contributions from the surface except for very small objects that are hardly measurable. However, for compliant materials such as elastomers and hydrogels, solid surface tension can play an important role in either driving or resisting their deformation at relatively large length scale that is well within the continuum description. With applications ranging from MEMS (Micro-Electro-Mechanical System) to drug delivery, from soft robotics to biomimetic systems, it is of great technological significance to understand the underlying mechanisms of the deformation in these compliant elastomers and gels in a quantitative manner. It is for this reason, we attempt to develop theoretical and numerical models to capture the coupled effect of surface tension and elasticity in deformation of compliant solids.

In this dissertation, I present our theoretical and experimental understanding of the effect of surface tension as it applies to a variety of phenomena involving deformation of compliant solids. Chapter 1 constructs a deformation map in which shape change of an elastic solid is captured by two dimensionless material parameters with a simple scaling argument. To enable accurate predictions, a finite element modelling technique, which incorporates surface tension effect, is used to quantify the shape change of a free standing elastic solid circular cylinder driven by both gravity and surface tension.

Chapter 2 and 3 outline two independent approaches of measuring surface tension of a solid by monitoring its deformation. Chapter 2 describes a method that is applicable to materials with a low moduli (less than 100 kPa). We mould gelatine against patterned master surfaces. The sharp features on gel surface are rounded compared to the master and can be significantly flattened upon demoulding. We model this phenomenon using finite element technique as an elastic deformation driven by surface stress, and thus estimate the values of the solid-air surface tension of these gels. It is however limited when apply this method to stiffer materials, for the bulk elasticity in these materials often dominates the deformation. An alternative technique of surface tension measurement described in Chapter 3 is specifically designed for not-so-compliant materials with moduli larger than 100 kPa. A thin solid film is deflected with a rigid indenter and its deflection can be modelled using a version of nonlinear von Karman plate theory incorporating surface tension. We apply this method to polydimethylsiloxane (PDMS) and obtained a value of its surface tension consistent with that reported in the literature.

Chapter 4，5 and 6 study the mechanics of contact and adhesion between solids, in which classical theories are extended to include surface tension of the solid surfaces outside the contact region. Chapter 4 models the adhesive contact between an elastic half-space and a rigid sphere in the absence of external load. We present a finite element solution of such a problem, which shows the transition between classical Johnson-Kendall-Roberts (JKR) deformation and surface-tension-dominant deformation. Chapter 5 extends the problem to include non-zero external load as well as non-adhesive contact. Besides the contact configuration of a rigid sphere and elastic half space, we also simulate contact between an elastic sphere and rigid plates. Both frictionless and no slip contacts are modelled and the results are compared to provide some insights on the effect of interface conditions. We also assess the validity of *Hui et al.*'s (2015) small-strain theory on

contact of soft solids, which includes surface tension effect, in large deformation regime. Chapter 6 focuses on modelling the surface displacement of the elastic substrate when being indented by a rigid sphere. Using the same FEM model from the previous two chapters, we compare the modelled surface profile of the substrate to an experiment performed by Jensen *et al.* (2015).

Chapter 7 lists some suggestions for future work.

BIOGRAPHICAL SKETCH

Originally from Shijiazhuang, China, Xuejuan Xu (known as Snow by many) attended high school in Singapore and did her undergraduate study at Trinity College of the University of Oxford in England. She received a Master degree in Engineering, Economics and Management from Oxford in 2010. She expects to complete her Ph.D. in Mechanical Engineering at Cornell University in May 2016. Upon completion of her study at Cornell, Xuejuan Xu will begin to work as a Senior Research Engineer at Saint-Gobain North America.

To My Parents

献给我的父母，我爱你们

ACKNOWLEDGEMENTS

I wish to express my immeasurable appreciation and deepest gratitude to my advisor, Prof. Chung-Yuen Hui, who has a genius mind and a good taste for life. I have been continually inspired and in awe of his curiosity in regard to research and commitment in regard to teaching. Without his guidance and support, this dissertation would not have been possible.

My dissertation committee guided me through all these years. I would like to thank Prof. Anand Jagota, who helped me immensely in all aspects of my research, especially in finite element modelling and experimental works. His keen attention to details and observant attitude towards experiments always kept me wanting to investigate deeper into my projects. Thank you to Prof. Paul Steen and Prof. Alan Zehnder for being my minor advisors and for giving me insightful suggestions along the way. Prof. Steen taught me "Analysis of Nonlinear Systems: Stability, Bifurcation, and Continuation" and Prof. Zehnder taught me "Fracture Mechanics". The knowledge and analytical skills I learned from both courses are indispensable to my research.

In addition, a thank you to all my collaborators over the years, Professor Dan Luo, Professor Eric Dufresne and Prof. Manoj Chaudhury. Their experimental work provided inspiration to my projects. I would also like to thank my co-authors, Prof. Mingming Wu, Dr. Songming Peng, Dr. Dadhichi Paretkar, Dr Nichole Nadermann and Tianshu Liu, for sharing my research path with me.

I am grateful to all my group mates, Abhishek Srivastava, Xinzeng Feng, Jing Ning, Rong Long, Pankaj Singh, Tianshu Liu and Jingyi Guo. It was a great pleasure working with them and I appreciate their ideas, support and good humour.

TABLE OF CONTENTS

CHAPTER 1: GRAVITY AND SURFACE TENSION EFFECTS ON SHAPE CHANGE OF SOFT MATERIALS **1**

1.1 Introduction 2
1.2 Deformation Map 5
1.3 Example of a Deformation Map 10
1.4 Results 12
1.5 Conclusion and Discussion 23
Acknowledgement 25
Appendix 1.1 Analytical Calculations in Gravity Regime 25
Appendix 1.2 Finite Element Simulation of Surface Tension Effect 28
Appendix 1.3 Calculations in Gravity and Surface Tension Dual Action Regime 33
References 35

CHAPTER 2: FLATTENING OF A PATTERNED COMPLIANT SOLID BY SURFACE STRESS **37**

2.1 Introduction 38
2.2 Experimental 40
2.3 Results 42
2.4 Discussion and Conclusions 53
Acknowledgements 56
Appendix 2 Supplementary Information 56
References 63

CHAPTER 3: SURFACE TENSION MEASUREMENT FROM INDENTATION OF CLAMPED THIN FILMS **66**

3.1 Introduction 67
3.2 Experiments 69
3.3 Numerical Model 71
3.4 Results and Discussion 76
Acknowledgement 79
Appendix 3.1 Supplementary Information 79
Appendix 3.2 Energy Release Rate of the Indented Circular Film 84
Appendix 3.3 Deflection of a Pre-Tension Circular Film due to a Liquid Drop 87
References 96

CHAPTER 4: EFFECT OF SURFACE TENSION ON THE ADHESIVE CONTACT OF A RIGID SPHERE TO A COMPLIANT SUBSTRATE **100**

4.1 Introduction 101

4.2 Dimensional Analysis and the Two Limits 106
4.3 Finite Element Model 108
4.4 Finite Element Results 111
4.5 Approximate Formula for Deformation 116
4.6 Conclusion 118
Acknowledgements 121
Appendix 4 Supplementary Information 121
References 123

CHAPTER 5: EFFECTS OF SURFACE TENSION AND LARGE DEFORMATION ON CONTACT OF SOFT SOLIDS **126**
5.1 Introduction 127
5.2.1 Finite Element Model 130
5.2.2 FEM Results: Non-Adhesive Contact 135
5.2.3 FEM Results: Adhesive Contact 144
5.3 Conclusions and Discussion 155
Acknowledgement 158
Appendix 5 Review of Hui et al.'s Small Strain Theory (SST) 158
References 161

CHAPTER 6: SURFACE DEFORMATION OF AN ELASTIC SUBSTRATE IN CONTACT WITH A RIGID SPHERE: EFFECT OF SURFACE TENSION AND LARGE DEFORMATION **164**
6.1 Introduction 165
6.2 Finite Element Model 168
6.3 Results 174
6.4 Discussion 177
Acknowledgements 178
Appendix 6 Supplementary Information 178
References 181

CHAPTER 7: RECOMMENDATION FOR FUTURE WORK **183**

LIST OF FIGURES

Figure 1.1	Shape change of a DNA meta-hydrogel cylinder.	4
Figure 1.2	The deformation map.	8
Figure 1.3	Referential undeformed configuration.	10
Figure 1.4	Results for gravity dominant regime using a neo-Hookean model.	15
Figure 1.5	Results for surface tension dominant regime.	18
Figure 1.6	Results for gravity and surface tension dual action regime.	20
Figure 1.7	Results for gravity, surface tension and elasticity triple action regime.	22
Figure A.1.1.1	Referential undeformed configuration of a soft solid placed on a rigid substrate.	27
Figure A.1.1.2	Plot of normal stretch ratio λ against normalized vertical coordinate z.	27
Figure A.1.2.1	Mesh selection of the FE model.	29
Figure A.1.2.2	A schematic diagram of two 2-node surface elements.	30
Figure A.1.2.3	Deformation of a soft solid in surface tension dominant regime.	33
Figure A.1.3.1	Current deformed configuration of a soft solid under gravity and surface tension.	34
Figure 2.1	(a) SEM image of a typical PDMS master periodic ridge geometry; (b) Schematic of the periodic ridge geometry.	39
Figure 2.2	(a) Measured 3D surface profile of periodic ridge geometry showing PDMS master and its gel replica; (b) Line scans of the PDMS and gel surface profiles; (c-d) Final gel height compared to (initial) PDMS.	43
Figure 2.3	Prediction of final shape of the gel profile based on eq. (2.8) for a low height periodic ridge geometry.	48
Figure 2.4	Deformed configuration of a typical demoulded gel sample predicted by FEM simulation.	50
Figure 2.5	Simulation results for the shape deformation of the high height periodic ridge geometry.	51
Figure 2.6	(a) Line scans across measured surface profile of periodic ridge geometry for PDMS master and its gel replica and predicted shape for the PDMS and gel profiles by FEM; (b) Measured reduction in gel height as a function of elastic moduli and periodic separations.	52
Figure A.2.1	Schematic of flat cylindrical punch with diameter $2a$ used to indent a gel block of height h and diameter L.	57
Figure A.2.2	Load measured as a function of indentation depth (Distance) in a typical contact compliance test.	58
Figure A.2.3	(a) Picture of a gel beam fixed at one end and freely hanging on the other; (b) Integral of moment versus angle plot.	60
Figure A.2.4	Optical micrographs of gel filled PDMS master prior to moulding.	61
Figure A.2.5	Measured initial height of ridge/channel in PDMS and the corresponding gel height for three different periodic spacing and five different moduli.	61

Figure A.2.6	Measured reduction in gel height and FEM analysis based least square fits for the height reduction as a function of varying elastic moduli and three different periods.	62
Figure A.2.7	Comparison of deformed heights for a given surface tension for the neo-Hookean versus linear elastic material models.	63
Figure 3.1	(a) A schematic of the side view of the experimental setup; (b) Profile of the top surface of a film deflected by a spherical glass indenter; (c) Deflections at points of equal distance from the sphere centre are averaged and plotted versus the distance.	70
Figure 3.2	The axisymmetric von Karman thin plate theory is used to model the film outside contact. Geometric parameters at the contact line are defined on the left.	72
Figure 3.3	Fitting the deflections of the thinnest film for different indentation depths.	75
Figure 3.4	Extrapolation of film pre-tension to zero Eh value yields twice the surface tension of PDMS.	77
Figure A.3.2.1	Schematic figure of a pre-stretched thin elastic solid film deflected by a rigid indenter.	85
Figure A.3.3.1	Schematic figure of a liquid drop hanging underneath a pre-stretched thin elastic solid film	88
Figure A.3.3.2	Figures of force balance	90
Figure 4.1	(a) A rigid sphere is brought into contact with an elastic half-space; (b) The deformed configuration when the modulus of the half-space is vanishingly small.	105
Figure 4.2	(a) Deformation of the half-space near the contact region after each loading step in a simulation with $\sigma/\mu R$=1, $P/\mu R^2 = 10$; (b) The loading curve corresponding to steps 2 and 3.	109
Figure 4.3	(a) $\sigma/\mu R$=0. Plots of indentation depth and contact radius against the work of adhesion; (b) $\sigma/\mu R$=50. Plots of indentation depth and contact radius against the ratio of work of adhesion to surface tension.	112
Figure 4.4	(a) Indentation depth δ/R is plotted against $W_{ad}/\mu R$ at W_{ad}/σ=1. (b-c) Deformed surface profiles in simulations of the same contact area at three different $\sigma/\mu R$.	114
Figure 4.5	Experimental results are fitted by interpolating the results of FEM simulations.	116
Figure 4.6	Normalized indentation depth and contact radius are plotted against normalized work of adhesion.	118
Figure A.4.1	The surfaces of indentation depth and contact radius are interpolated over a grid of ($W_{ad}/\mu R$, W_{ad}/σ).	122
Figure 5.1	Geometries of finite element models	131

Figure 5.2	Deformation of the elastic parts after each loading step in a simulation with α=1	134
Figure 5.3	Results of non-adhesive contact: normalized load versus a_H/R with varied elasto-capillary number α.	138
Figure 5.4	Results of non-adhesive contact: normalized indentation depth versus a_H/R with varied elasto-capillary number α.	140
Figure 5.5	Results of non-adhesive contact: normalized load versus β.	142
Figure 5.6	Results of non-adhesive contact: normalized indentation depth is plotted against β.	144
Figure 5.7	FEM results of adhesive contact are compared to JKR theory and Lin & Chen's results: normalized load versus normalized contact radius.	146
Figure 5.8	Results of adhesive contact at α=1: normalized energy release rate versus normalized contact radius.	149
Figure 5.9	Results of adhesive contact at zero load: normalized energy release rate versus normalized contact radius.	151
Figure 5.10	Results of adhesive contact at normalized load of -1: normalized energy release rate versus normalized contact radius.	153
Figure 5.11	Results of adhesive contact: normalized contact radius versus normalized load in systems with varied ω.	155
Figure 6.1	(a) Schematics of Jensen et al.'s experiments. (b) A close-up view of the contact line.	168
Figure 6.2	Deformed surface after each step in a simulation with α=0.6.	169
Figure 6.3	FEM results of the deformed substrate surface profiles at various values of the elasto-capillary number α at a/R=0.75 and δ/R=0.31.	170
Figure 6.4	FEM deformed substrate surface profiles at α=0.6. The normalized contact radius is varied at ±5% of a/R=0.75	172
Figure 6.5	FEM results of the deformed substrate surface profiles at α=0.6 and a/R=0.75. The sphere displacement is varied ±5% of δ/R=0.31.	173
Figure 6.6	Comparison of the deformed surface profiles predicted by JKR theory without surface tension, Hui et al.'s small strain modified JKR theory with surface tension, FEM with neo-Hookean material at α = 0, FEM with neo-Hookean material at α = 0.6 as well as FEM with Ogden material at α = 0.6.	175
Figure A.6.1	Plot of normalized stress against stretch ratio in a uniaxial tensile test of the 2nd order Ogden model.	179
Figure A.6.2	Normalized mean curvatures as a function of normalized arc length of the FEM results at a/R = 0.75 and δ/R = 0.31	180

LIST OF TABLES

Table 2.1	Dimensions (with standard deviations) of periodic ridge geometry. For the case of lower height ridges (h ~1.7 and 2.7 μm) the width was not measured separately but was estimated in the model as half of the mean period.	40

CHAPTER 1

GRAVITY AND SURFACE TENSION EFFECTS ON SHAPE CHANGE OF SOFT MATERIALS*

Abstract

Surface tension and gravity, whose influence on deformation of conventional engineering materials is negligible, become important for soft materials that are typically used in micro-fabrication of devices such as micro-fluidic channels. Although for soft materials the shape change due to these forces can be large, it is often neglected in the design processes. To capture conditions under which the influence of these forces is important, we propose a deformation map in which shape change is captured by two dimensionless material parameters. Our idea is demonstrated by simulating the large deformation of a short circular cylinder made of a neo-Hookean material in frictionless contact with a rigid substrate. These simulations are carried out using a finite element model which accounts for surface tension and gravity. Our model integrates the two different approaches typically used to determine the shape change of solids and liquid drops in contact with a substrate.

---

* Xu, X., Jagota, A., Peng, S., Luo, D., Wu, M. and Hui, C.Y. (2013) *Langmuir*, 29(27):8665-8674.

1.1 Introduction

Soft materials such as elastomers and hydrogels can support very large deformation and play an increasingly important role in engineering applications. Polydimethylsiloxane (PDMS), for example, is often used for stamps in micro- and nano-printing for its low surface energy, transparency and elasticity [1]. It can also be used as a mold to transfer or replicate surface patterns from hard substrates. Such pattern transfer is important for many applications such as microfluidic devices [2] and bio-inspired adhesives [3]. A different class of soft materials are hydrogels, which are essentially polymer networks swollen in water. The biocompatibility of many hydrogels and their ability to respond to environmental stimuli make them attractive candidates for many biological and engineering applications such as bio-separation, drug delivery and tissue scaffolding [4].

The Young's modulus of most elastomers is on the order of megapascals. For hydrogels, this number ranges from hundreds to thousands of pascals. Most notably, recent development in synthetic hydrogels has led to the creation of a highly stretchable DNA hydrogel ('metagel') with a modulus on the order of only a few pascals [5]. Traditionally, engineering analysis of the deformation of solids neglects the influence of surface tension and gravity [a]. In his article on surface tension, Gibbs [6] in 1876 stated that 'the rigidity of solids is in general so great, that any tendency of the surfaces of discontinuity to variation in area or form may be neglected in comparison with the forces which are produced in the interior of solids by any sensible strains, so

[a] Gravity loading is important for very large structures such as buildings and dams.

that it is not necessary to take account of the surface of discontinuity in determining the state of strain of solid masses'. However, for very soft materials, surface tension can be the dominant driving force of shape change. Fig. 1.1a shows the image of a DNA meta-hydrogel in water after being released from its cylindrical mold. Since the gel consists mostly of water, the loading due to gravity and surface tension is relatively small when the gel is submerged in water and therefore it retains its (cylindrical) shape. However, when water is drained from the container, it immediately deforms to a pancake shape by the dual action of gravity and surface tension - its original shape is unrecognizable (Fig. 1.1b). Remarkably, because of its elasticity, it recovers to its original shape in Fig. 1.1c-1.1f when water is reintroduced. This "memory effect" is due to elasticity and not to changes in microstructure. A less dramatic example of surface induced shape change can be found in micro-fabrication of PDMS stamps. The corners of PDMS stamps release from silicon molds are never as sharp as the molds, suggesting that surface tension has caused the rounding of these corners [1]. Recently, Jagota *et al.* [7] have shown that a gel-replica of a rippled PDMS master has much reduced amplitude (about 60% reduction). The influence of liquid surface tension on the deformation of solids has been studied extensively in recent years [8]. An important example is the deformation of a substrate due to forces at the triple line of a drop on a substrate [9], where the additional role of solid-fluid surface tension has recently been established [10]. Clearly, the role of surface tension and gravity on the shape of structures will become more significant as the modulus decreases [11 12].

Perhaps the most familiar phenomenon that demonstrates surface tension in liquids is the shape of a pendant drop [13], which the theory of capillary allows us to compute in terms of two forces: gravity

and surface tension. As a solid becomes increasingly compliant, a natural question arises: how do gravity and surface tension control the shape of soft materials? That is the subject of this chapter.

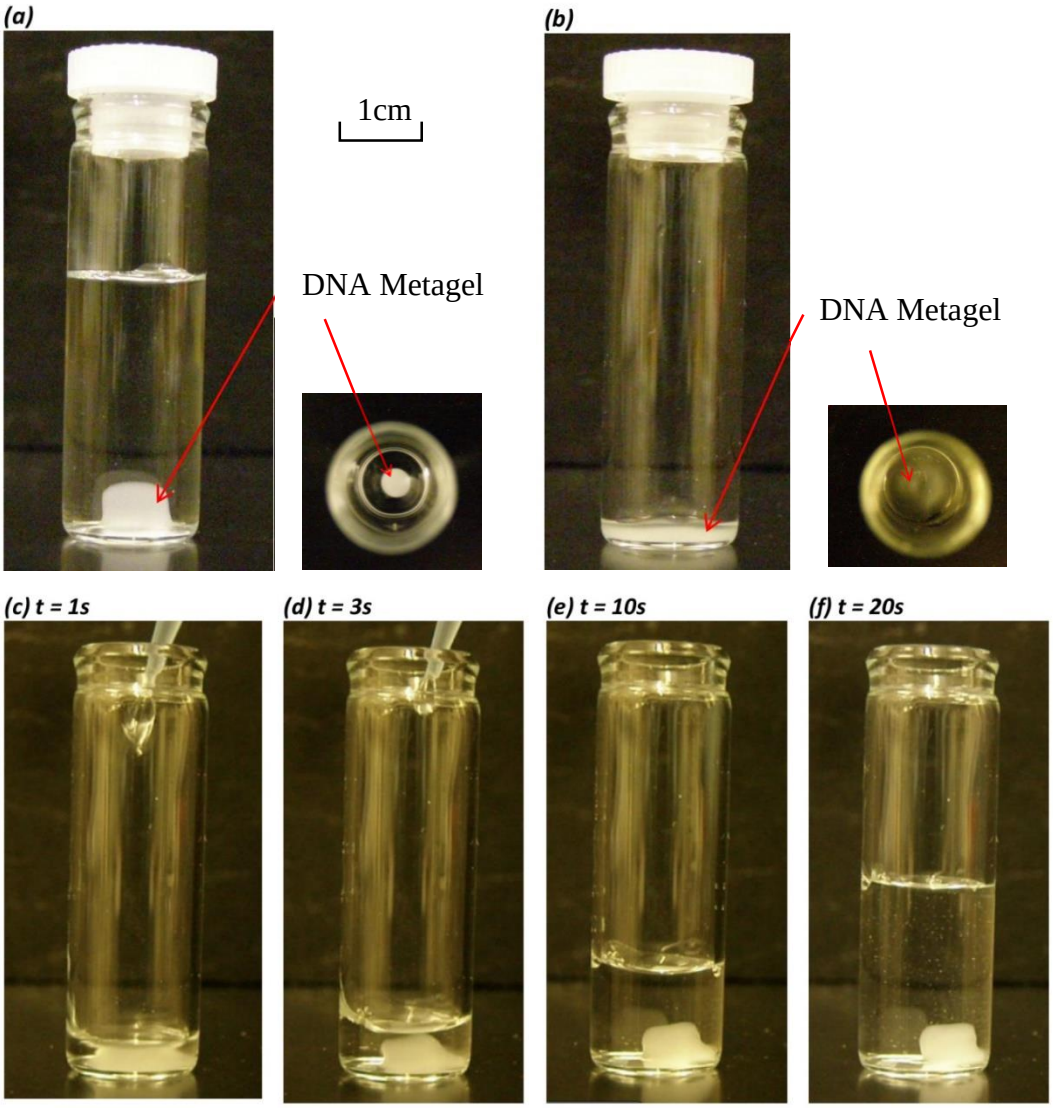

Figure 1.1 Shape Change of a DNA Meta-Hydrogel Cylinder. (a), Side- and top-views of a cylindrical shape hydrogel placed in a glass container submerged in water; (b), side- and top-views of the cylindrical shape hydrogel deformation after water has been extracted within seconds; (c) – (f), time sequence of images of the hydrogel in (b), as water is reintroduced to the glass container at $t=0$, the hydrogel recovers to its original cylindrical shape in less than 20 seconds. The characteristic time for swelling of the gel sample is on the order of hours; hence the shape recovery is due to elasticity of the hydrogel network.

1.2 Deformation Map

Because a liquid has no natural configuration, the shape of a liquid drop in contact with a solid substrate is determined by its volume and the energies of the three interfaces, liquid-vapor, solid-liquid, and solid-vapor. The equilibrium shape is the one that minimizes free energy, which has contributions only from surface energy terms. For a solid, however compliant, one must additionally specify a reference unstressed configuration for the body as well as the elastic properties of the solid. In this chapter, we assume that our soft solid is incompressible, isotropic and hyperelastic. The assumption of hyperelasticity implies the existence of a strain energy density function W and allows for arbitrary large deformation. The strain energy density W of an isotropic incompressible material has the form [14]:

$$W = \mu\varphi(I_1, I_2) \tag{1.1}$$

where φ is a dimensionless function of its dimensionless arguments I_1 and I_2, which are scalar invariants of the deformation gradient tensor, and μ is the small strain shear modulus. Specifically,

$$I_1 = \sum_{i=1}^{3} \lambda_i^2, \qquad I_2 = \lambda_1^2\lambda_2^2 + \lambda_1^2\lambda_3^2 + \lambda_2^2\lambda_3^2 \tag{1.2}$$

where λ_i 's are the principal stretch ratios. The simplest example is an ideal rubber or a neo-Hookean solid, where

$$\phi(I_1, I_2) = \mu(I_1 - 3)/2 \tag{1.3}$$

In the following, for simplicity, we shall assume that the dimension of our soft material is characterized by d. For example, the solid can be a sphere of radius d, or a cube with sides d or a

long slab with height d etc. Let γ denote the surface tension of the soft solid and ρ denote its mass density. Imagine that the solid is formed by pouring a liquid into a mold followed by its gelation or cross-linking into a solid. The reference configuration of the soft material is determined by the geometry of the solid in the mold. For the sake of argument, let us consider a cube with sides d. In applications, it is important to determine its shape after release from the mold. If d is very small, the deformation is expected to be predominantly driven by the surface tension, since the average strain of the cube due to surface tension is on the order of

$$\alpha \equiv \frac{\gamma}{\mu d} \tag{1.4}$$

On the other hand, if the cube is sufficiently large, then gravity will dominate, in which case the average strain will be on the order of

$$\beta \equiv \frac{\rho g d}{\mu} \tag{1.5}$$

where g is the acceleration of gravity.

The dominant force(s) that drive(s) the deformation can be determined by comparing the magnitude of the two dimensionless strain parameters α and β to each other and to unity. The influence of gravity and surface tension is about the same when the cube has sides of the characteristic length scale d_c determined by the condition

$$\frac{\rho g d_c}{\mu} = \frac{\gamma}{\mu d_c} \tag{1.6}$$

Equation (1.6) can expressed in terms of the Bond or Eötvös number $b_o \equiv \rho g d^2 / \gamma$,

$$b_o\left(d_c\right) = \frac{\rho g d_c^2}{\gamma} = 1 \tag{1.7}$$

That is, gravity dominates deformation for large Bond number and surface tension drives deformation for small Bond number.

Equation (1.7) shows that d_c is independent of modulus. For materials such as hydrogels with surface energy and density similar to those of water, the characteristic length scale d_c is on the order of 3 mm. In this regime, a rough estimate of the magnitude of average strain in a meta-gel cube, using μ = 6 Pa, shows that $\gamma/\mu d_c$ = 4, which corresponds to an average strain of 400%. On the other hand, if the same cube was made of PDMS, the average strain will be smaller by a factor of 10^6 since the shear modulus of PDMS is about 1 MPa and its surface tension is about 20 mJ/m^2.

The fact that deformation depends on two dimensionless 'average strain' parameters α and β suggests the use of a 2D deformation map (Fig. 1.2) in the space spanned by these variables, which shows how shape changes depend on them. Specifically, we introduce a strain space with coordinates (α, β). Each point in this space corresponds to a shape of a given (initially stress-free) elastic body deformed by a combination of gravity and surface tension. The origin (0, 0) corresponds to the initial shape. It is convenient in this strain space to use a polar system of coordinates (R, θ) related to the strain parameters by

$$\alpha = \gamma / \mu d = R \sin\theta$$

$$\beta = \rho g d / \mu = R \cos\theta$$

$$\text{where} \begin{cases} \tan\theta = \dfrac{\gamma}{\rho g d^2} = \dfrac{1}{b_o} \\ R = \sqrt{\alpha^2 + \beta^2} = \dfrac{1}{\mu}\sqrt{(\gamma/d)^2 + (\rho g d)^2} \end{cases} \tag{1.8}$$

Circular arcs in the deformation map correspond to changing Bond Number b_o with constant elastic modulus, whereas the elastic modulus decreases with increasing distance along a radial line. Thus, R is a measure of strains due to surface tension and gravity; a point at a distance far away from the origin corresponds to very large shape change.

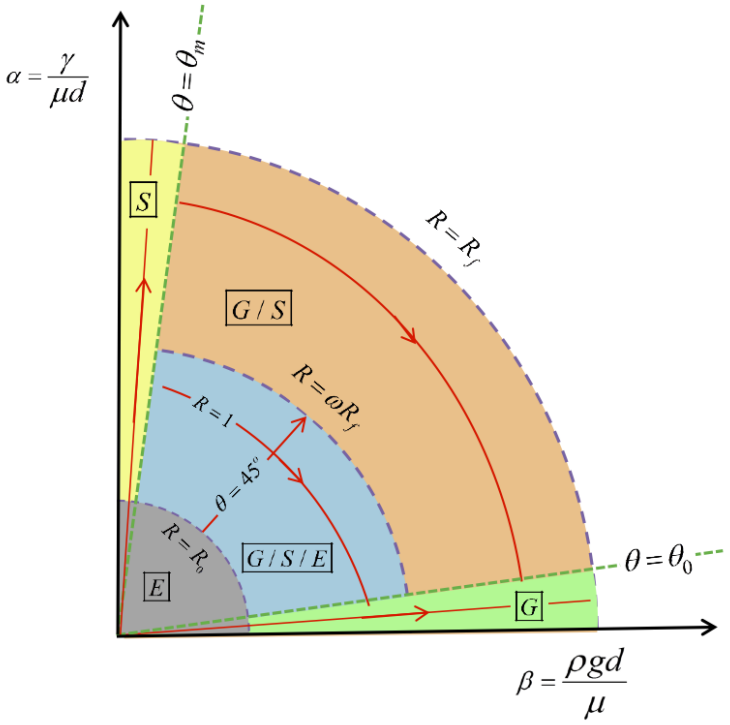

Figure 1.2 The Deformation Map. We describe five regions according to the relative importance of the roles of elasticity, surface tension and gravity in defining the shape of a soft material: 1. Small Strain Regime (E); 2. Gravity Dominant Regime (G); 3, Surface Tension Dominant Regime (S); 4. Gravity and Surface Tension Dual Action Regime (G/S); 5. Gravity, Surface Tension and

Elasticity Triple Action Regime (G/S/E). Analysis has been carried out for each regime along the red paths.

Dashed and dotted lines in Fig. 1.2 divide the deformation map into five regimes. The grey regime (E) occupies the interior of a small quartered circle of radius $R_0 << 1$ centered at the origin, where R_0 is some value small enough compared to unity for strain to be regarded as negligible. In this region, the deformation due to gravity and surface tension is negligibly small. This is the typical situation for structures made of stiff materials such as ceramics, metals and inorganic glasses for any value of d greater than a few atomic spacing. The other extreme of $R \to \infty$ is clearly impossible, since no solid can support infinite deformation, so there must exist a circle of radius R_f, outside which the solid fails. We need only to consider points inside this circle. If we pick some suitably small value of $\theta_0 << 1$, the circular sector bounded by $0 \leq \theta \leq \theta_0$ and $R < R_f$ represents the green regime (G), where gravity is the dominant force that drives deformation. Similarly, the yellow regime (S) is the circular sector bounded by $\theta_m \leq \theta \leq \pi/2$ and $R < R_f$, where a value of θ_m suitably close to $\pi/2$ is chosen such that surface tension dominates. The region in between regimes E, G and S can further be separated into two regimes. One of them, the blue regime (G/S/E), is bounded by $0 < \theta < \pi/2$ and $R \leq \omega R_f$, where $\omega < 1$ is a positive number that characterizes the maximum deformation allowed by which this regime is defined. Inside this region the deformed shape is driven by both gravity and surface tension and shape change is resisted by the restoring forces of elasticity. Finally, in the orange regime (G/S), $0 < \theta < \pi/2$ and $R > \omega R_f$, the modulus is sufficiently small that the material behaves almost like a liquid. As a result, the final deformed shape bears little resemblance to the original shape. For example, a cube and a long cylindrical bar of the same volume can be deformed into a sphere of the *same* radius. It is clear that these regimes do not have clear-cut boundaries, for example, we can set $\omega = 3/4$.

Such a deformation map would apply to freely-suspended and roughly equiaxial stress-free shapes (cubes, spheres etc.). Specifically, the deformation map does not account for the effect of boundary conditions imposed on the deformation of the elastic body. The analogous situation for liquid capillarity is the difference between shapes of a pendant drop and a drop of the same liquid in contact with a solid surface. As expected, here too, shape change will be affected by the contact condition, which is determined by friction, adhesion and the affinity (or lack thereof) of the surfaces in contact. This will be discussed in more detail below.

1.3 Example of a Deformation Map

As a concrete example, in the following we will determine the shape change of an initially stress-free circular cylinder with equal height and diameter *d* as shown schematically in Fig. 1.3, where *Z* and *r* denote the vertical and radial positions of a material point in the referential undeformed configuration respectively. After the cylinder is released from the mold in which it was cast, it is placed on a flat frictionless rigid surface and is deformed by gravity and surface tension.

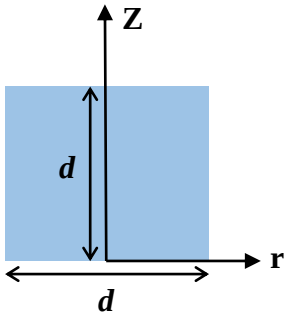

Figure 1.3 Referential Undeformed Configuration. We use a short circular cylinder with equal height and diameter in all the simulations.

Determining the shape change of three dimensional elastic bodies with arbitrary initial shape due to surface tension and gravity is a non-trivial problem. In this work we consider only axisymmetric deformation. Consistent with this assumption, surfaces in this study are assumed to be homogeneous and isotropic, so that surface stress is an isotropic tensor with magnitude equal to the surface tension. We avoid elastic instabilities such as buckling by restricting our attention to a short cylinder (see the discussion section). However, the governing equations of elasticity are still nonlinear due to the nonlinear kinematics caused by large deformation as well as nonlinear material behavior. Additional nonlinearity is also introduced by the shape changes and the contact condition. Specifically, the location of the contact line, which in our case is a circle, is unknown and dependent on boundary or contact conditions. As in most contact mechanics approaches, we assume frictionless contact. For hydrogels, it is also reasonable to assume the interfacial tension of gel (g) / air (v) interface, γ_{gv} to be the surface tension of water. Since a solid (e.g. gel) can resist shear, the contact angle ϕ between the solid and the substrate is determined numerically by solving the full set of elasticity equations and in general *does not* satisfy Young's equation [15]:

$$\cos\phi = \frac{\gamma_{sv} - \gamma_{sg}}{\gamma_{gv}} \tag{1.9}$$

where γ_{sv} and γ_{sg} are the interfacial energies between the substrate (s) / air (v) and substrate (s) / gel (g) respectively. There is but one exception for the examples in this work: $\phi = \pi/2$ if $\gamma_{sv} = \gamma_{sg}$; this is because the substrate is rigid and the undeformed cylinder's lateral surface is perpendicular to the substrate. In general, even though the contact angle may not be given by equation (1.9), it is expected that the contact angle will be more than $\pi/2$ if $\gamma_{sv} - \gamma_{sg} < 0$ and less than $\pi/2$ if $\gamma_{sv} - \gamma_{sg} > 0$. In this chapter, we neglect adhesion – the position of the contact line is determined by the (Hertz)

condition- it lies where the normal interfacial traction between the cylinder and the substrate turns purely compressive. The role of adhesion will be discussed in the last section of this chapter.

Although there is no difficulty using more sophisticated models to quantify material behavior, we use the neo-Hookean model so as to capture large deformation while retaining the simplicity of a single parameter (μ) to represent elasticity. A finite element method (FEM) is used to solve for the deformation and stresses caused by gravity and surface tension. The commercial software, ABAQUS® is used in all our numerical simulations. Loading due to surface tension is simulated via a user-defined surface element [1 16]. Details of our finite element method are given in Appendix 1.2. In the following we will present the numerical results. Approximated analytical solutions are possible in regimes 2, 3 and 4, and we will compare these solutions to our FEM results.

1.4 Results

Regime E: Small Strain Regime α << 1 and β << 1. In this regime, the stress-strain relation of an isotropic hyperelastic material in the infinitesimal strain limit reduces to isotropic linear elasticity. Surface tension and gravity effects can be neglected.

Regime G: Gravity Dominant Regime α << β and α <<1. Gravity dominantly drives the deformations of solids in this regime, whereas surface tension only acts locally to round off sharp edges. Hence the deformation in this regime is controlled solely by the strain parameter $\beta \equiv \rho g d/\mu$.

We carried out our analysis along the red line in regime G of the deformation map shown in Fig. 1.2. An approximate analytical large strain solution can be obtained by assuming all the components of the 1st Piola-Kirchhoff stress vanish except the one that is parallel to the direction of gravity (i.e. *Z* direction in the referential configuration shown in Fig. 1.3). A straightforward analysis shows that the stretch ratio in vertical direction $\lambda_z \equiv \lambda$ is related to *Z* in the reference configuration by

$$\lambda - \frac{1}{\lambda^2} = \beta(z-1), \text{ where } \beta = \frac{\rho g d}{\mu},\ z = \frac{Z}{d} \tag{1.10}$$

Equation (1.10) has only one positive real root of λ, whose value depends on the discriminant $\Delta = 4\beta^3(1-z)^3 - 27$:

$$\begin{aligned}
&\Delta = 0,\ \lambda = 2^{-2/3} \\
&\Delta < 0,\ \lambda = -\frac{1}{3}\left\{\beta - \beta z + \sqrt[3]{\frac{1}{2}\left(2\beta^3(1-z)^3 - 27 + \sqrt{-27\Delta}\right)} + \sqrt[3]{\frac{1}{2}\left(2\beta^3(1-z)^3 - 27 - \sqrt{-27\Delta}\right)}\right\} \\
&\Delta > 0,\ \lambda = \frac{2\beta(1-z)}{3}\cos\left(\frac{n+m\pi}{3}\right) - \frac{\beta(1-z)}{3},\ \text{where } m = 0, 2, 4,\ n = \cos^{-1}\left(\frac{27 - 2\beta^3(1-z)^3}{2\beta^3(1-z)^3}\right)
\end{aligned} \tag{1.11}$$

The vertical displacement δ of the top free surface normalized by the initial height of cylinder *d*, can be obtained using

$$\delta / d = 1 - \int_0^1 \lambda(\beta, z)\, dz \tag{1.12}$$

Another quantity of interest is the minimum stretch ratio λ_{min} ($\lambda_{min} < 1$ indicates that material element is compressed), which occurs at the bottom surface, i.e. $z = 0$. Since the approximated analytical solution assumes the deformation of a point being independent of its lateral position, we compare the results from equation (1.11) and (1.12) with numerical results by taking the average of top surface (bottom surface) vertical displacements (stretch ratios) from the FEM simulation.

Fig. 1.4a plots the (average) vertical displacement at the top surface against the strain parameter β. Fig. 1.4b shows the variation in λ_{min} with β. The analytical solution is found to be in good agreement with FEM result. The deformed shape is compared to the initial shape in Fig. 1.4c and 1.4d for $\beta = 80$ and $\beta = 20$. Due to symmetry, only half of the cylinder is shown with contours representing surfaces of constant vertical displacement U_2.

The DNA hydrogel sample in Fig. 1.1 lies approximately in this regime. A rough estimate of the magnitude of average strains in the gel sample, using $\mu = 5$ kPa, gives $\alpha \sim 2$ and $\beta \sim 15$. Fig. 1.1 shows that gravity force compressed the sample to less than half of its initial height. It agrees qualitatively with our numerical results.

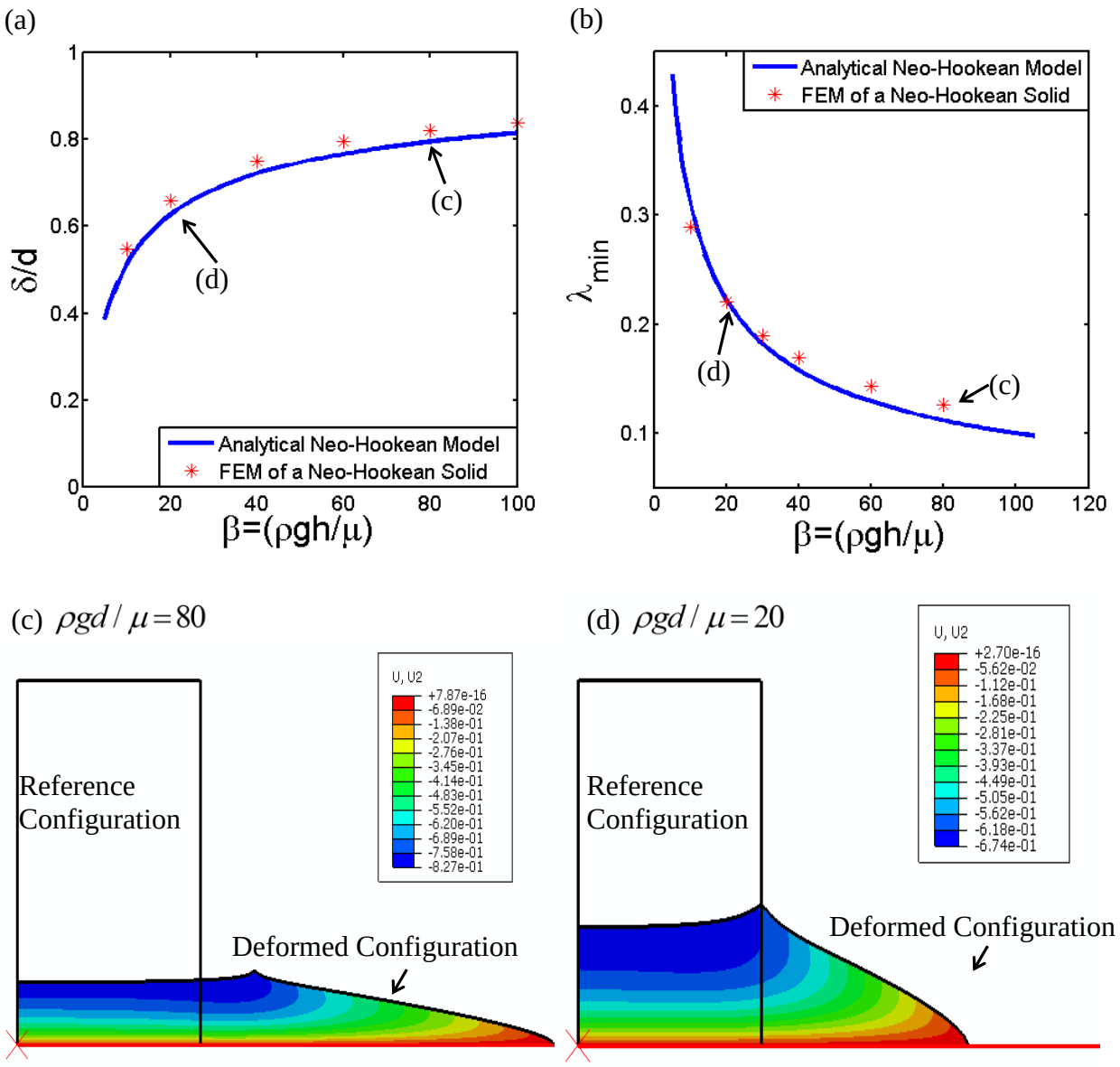

Figure 1.4 Results for Gravity Dominant Regime Using a Neo-Hookean Model. (a), (average) vertical displacement at the top surface δ/d against β; (b), minimum stretch ratio λ_{min} (average vertical stretch ratio at the bottom surface) against β; (c), initial and deformed shapes at β = 80; (d), initial and deformed shapes at β = 20. Contours represent surfaces of constant vertical displacement U_2.

Regime S: Surface Tension Dominant Regime α >> β and β <<1. The average strain due to gravity is small for solids in this regime so we can characterize the deformation based solely on the strain parameter $\alpha \equiv \gamma/\mu d$. The effect of surface tension becomes increasingly prominent as one moves along the red line in the direction of increasing α on the deformation map (regime S) in Fig. 1.2. When $\alpha >> 1$ (i.e. structures of very small size or materials with negligible modulus) is reached, surface tension deforms solids into spherical caps, regardless of their initial shape.

In the following, we characterize the deformed shapes using the deformed height h and the contact base radius r_c as defined in Fig. 1.5a, and all length scales are normalized by the initial height d of the cylinder. First, we consider the special case where the contact angle $\phi = \pi/2$. Results from FEM simulations for increasing values of α are plotted in Fig. 1.5b for this case. As expected, the deformed height h and the contact base radius r_c converge to the same value as α increases, implying that the deformed shape is a hemisphere. Fig. 1.5c and 1.5d compare the deformed shapes with the initial shape for $\alpha = 1$ and $\alpha = 100$ respectively with prescribed contact angle $\phi = \pi/2$. For $\alpha = 1$ (Fig. 1.5c), surface tension effect is confined to the corner (i.e. the top edge of the cylinder), while the rest of the original shape is mostly unchanged due to resistance by elasticity. In contrast, for $\alpha = 100$ (Fig. 1.5d), surface tension dominates elasticity and the deformed shape is approximately a hemisphere.

To further validate our FEM results, we note that an analytical solution can be obtained for the special case of $\alpha >> 1$. In this regime, the final deformed shape is a spherical cap and is approximately independent of the initial shape. Since the material is incompressible, the dimensions of the spherical cap are completely determined by the initial volume of the solid V_0

and the equilibrium contact angle ϕ. Specifically, the height of the cap h and the radius of its base r_c is obtained by solving equations (1.13) and (1.14),

$$\cos\phi = \frac{r_c^{\,2} - h^2}{r_c^{\,2} + h^2} \tag{1.13}$$

$$V_0 = \frac{\pi}{6} h(3r_c^{\,2} + h^2) \tag{1.14}$$

Fig. 1.5b, shows that the spherical cap solution given by (1.13) and (1.14) is a good approximation when α is greater than 10. Hence in Fig. 1.5e, we compare the FEM results for α = 100 to the analytical results for the full range of contact angles. In this figure, the volume of the cylinder $V_0 = \pi d^3/4$ is fixed. The results show good agreement between the approximated theory and FEM simulations.

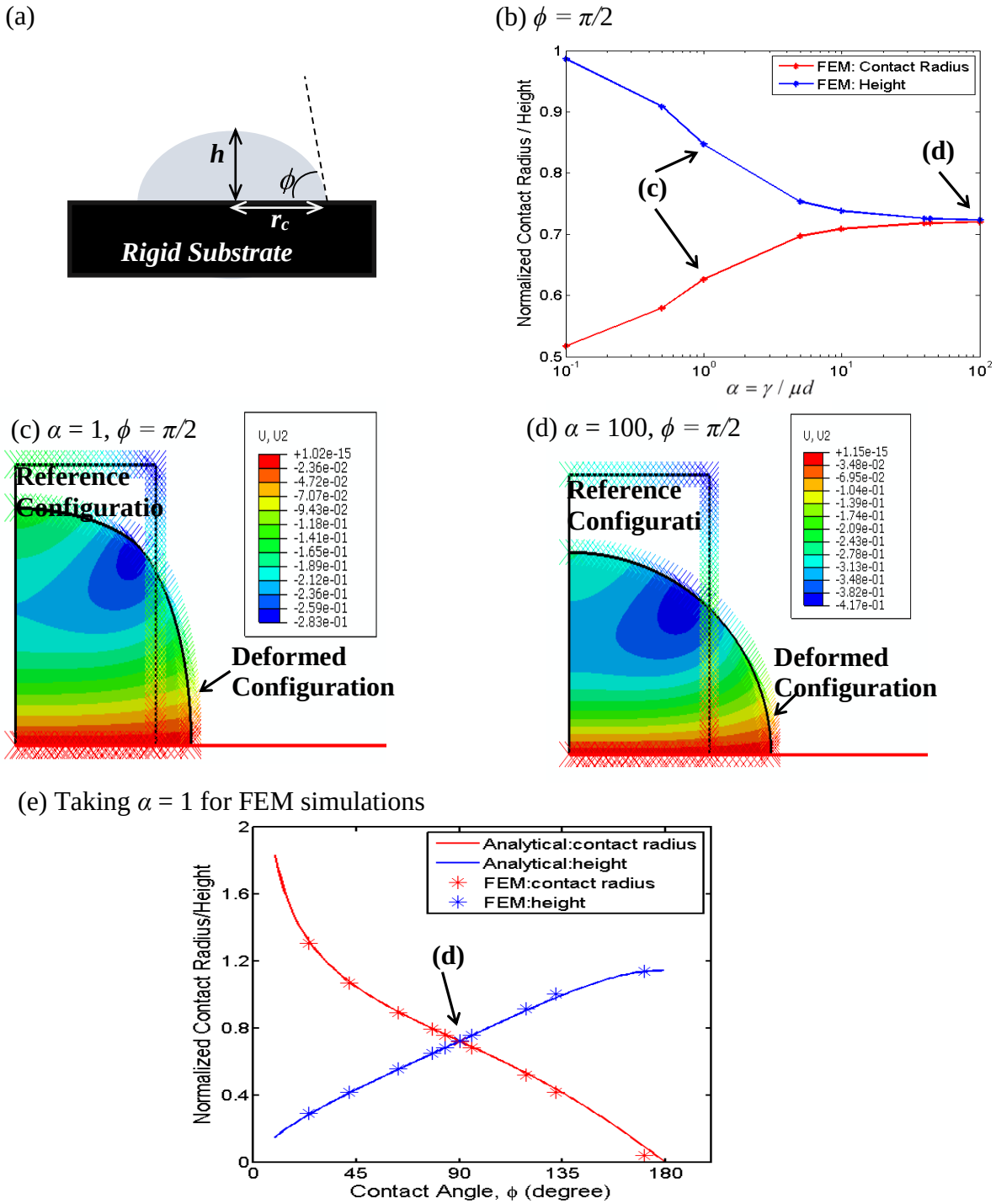

Figure 1.5 Results for Surface Tension Dominant Regime. (a), deformed configuration; (b), plots of normalized contact radius r_c and deformed height h against strain parameter α for contact angle $\phi = \pi/2$; (c), comparison of deformed shape with initial shape for $\alpha = 1$, $\phi = \pi/2$; (d), comparison of deformed shape with initial shape for $\alpha = 100$, $\phi = \pi/2$; (e), plots of r_c and h against contact angle ϕ when $\alpha >> 1$, FEM results are obtained at $\alpha = 100$.

Regime G/S: Gravity and Surface Tension Dual Action Regime α >> 1 and β >> 1. Solids in this regime deforms like a liquid with no apparent resistance to shape change because gravity, surface tension or both overwhelm the elastic restoring forces. In this regime, the deformed shape is dependent only on the initial volume V_0 (which remains constant due to incompressibility), boundary conditions (we assume frictionless contact and prescribe the contact angle ϕ) and the Bond number b_o; it is approximately independent of the initial shape. Hence the deformed shape is governed by the standard theory of liquid capillarity but, as demonstrated in Fig. 1.1, the solid can still retain its ability to recover its original shape if gravity and surface tension are removed. For an axisymmetric liquid drop in a gravity field [17], the final deformed shape can be determined by solving a boundary value problem involving three ordinary differential equations. Since the theory is well known, we include the relevant details in Appendix 1.3; here we present the results of these calculations.

The deformed coordinates in these calculations are defined in Fig. 1.6a. It is convenient to normalize all length scales by r_0, the radius of a sphere with the same volume V_0 as the undeformed solid. We start by prescribing the contact angle to be $\pi/2$ and vary the Bond number so that these deformations lie on the circular arc in regime 4 of the deformation map in Fig. 1.2. When Bond number is small (b_o = 0.1), surface tension outweighs gravity, the deformed shape can be approximated by a hemisphere, i.e. $r_c \approx h$ as shown in Fig. 1.6b. As the gravity becomes more significant with increasing b_o, the contact radius and deformed height diverge from each other, indicating that the solid is crushed into the shape of a pancake (similar to the situation in Fig. 1.1).

For a given contact angle, the contact radius and deformed height as well as the deformed shape can be completely determined for a given Bond number as illustrated in Fig. 1.6c. Results for different Bond numbers, 0.1, 1 and 10 are shown in three plots. Each plot shows the deformed shapes of contact angle ϕ prescribed to be 0.1 π, 0.5 π and π.

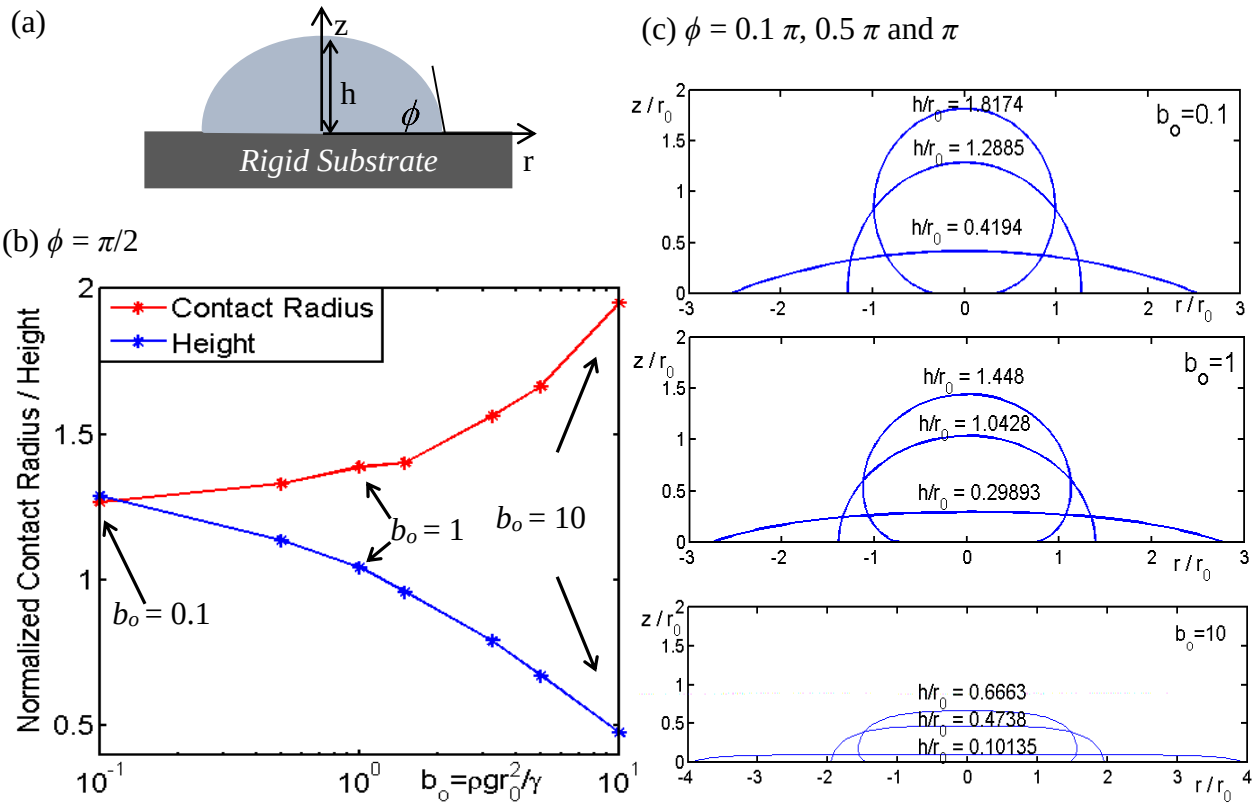

Figure 1.6 Results for Gravity and Surface Tension Dual Action Regime. All lengths are normalized by r_0: (a), deformed configuration; (b), plots of contact radius r_c and deformed height h against Bond number with contact angle of $\pi/2$; (c), deformed shapes plotted for contact angle of $\pi/10$, $\pi/2$ and π, at given Bond numbers of 0.1, 1 and 10.

Regime G/S/E: Gravity, Surface Tension and Elasticity Triple Action Regime. Finally in the last regime, where elastic modulus of the solid is no longer negligible and the gravity and surface tension effects are comparable to each other, we carry out two series of finite element simulations:

one is along the radial line labeled $\theta = 45^o$ (or $b_o = 1$, where surface tension and gravity effects are comparable) and the other is along the arc labeled $R = 1$ in the deformation map (where the average strain is 100%). All simulations are based on a contact angle of $\phi = \pi/2$ and we normalize all lengths by the initial height of the cylinder d.

For the first series of simulations along $\theta = 45^o$, the radial distance R on the deformation map increases with decreasing shear modulus μ while the Bond number is fixed at 1. The contact radius r_c and deformed height h are plotted against the average strain R in Fig. 1.7a. As expected, the deformed height decreases and the contact radius increases with increasing average strain R. Deformed shapes for the cases of $R = 0.1$, 1 and 10 (indicated by arrows in Fig. 1.7a) are compared to the initial shape in Fig. 1.7c.

Fig. 1.7b plots results from the second series of simulations where the average strain R is fixed to be 1 while the Bond number changes. An increase in Bond number (i.e. a decrease in θ on the deformation map) indicates increasing importance of gravity compared to that of surface tension. Fig. 1.7b shows that the contact radius and deformed height are quite insensitive to the Bond number for a given average deformation R. Selected deformed shapes of the cases tan $\theta = 0.1$, 1 and 10 are also compared to the reference configuration in Fig. 1.7d corresponding to points labeled in Fig. 1.7b. Colors in these figures denote contours of constant vertical displacement *U2*.

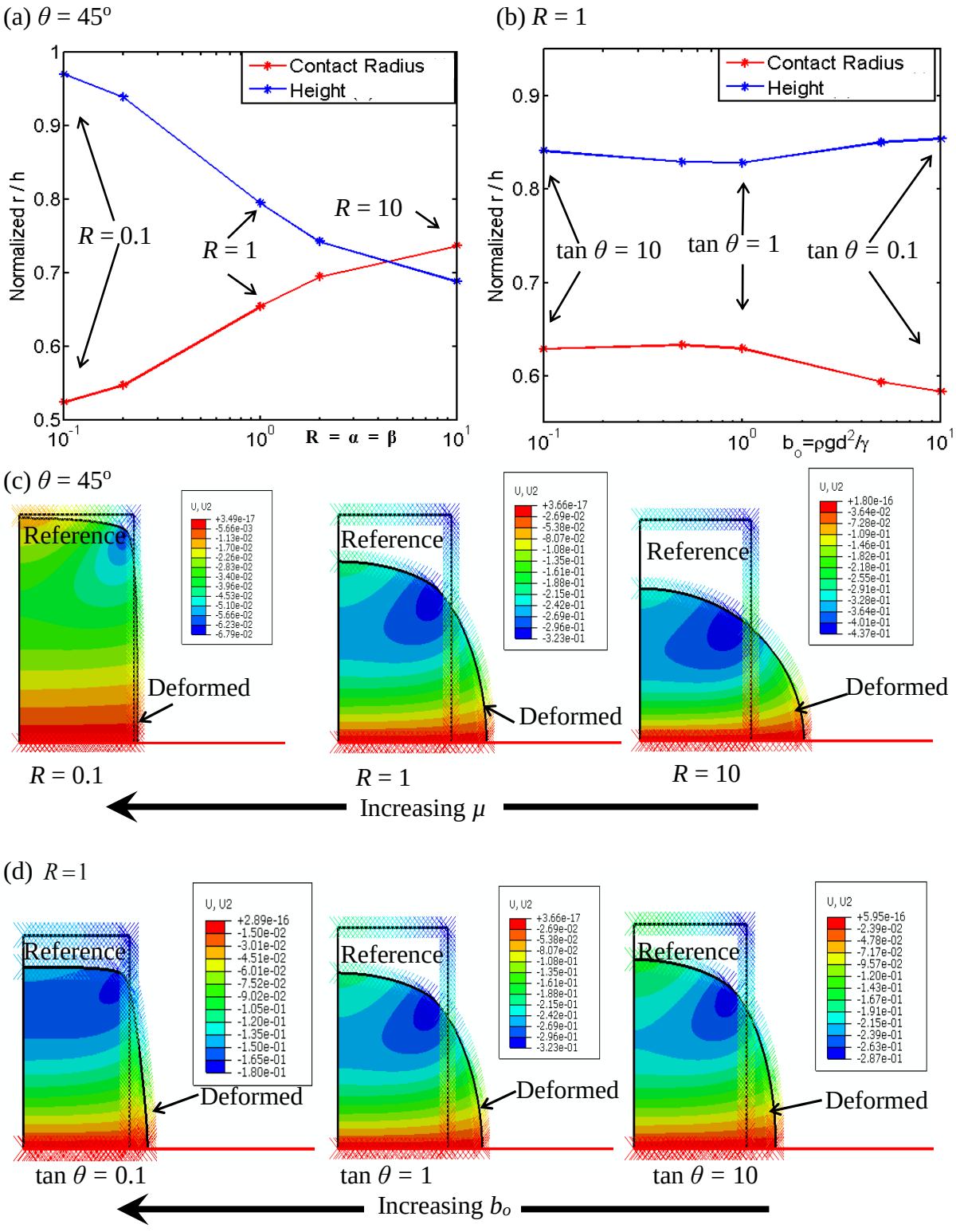

Figure 1.7 Results for Gravity, Surface Tension and Elasticity Triple Action Regime. All lengths are normalized by initial height of the cylinder d: (a), plots of contact radius r_c and

deformed height h along the radial line on the deformation map of $\theta = 45^o$; (b), plots of r_c and h along the arc of $R = 1$ on the deformation map; (c), deformed shapes corresponding to points labeled in (a) are compared with the initial shape; (d), deformed shapes corresponding to points labeled in (b) are compared with the initial shape. Colors denote contours of constant vertical displacement *U2*.

1.5 Conclusion and Discussion

A deformation map is proposed to characterize the shape change of soft materials subjected to gravity and surface tension forces. The deformation map can be partitioned into five regimes, and the characteristic of each regime is described in some detail using a specific example of a short circular elastic cylinder placed on a flat smooth rigid substrate. A circular cylinder is chosen in this work but there is no difficulty simulating other geometries. It has long been known that a long elastic column will buckle under its own weight when its length exceeds $L_{max} = (7.84\ w/D)^{1/3}$, where w is weight per unit length and D is the flexural rigidity of the column [18]. Hence we study the deformation of a short cylinder to avoid non-unique solutions caused by buckling. Experimental data of the cylindrical DNA hydrogel sample in Fig. 1.1 is also compared qualitatively to our numerical results in the gravity dominant regime.

In our analysis, we assume the soft material is incompressible, isotropic and neo-Hookean. This is the simplest material model that captures many important features of elastic materials composed of polymer networks. It is well known that the neo-Hookean model underestimates the amount of strain hardening, especially in the large deformation regime when chains between cross-links are fully extended. Hence our solution tends to overestimate the amount of deformation. The calculations and simulations in this work can be readily extended to other strain-energy functions

that model these strain-hardening effects, as well as anisotropy and compressibility. Since these models are material-specific, we leave these applications to future works.

Accurate representation of contact requires quantitative description of surface interactions. Modeling realistic surface interaction is still an unresolved problem. There is no universal accepted model which accounts for both friction and adhesion, not to mention hydrophobic and hydrophilic interactions. In all our simulations, frictionless boundary condition is enforced – this is an assumption that is consistent with most contact mechanics approach. Undoubtedly, there are situations where the frictionless boundary condition is inappropriate. However, there is no difficulty enforcing the opposite limit where no slip is allowed in our simulations.

A final word regarding the use of frictionless boundary condition: on a frictionless interface the contact line is free to move laterally, so that the quantities γ_{sv} and γ_{sg} in Young's equation (1.9) should be interpreted as interfacial energies and not as interfacial tensions. However, if no slip is allowed, these quantities should be regarded as interfacial tensions. This distinction is important since the surface energy of a solid can be different from its surface tension.

We emphasize that there are two distinct approaches to the contact mechanics of liquid drops and elastic bodies. In the literature, the equilibrium shape of a liquid drop on a frictionless rigid substrate is determined by Young's equation and the Laplace capillary equation. On the other hand, the shape of an elastic solid in contact with a rigid substrate is determined by solving the full elasticity equations subjected to displacement and traction continuity in the contact region *without* regard to interfacial energies and surface tension. The location of the contact line is determined by enforcing the Hertz condition for non-adhesive contact (that is, only compression is allowed inside

the contact region and it is traction free outside). Adhesion can be accounted for using cohesive zone models which specifies how interfacial traction varies with the interfacial displacements [19]. These two approaches are distinct and cannot be reconciled without additional physics since they are based on different sets of equations. Our formulation unifies these two approaches since the surface of our elastic solid is endowed with surface tension elements so that our results will approach the capillary limit when the shear modulus of our elastic solid approaches zero. In our simulations, we assume non-adhesive contact to reduce the number of material parameters. Adhesion is clearly important when structural dimensions or moduli are small, that is, in the surface tension dominated regime. The effect of adhesion can be modelled by incorporating surface interaction potentials and will be addressed in future works.

Acknowledgement

C.Y. Hui, A. Jagota and X. Xu acknowledge support from the U.S. Department of Energy, Office of Basic Energy Science, Division of Material Sciences and Engineering under Award (DE-FG02-07ER46463).

Appendix 1.1 Analytical Calculations in Gravity Regime

Consider a circular disk of radius *a*, and height *d*, as shown in Fig. A.1.1.1. For isotropic and incompressible material,

$$\mathbf{P} = -p\mathbf{F}^{-T} + \frac{\partial \Psi}{\partial \mathbf{F}} \qquad \text{(A.1.1.1)}$$

where p is the hydrostatic pressure that enforces the incompressibility. Assuming all the components of 1st Piola Kirchhoff stresses P_{ij} are zero except the normal component P_{33}, where by equilibrium,

$$\begin{aligned} &P_{11} = 0, P_{22} = 0 \\ &P_{33} = P = \rho g\left(Z - d\right) \end{aligned} \qquad \text{(A.1.1.2)}$$

This assumption is most valid when $a>>d$. In the case of axisymmetric model, the principal stretches are normal stretch ratio $\lambda_3 = \lambda$, and lateral stretch ratios $\lambda_1 = \lambda_2 = 1/\sqrt{\lambda}$, due to incompressibility. Thus,

$$\begin{aligned} &\frac{-p}{\lambda_1} + \frac{\partial \Psi}{\partial \lambda_1} = 0 \Rightarrow p = \lambda_1 \frac{\partial \Psi}{\partial \lambda_1} \\ &\rho g\left(Z - d\right) = -\frac{\lambda_1}{\lambda}\frac{\partial \Psi}{\partial \lambda_1} + \frac{\partial \Psi}{\partial \lambda} = \frac{-1}{\lambda^{3/2}}\frac{\partial \Psi}{\partial \lambda_1} + \frac{\partial \Psi}{\partial \lambda} \end{aligned} \quad . \qquad \text{(A.1.1.3)}$$

Substituting the strain energy function of a neo-Hookean material into equation (A.1.1.3), a relationship between the normal stretch ratio λ and vertical position Z is obtained,

$$\Psi = \frac{\mu}{2}(I_1 - 3) = \frac{\mu}{2}(\lambda_1^2 + \lambda_2^2 + \lambda_3^2 - 3) \qquad \text{(A.1.1.4)}$$

$$\beta\left(z - 1\right) = \frac{-1}{\lambda^2} + \lambda \text{ where } \beta = \frac{\rho g d}{\mu}, z = \frac{Z}{d} \qquad \text{(A.1.1.5)}$$

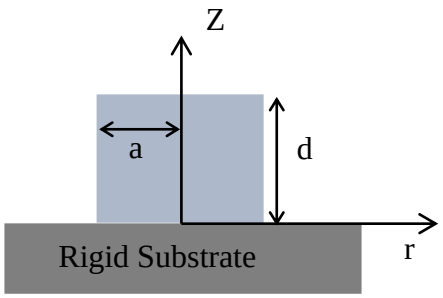

Figure A.1.1.1. Referential undeformed configuration of a soft solid placed on a rigid substrate.

We are interested in finding λ (β, z). The right hand side of equation (A.1.1.5) is monotonically increasing in (0, ∞). Hence there is only one real root to the equation, which is presented in the chapter. Fig. A.1.1.2 shows the variation of stretch ratio with normalized vertical coordinate z in the case of β = 80. The finite element (FE) results are shown as stars, using $2a = d$. One thing to note is that it is easier to plot z with given value of λ in the domain of $z \in [0,1]$.

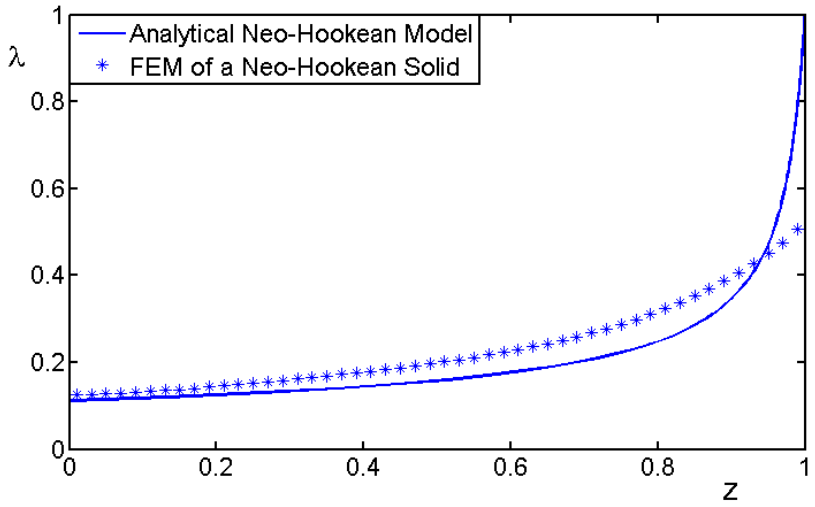

Figure A.1.1.2. Plot of normal stretch ratio λ against normalized vertical coordinate z.

Another interested parameter is the vertical displacement δ of the top surface, which is normalized by the initial height d,

$$\delta / d = 1 - \int_0^1 \lambda(\beta, z) dz \tag{A.1.1.6}$$

From equation (A.1.1.5), at given constant value of β

$$dz = \frac{1}{\beta}\left(1 + \frac{2}{\lambda^3}\right) d\lambda \tag{A.1.1.7}$$

$$\frac{\delta}{d} = 1 - \int_{\lambda_{\min}}^1 \lambda \frac{1}{\beta}\left(1 + \frac{2}{\lambda^3}\right) d\lambda = \frac{1}{\beta}\left(\frac{2}{\lambda_{\min}} - \frac{\lambda_{\min}^2}{2} - \frac{3}{2}\right) \tag{A.1.1.8}$$

where λ_{min} is the minimum stretch ratio occurred at the bottom surface of $z = 0$.

Appendix 1.2 Finite Element Simulation of Surface Tension Effect

In ABAQUS®/Standard, loads are applied in small increments, the incremental displacements are found by iterations. Specifically, ABAQUS®/Standard used the Newton-Raphson (N-R) method: for any iteration n, the equation to be solved is

$$\mathbf{R}^n\left(\mathbf{u}^n + \mathbf{c}^{n+1}\right) = 0 \tag{A.1.2.1}$$

where $\mathbf{R}^n$ is the residual force as a function of $\mathbf{u}^n$, the displacement approximation from the previous iteration (or the initial guess of displacement if $n = 1$), and $\mathbf{c}^{n+1}$, the difference between $\mathbf{u}^n$ and the exact displacement solution. Linearization of equation (A.1.2.1) using Taylor expansion and neglecting higher order terms for small magnitude of $\mathbf{c}^{n+1}$ gives

$$\mathbf{R}\left(\mathbf{u}^n\right)+\mathbf{K}^n\mathbf{c}^{n+1}=0 \qquad \text{(A.1.2.2)}$$

where $\mathbf{K}^n\left(\mathbf{u}^n\right)=\frac{\partial \mathbf{R}}{\partial \mathbf{u}}\left(\mathbf{u}^n\right)$ is the Jacobian matrix to be assembled and solved in the nth iteration. Then for the (n+1)th iteration, the approximated displacement is $\mathbf{u}^{n+1}=\mathbf{u}^n+\mathbf{c}^{n+1}$. Incompressibility is handled by using a hybrid u-p element formulation.

In our model, 4-node bilinear axisymmetric quadrilateral hybrid element CAX4H is used for the circular cylindrical reference configuration. A simple convergence test (Fig. A.1.2.1a) is carried out in the case without applying surface tension effect to select the desirable mesh-size. Fig. A.1.2.1b shows the mesh we used in all simulations.

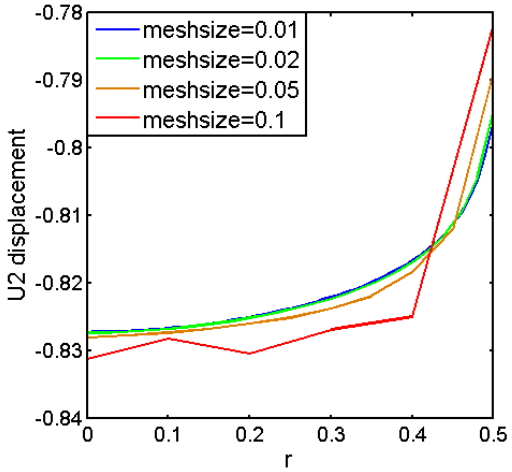

(a) Convergence test: vertical displacement of the top surface.

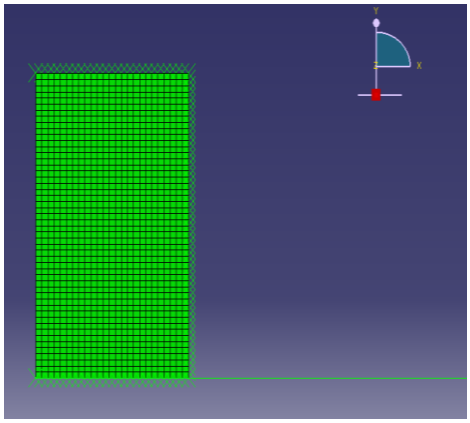

(b) Mesh used for all cases: mesh size=0.02.

Figure A.1.2.1 Mesh selection of the FE model: (a), convergence test by plotting the normal displacements of nodes on the top edge at different mesh sizes; (b), reference configuration drawn with the selected mesh.

The crosses on the external edges in Fig. A.1.2.1b indicate 2-node linear axisymmetric surface elements that are used to simulate surface tension, which is applied incrementally, through a user-

subroutine in ABAQUS®. Fig. A.1.2.2 schematically shows the assignment of surface elements. Two 4-node quadrilateral bulk elements *a* and *b* are on the external edge of the model with nodes 1, 2 and 3 lying on the outer surface, which is discretized naturally to form two 2-node axisymmetric surface elements 1-2 and 2-3.

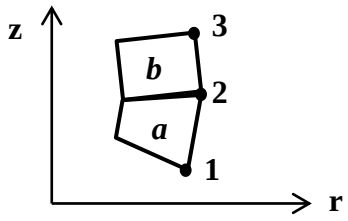

Figure A.1.2.2 A schematic diagram of two 2-node surface elements.

As mentioned above, ABAQUS® solves the overall system of equation (A.1.2.2) iteratively. During iterations we need to define the surface element's contribution to the residual **R** via nodal forces and the element's contribution to the Jacobian matrix **K**. Considering a single surface element 1-2, we attach this element to the bulk element via the shared nodes 1 and 2, hence if physically the bulk element experiences a surface tension γ, the surface element is under a force of same magnitude but opposite direction, i.e. $-\gamma$. Hence the potential energy of this element due to the constant surface tension increment is

$$\Pi^e = -\gamma A^e,\ A^e = \pi\left(r_1 + r_2\right)\sqrt{\left(r_2 - r_1\right)^2 + \left(z_2 - z_1\right)^2} \tag{A.1.2.3}$$

where A^e is the area of the ring represented by this axisymmetric line element. For the calculations presented in this work, we assume that γ is a constant that does not change with deformation.

Consistent with the convention in ABAQUS®, we define nodal force and deformed position vectors of the surface element 1-2 as

$$\mathbf{f} = \{ f_{1r}, f_{1z}, f_{2r}, f_{2z} \}^T ; \ \mathbf{x} = \{ r_1, z_1, r_2, z_2 \}^T \tag{A.1.2.4}$$

Taking the differentiation of potential energy with respect to nodal positions to get work-equivalent nodal forces on the bulk element

$$f_i = -(-\frac{\partial \Pi^e}{\partial x_i}) = \frac{\partial \Pi^e}{\partial x_i}, \text{ where } i = 1, 2, 3, 4 \tag{A.1.2.5}$$

The element's contribution to the Jacobian matrix **K** supplied for iterative solution is hence,

$$K_{ij}^e = \frac{\partial R_i}{\partial u_j} = \frac{\partial f_i}{\partial x_j} \quad i, j = 1, 2, 3, 4 \tag{A.1.2.6}$$

This formulation can be readily extended for other nonlinear finite element codes.

Boundary conditions include the axisymmetry on the left edge (the axis of symmetry) and frictionless contact between the cylinder and rigid surface.

In the regime where surface tension dominates and elasticity is negligibly small, we carried out simulations for different contact angles. In general, Young's equation

$$\cos \phi = \frac{\gamma_{sv} - \gamma_{sg}}{\gamma_{gv}} \tag{A.1.2.7}$$

is not satisfied at the contact line. However when elasticity is neglected, that is when the solid behaves like a liquid, equation (A.1.2.7) needs to be enforced. We treat $\Delta\gamma \equiv \gamma_{sv} - \gamma_{sg}$ as a parameter and vary it in our simulation. $\Delta\gamma$ is implemented differently for hydrophobic (contact angle $\phi > \pi/2$) and hydrophilic cases ($\phi < \pi/2$).

For hydrophobic cases (Fig. A.1.2.3a), $\Delta\gamma < 0$. $\Delta\gamma$ is implemented by assigning smaller surface tension to surface elements in contact with the rigid surface. Since Young's equation only balances the forces in radial direction at the point of gel, solid and air triple contact, in order to ensure that forces are also balanced in the vertical direction, the normal component of nodal force contribution, f_z, applied through the surface element is hence made zero.

For hydrophilic cases (Fig. A.1.2.3b), $\Delta\gamma > 0$. Since the value of surface tension assigned to our surface elements contributes to the overall Jacobian, assigning a negative surface tension to the surface elements in contact with the rigid surface may results in a negative Jacobian. We notice that the point of gel, solid and air triple contact always lies on the same node (i.e. at the bottom right corner), throughout all loading steps. $\Delta\gamma$ is hence implemented by applying a point force on the bottom right corner node in the radial direction, so that the Young's equation is satisfied at that node when elasticity is neglected. Fig. A.1.2.3 below shows the deformations of a soft solid resting on different surfaces with negligible gravity and elasticity.

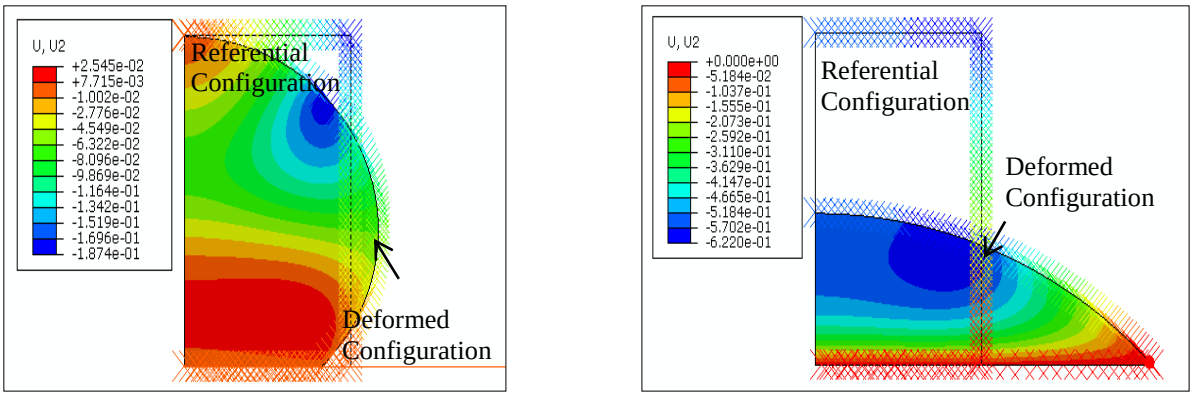

(a) Hydrophobic: $\phi = 3\pi/4$ (b) Hydrophilic: $\phi = \pi/4$

Figure A.1.2.3 Deformation of a soft solid in surface tension dominant regime on (a), a hydrophobic surface; (b), a hydrophilic surface. Colors are contours of vertical displacement *U2*.

Appendix 1.3 Calculations in Gravity and Surface Tension Dual Action Regime

The classical Laplace equation of capillarity relates the pressure gradient across a surface to its curvature,

$$\Delta P = \gamma\left(\frac{1}{R_1}+\frac{1}{R_2}\right) = p_o + \rho g Z \qquad \text{(A.1.3.1)}$$

where R_1 and R_2 are the principal radii of curvature, γ the surface tension, p_o the pressure difference across the interface at the apex O, ρ the density, g the gravitational acceleration and Z the vertical distance of any point on the surface from the apex. Fig. A.1.3.1 shows the current configuration of a soft solid in this regime placing on a rigid substrate, with s is the arc length along the surface of an axisymmetric cut of the body and θ the azimuthal tangent angle of the surface.

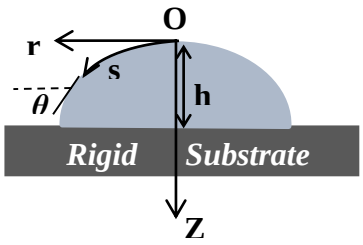

Figure A.1.3.1 Current deformed configuration of a soft solid under gravity and surface tension.

Hence, equation (A.1.3.1) can be rewritten as,

$$\frac{d\theta}{ds}+\frac{\sin\theta}{r}=\frac{p_o+\rho gZ}{\gamma} \tag{A.1.3.2}$$

Also, $\frac{dr}{ds}=\cos\theta, \frac{dZ}{ds}=\sin\theta$ (A.1.3.3)

subject to boundary conditions

$$r\big|_{s=0}=0,\ \theta\big|_{s=0}=0 \text{ and } \theta\big|_{Z=h}=\phi \tag{A.1.3.4}$$

where α is the contact angle that satisfies Young's equation (A.1.2.7).

Since p_0 is also unknown, we need an additional constraint on volume. For incompressible solids, the volume is conserved, i.e.

$$\pi\int_0^h r^2 dZ = V_0 \tag{A.1.3.5}$$

where V_0 is the initial volume. In this work, the initial value problems of equations (A.1.3.2) and (A.1.3.3) are solved numerically using p_0 as a shooting parameter to satisfy equation (A.1.3.4). A

4^{th}-order Runge-Kutta method is implemented. Once r and θ are found, constraint (A.1.3.5) is used to determine the unknown h.

References

[1]. Hui, C. Y.; Jagota, A.; Lin, Y. Y.; Kramer, E. J. Constraints on Microcontact Printing Imposed by Stamp Deformation. *Langmuir* **2002,** No. 18, 1394-1407.

[2]. McDonald, J. C.; Whitesides, G. M. Poly(dimethylsiloxane) as a Material for Fabricating Microfluidic Devices. *Accounts of Chemical Research* **2001,** *35* (7), 491-499.

[3]. Jagota, A.; Hui, C. Y. Adhesion, Friction, and Compliance of Bio-Mimetic and Bio-Inspired Structured Interfaces. *Materials Science and Engineering: Reports* **2011,** *72* (12), 253-292.

[4]. Hoffman, A. S. Hydrogels for Biomedical Applications. *Advanced Drug Delivery Reviews* **2012,** *64, Supplement* (15), 18-23.

[5]. Lee, J. B.; Peng, S.; Yang, D.; Roh, Y. H.; Funabashi, H.; Park, N.; Rice, E. J.; Chen, L.; Long, R.; Wu, M.; Luo, D. A Mechanical Metamaterial Made from a DNA Hydrogel. *Nature Nanotechnology* **2012,** No. 7, 816-820.

[6]. Gibbs, J. On the Equilibrium of Heterogeneous Substances. *Trans. Conn. Acad.* **1876,** *3,* 108-248;343-524.

[7]. Jagota A., P. D. . G. A. Surface-Tension-Induced Flattening of a Nearly Plane Elastic Solid. *Physical Review E* **2012,** *85* (5), 051602.

[8]. Roman, B.; Bico, J. Elasto-capillarity: deforming an elastic structure with a liquid droplet. *Journal of Physics: Condensed Matter* **2010,** *22* (49).

[9]. Yu, Y.-s. Substrate elastic deformation due to vertical component of liquid-vapor interfacial tension. *Applied Mathematics and Mechanics - English Edition* **2012,** *33* (9), 1095-1114.

[10]. Style, R. W.; Che, Y.; Wettlaufer, J. S.; Wilen, L.; Dufresne, E. R. Universal Deformation of Soft Substrates Near a Contact Line and the Direct Measurement of Solid Surface Stresses. *Physical Review Letters* **2013,** *110* (6), 066103.

[11]. Jerison, E. R.; Xu, Y.; Wilen, L. A.; Dufresne, R. The Deformation of an Elastic Substrate by a Three-Phase Contact Line. *Physical Review Letters* **2011,** *106* (18), 186103.

[12]. Mora, S.; Phou, T.; Fromental, J.-M.; Pismen, L. M.; Pomeau, Y. Capillarity Driven Instability of a Soft Solid. *Physical Review Letters* **2010,** *105* (21), 214301.

[13]. deGennes, P. G.; Brochard-Wyart, F.; Quere, D. *Capillarity and Wetting Phenomena Drops, Bubbles, Pearls, Waves;* Springer Science+Business Media, Inc.: New York, 2002.

[14]. Rivlin, R. S. Large Elastic Deformations of Isotropic Materials. IV. Further Developments of the General Theory. *Phil. Trans. R. Soc. Lond. A* **1948,** *241,* 379-397.

[15]. Young, T. An Essay on the Cohesion of Fluids. *Philos. Trans. R. Soc. Lond.* **1805,** *95,* 65-87.

[16]. Jagota, A.; Argento, C.; Mazur, S. Growth of adhesive contacts for Maxwell viscoelastic spheres. *Journal of Applied Physics* **1998,** *83* (1), 250-259.

[17]. Adamson, A. W.; Gast, A. P. *Physical Chemistry of Surfaces;* Wiley: New York, 1997.

[18]. Greenhill, A. G. Determination of the greatest height consistent with stability that a vertical pole or mast can be made, and the greatest height to which a tree of given proportions can grow. *Proc. Cambridge Philos. Soc.* **1881,** No. 4, 65-73.

[19]. Maugis, D. *Contact, Adhesion and Rupture of Elastic Solids;* Springer: New York, 2000.

CHAPTER 2

FLATTENING OF A PATTERNED COMPLIANT SOLID BY SURFACE STRESS*

Abstract

We measured the shape change of periodic ridge surface profiles in gelatin organogels resulting from deformation driven by their solid–vapor surface stress. A gelatin organogel was molded onto poly-dimethylsiloxane (PDMS) masters having ridge heights of 1.7 and 2.7 μm and several periodicities. Gel replicas were found to have a shape deformed significantly compared to their PDMS master. Systematically larger deformations in gels were measured for lower elastic moduli. Measuring the elastic modulus independently, we estimate a surface stress of 107 ± 7 mN m−1 for the organogels in solvent composed of 70 wt% glycerol and 30 wt% water. Shape changes are in agreement with a small strain linear elastic theory. We also measured the deformation of deeper ridges (with height 13 μm), and analysed the resulting large surface strains using finite element analysis.

---

* Paretkar, D., Xu, X., Hui, C.Y. and Jagota, A. (2014). *Soft matter*, 10(23):4084-4090.

2.1 Introduction

Compliant amorphous solids such as elastomers and gels occupy an important place in current materials research. For sufficiently compliant materials, their surface stress can exert a significant influence on material behaviour by driving or resisting deformation. The surface stress of many elastomers and gels is isotropic and can be represented by a single number, σ [1–3]. How the shape of compliant solids is influenced by the surface stress of the solid–fluid interface has been examined in several recent studies [4–9]. Often, surface stress plays a significant role when the characteristic material length scale, σ/E, exceeds some characteristic geometrical feature size, where E is the small strain Young's modulus [1, 10]. For stiff solids such as metals and ceramics this characteristic material length scale is generally smaller than a nanometre and so the resulting deformations are very small and difficult to measure [10, 11]. For compliant solids such as elastomers and gels, however, surface stress driven deformations can be macroscopic (tens to hundreds of μm) and can be readily measured. Mora *et al.* have observed an elastic Rayleigh–Plateau instability in a thin filament of solid hydrogel [6]. Similarly, when a thin elastomeric wire was immersed into a liquid a substantial elastic compression due to the solid capillary pressure was reported [8]. Deformation of thin elastomeric films due to liquid drops placed on their surface has been shown to be influenced strongly by surface stress [12, 13]. We have previously shown that surface stress causes deformation of a ripple surface pattern in a hydrogel [9].

Here we present a study of the surface deformation of a compliant gelatine organo-gel patterned into a periodic ridge-channel shape. The advantage of working with organo-gels is that any drying

effects are substantially minimized [15]. When the gel is released from the geometric constraint imposed by a PDMS mould consisting of periodic ridges (see Fig. 2.1a), the surface stress of the exposed gel–air interface causes the gel to deform. We measure the shapes of the master and the deformed gel, in particular, the reduction in the peak-to-valley distances (*h*) of the gel's surface features upon exposure to air. We systematically change the elastic modulus of the gels to effect a change in the amount of deformation caused by the surface stress. The elastic modulus of the gels is determined independently using beam bending and punch tests (see Appendix 2). The surface stress of the gels is determined by comparing the measured deformation to the prediction of models for surface-stress-driven elastic deformation. Our results suggest that the shape change for nearly flat surfaces in the case of simple geometries such as periodic ridges can be used for determination of the surface stress of compliant solids.

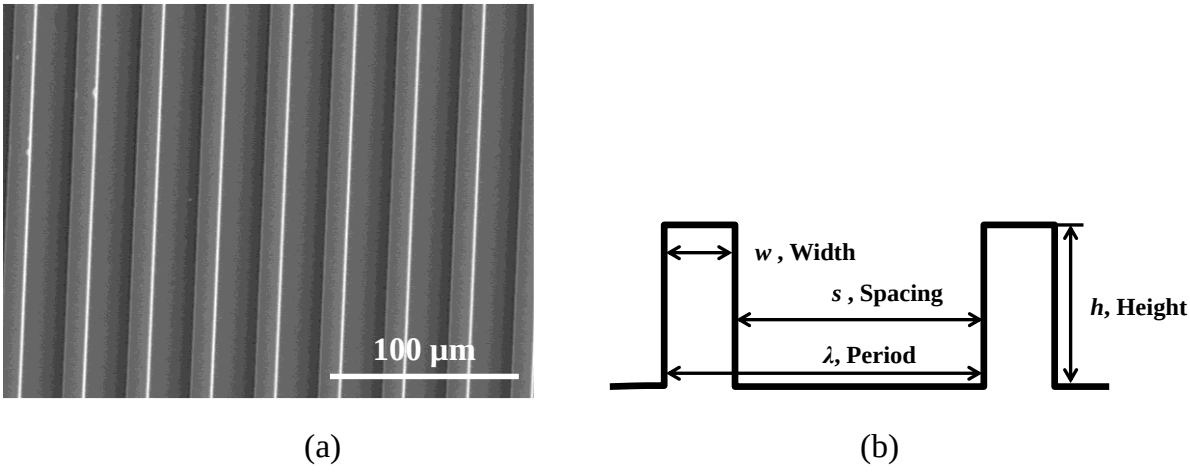

(a) (b)

Figure 2.1 (a) SEM image of a typical PDMS master periodic ridge geometry. (b) Schematic of the periodic ridge geometry.

2.2 Experimental

Fabrication of periodic ridge samples. Polydimethylsiloxane (PDMS) surfaces structured with a periodic ridge geometry were used to replica-mold gelatin gels (Fig. 2.1). Three sets of ridge geometries, one with a height (h) of 13 μm and two others with lower heights of 1.7 and 2.7 μm, were used in this work. For the lower height ridge geometries the width (w) of the ridge was kept the same as the spacing (s) between the ridges, whereas for the high ridge geometry three different periods λ ($\lambda = w + s$) were fabricated. Height, h, is taken as the initial peak-to-valley distance for the gel sample i.e. prior to its demoulding (having previously confirmed that the gel fills the PDMS master without any air cavities [9]).

Table 2.1 lists the details of the periodic ridge geometry. The fabrication details for surface structuring of PDMS with ripple geometries are described in detail elsewhere [14].

Table 2.1 Dimensions (with standard deviations) of periodic ridge geometry. For the case of lower height ridges (h ~1.7 and 2.7 μm) the width was not measured separately but was estimated in the model as half of the mean period.

Ridge/channel h[μm]	Period λ_1 [μm]	Period λ_2 [μm]	Period λ_3 [μm]	Width w [μm]
1.68±0.03	-	39.68±0.52	49.39±0.39	λ/2
2.66±0.05	24.82±0.49	39.77±0.37	49.54±0.29	λ/2
13.16±0.15	34.55±1.12	49.42±0.64	64.90±0.87	10.91±0.21

High temperatures and continuous stirring were employed to obtain homogenous pre-gel mixtures following Baumberger *et al.*[15]. Organo-gels were prepared by dissolving 7.5, 10, 12.5 and 15 wt%

gelatin powder (type A from porcine skin, Sigma Aldrich) in mixtures of 70 wt% glycerol–30 wt% deionized water, followed by continuous stirring at 85 °C for 4 hours. This was followed by an additional hour of heating without stirring to allow the air bubbles to escape the pre-gel mixture. The pre-gel mixture was poured into a Petri dish containing the structured PDMS mould placed with its structured side facing up. The liquid gel filled the PDMS mould and rose to a thickness of about 2 mm above the PDMS surface. The liquid wets the PDMS surface completely and upon cross-linking it takes the shape of the PDMS surface (see Appendix 2 and Ref. 9). The pre-gel mixture was allowed to cool and cross-link at room temperature for about 10–15 min after pouring. Subsequently, the mould was placed in a refrigerator at 4 °C for 16.5 hours to complete the gelation process. The gel was then removed and allowed to equilibrate to room temperature for 1 hour prior to demoulding and gel characterization.

The gel and PDMS surface profiles were measured using an optical profilometer (Zemetrics ZeGage, Zygo Corp. CT USA).

Measurement of elastic modulus. Elastic moduli of the gel samples were measured independently by beam-bending and a contact compliance method. In the contact compliance method, a polished steel cylindrical flat probe is indented on the flat surface of a block of gelatine gel (30 × 30 mm and 4–5 mm thick) at a constant speed of 1 μm s^{-1} to a pre-defined indentation depth (~50–150 μm) and retracted at the same speed to the starting position. The indenter radius (~1 mm) is small in comparison to the lateral dimensions of the gel block. The contact was monitored using a microscope. The force and the indentation depth during indentation/retraction were recorded using

a load cell (Honeywell Ltd.) and a capacitive displacement sensor, respectively. The compliance of the sample was determined from the slope of the force versus indentation depth curve and the Young's modulus was computed following Rong *et al.*[16], (details in the Appendix 2). Beam bending tests were additionally performed as an independent modulus measurement (see Appendix 2 for a detailed description). The Young's moduli of the gels range from 14–50 kPa. We also studied the effect of the loading rate by conducting indentations at different rates (0.01–10 μm s^{-1}) and found no significant difference in the measured Young's modulus.

2.3 Results

(a) Periodic ridge geometry h ~ 2.7 and 1.7 μm. Fig. 2.2a shows a 3D surface profile of a PDMS mould with a periodic ridge-channel geometry against which a gel with Young's modulus E = 32.5 kPa was moulded. The measured surface profile of the demoulded gel sample is shown alongside.

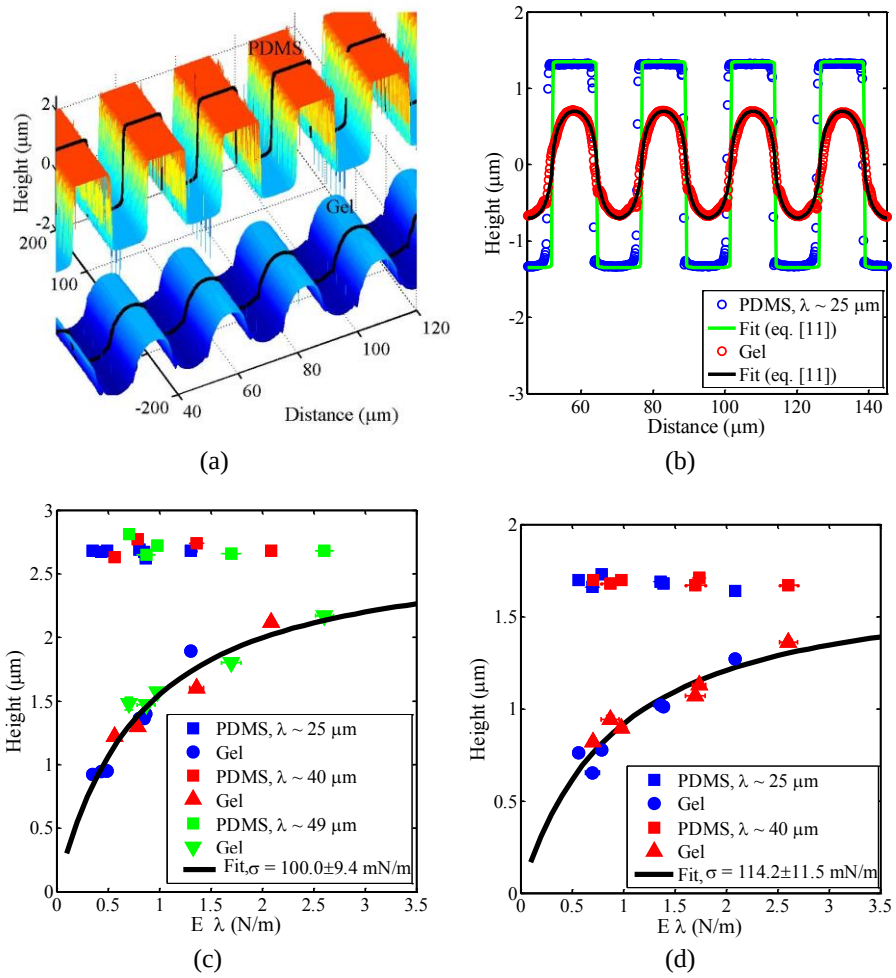

Figure 2.2 (a) Measured 3D surface profile of periodic ridge geometry showing PDMS master and its gel replica for E = 32.5 kPa, $\lambda \sim 25$ μm and initial height $h \sim 2.7$ μm. The black lines over the surface profiles represent the position of the line scan in (b); (b) Line scans of the PDMS and gel surface profiles (circle symbols) and the theoretically predicted PDMS and gel profiles (continuous lines) using eq. (2.9) and a single fitting parameter of σ = 100.0 mN/m for the deformed shape. (PDMS and gel profiles have been shifted with respect to the y-axis such that their mean lies around zero); (c) Final gel height (h_d) (symbols circles, triangles and inverted triangles represent, respectively, spacings $\lambda \sim 25$, 40 and 49 μm) compared to (initial) PDMS (square symbols) with ridge height $h \sim 2.7$ μm (d) $h \sim 1.7$ μm as a function of several elastic moduli (E) and periodic separations (λ). Least Square fits using eq. (2.9) (solid black lines in (c) and (d)) estimate the surface stress to be 100.0±9.4 mN/m and 114.2±11.5 mN/m (95% confidence) for $h \sim 2.7$ and 1.7 μm respectively.

We observe that the gel profile is significantly rounded compared to the sharply edged periodic ridges of the PDMS master into which it was moulded. The deformed height (h_d) and the rounding of the edges create a sinuous profile, which can be seen from the line scans (Fig. 2.2b) of the surfaces of the gel sample and the PDMS master. Using small strain theory the entire surface profiles (eq. (2.9) below, continuous lines, Fig. 2.2b) for the PDMS (which is the same as the undeformed gel for σ = 0 mN m^{-1}) and the deformed gel (σ = 100 mN m^{-1}) were evaluated and plotted alongside experimental data. For the shallow profiles, the theory based on small strain elasticity fits the data well.

Fig. 2.2c and d show the measured ridge height of PDMS master (h) (square symbols) and its gel replica (h_d) after demoulding. The maximum height (peak to valley) of the deformed sample (h_d) is plotted against the product of periodic spacing (λ) and elastic modulus (E) of the gels (symbols: circles, triangles and inverted triangles represent, respectively, spacings $\lambda \sim$ 25, 40 and 49 μm). A systematic reduction in the gel height h with reduction in the gel modulus was observed. Least square fits to the experimental data using the small strain theory (eq. (2.9)) are plotted for the two initial heights, $h \sim$ 2.7 μm (Fig. 2.2c) and $h \sim$ 1.7 μm (Fig. 2.2d). The fits are generated using a single fitting parameter, the mean surface stress, of σ = 100.0 and σ = 114.2 mN m^{-1} for h ~ 2.7 and 1.7 μm, respectively. We further determined the accuracy of the fitted surface stress[17] and found, with a confidence of 95%, that σ = 100.0 ± 9.4 mN m^{-1}.

(b) Analysis of deformation driven by surface stress. To analyse the shape change we assume that deformation is driven by the surface stress. Further, we have assumed that the boundaries are

traction free and the material is elastic. There is little change observed experimentally in the dimension parallel to the ridges, hence we use a plane strain condition.

When the ridges are shallow, the deformation is small, and a closed form approximate solution can be obtained based on a scheme used by Hertz to compute the deformation of elastic spheres in contact [18]. Specifically, instead of applying the Laplace pressure on the deformed surface, which is not flat, we determine the deformation caused by the Laplace pressure by imposing it on a flat elastic half space. This procedure is valid provided that the curvature of the deformed surface is small. Since periodic ridge surface profiles can be represented by a Fourier series, the undeformed surface profile y_0 is

$$y_0 = c_0 + \sum_{n=1}^{\infty} a_n^0 cos\left(\frac{2\pi nx}{\lambda}\right) \tag{2.1}$$

where $\left(c_0, a_n^0\right)$ are Fourier coefficients. The deformed surface profile, after peeling the gel off the PDMS master is given by

$$y = c + \sum_{n=1}^{\infty} a_n cos\left(\frac{2\pi nx}{\lambda}\right) \tag{2.2}$$

The Laplace pressure p that causes the surface flattening is equal to the product of surface stress and curvature which we assume to be small. Using (2.2),

$$p = \sigma y'' = -\sum_{n=1}^{\infty} a_n \sigma \left(\frac{4\pi^2 n^2}{\lambda^2}\right) cos\left(\frac{2\pi nx}{\lambda}\right) \tag{2.3}$$

The Laplace pressure is calculated based on the unknown final shape (eq. (2.2)), not the initial shape. For this reason, although the kinematics and elasticity is linear, the final result relating the shape change to the surface stress that drives it is nonlinear. As mentioned earlier, the vertical displacement u caused by the Laplace pressure (eq. (2.3)) was computed based on the elastic solution of a periodic normal traction acting on the surface of a flat elastic half space.[19] Using superposition, u is found to be:

$$u = -\sum_{n=1}^{\infty} 4\pi \left(\frac{a_n n}{\lambda} \right) \left(\frac{\sigma}{E^*} \right) cos\left(\frac{2\pi n x}{\lambda} \right) \tag{2.4}$$

The final and the initial shapes of the surface are related to each other by

$$y = y_0 + u \tag{2.5}$$

The relationship between the Fourier coefficients of y_0 and y can be found using (2.1), (2.2), (2.4) and (2.5), which results in

$$a_n = \frac{a_n^0}{1 + 4\pi \left(\frac{\sigma n}{\lambda E^*} \right)}; c = c^0 \tag{2.6}$$

Eq. (2.6) shows that the higher Fourier modes (larger n) are attenuated by surface stress to a greater extent than are modes with smaller n. The Fourier coefficients of the undeformed profiles are

$$a_n^0 = \frac{2h}{n\pi} sin\left(\frac{n\pi w}{\lambda} \right); c_0 = \frac{hw}{\lambda} \tag{2.7}$$

The shape of the deformed profile can be found using (2.6), (2.7) and (2.2), resulting in

$$y = \frac{hw}{\lambda} + \frac{2h}{\pi}\sum_{n=1}^{\infty}\frac{sin\left(\frac{n\pi w}{\lambda}\right)}{n\left[1+4\pi\left(\frac{\sigma n}{\lambda E^{*}}\right)\right]}cos\left(\frac{2\pi nx}{\lambda}\right) \tag{2.8}$$

The peak to valley height of the deformed profile is

$$h_d = \sum_{n=1}^{\infty}a_n - \sum_{n=1}^{\infty}(-1)^n a_n = \frac{4h}{\pi}\sum_{n=1}^{\infty}\frac{\sin\left[\frac{(2n-1)\pi w}{\lambda}\right]}{(2n-1)\left(1+4\pi\frac{\sigma(2n-1)}{\lambda E^{*}}\right)} \tag{2.9}$$

Fig. 2.3 shows the shape change of a gel replica with increasing surface stress predicted using eq. (2.8) (500 terms were included in the calculation). As seen already in Fig. 2.2b, compared to the initial sharp edges present in the periodic ridge profile, the deformed shape of the gel has significantly rounded edges.

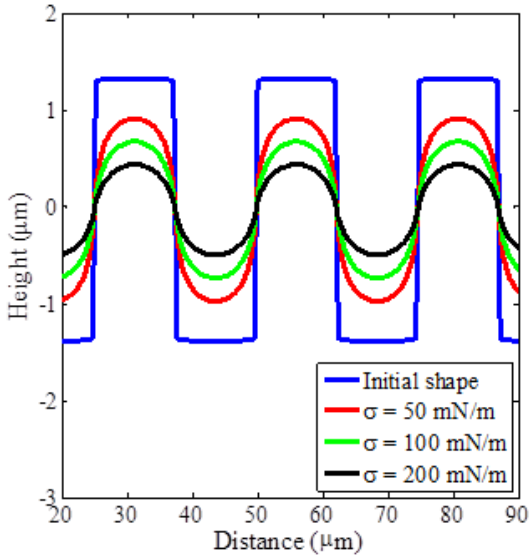

Figure 2.3 Prediction of final shape of the gel profile based on eq. (2.8) for a low height (h ~ 2.7 μm) periodic ridge geometry with Young's modulus E = 33 kPa and λ ~ 25 μm. Surface stress σ increases from 50 -200 mN/m.

Eq. (2.8) and (2.9) were used to fit the data shown in Fig. 2.2.

(c) Deformation of deeper ridge geometry h ~ 13 μm. Compliant materials are often structured by moulding into a master made of much stiffer material and it is common for feature height to be about the same size as other dimensions such as width or spacing. For such cases, deformation can be significantly larger and its analysis requires numerical methods. Here we demonstrate that a finite element analysis of larger deformations can be used to model this more general situation of surface-stress-driven deformation.

A straightforward dimensional analysis shows that

$$\frac{h_d}{h} = f\left(\frac{\sigma}{\lambda E}, \frac{w}{\lambda}, \frac{h}{\lambda}\right) \tag{2.10}$$

where h_d is the deformed height for a ridge geometry with initial height h. In the case of shallow ridge, $h/\lambda << 1$, for the small-strain solution in eq. (2.9), the ratio $\frac{h_d}{h} = f\left(\frac{\sigma}{\lambda E}, \frac{h}{\lambda}\right)$ is independent of h/λ. However, when h/λ is large, the Hertz approximation is no longer valid, hence eq. (2.9) is not applicable. For these high ridge geometries, we carried out FEM analysis with a two dimensional plane strain model using ABAQUS®/Standard 6.8 to simulate the surface deformation. Since the length of the ridges is very long in comparison with its lateral dimensions, a plane strain model is used. The predicted deformed surface profile was fitted to that obtained by experiment using surface stress as a fitting parameter.

In all our simulations, the gel was modelled as an incompressible neo-Hookean material [20] with a strain energy density function

$$W = \frac{\mu}{2}(I_1 - 3), \qquad I_1 = \lambda_1^2 + \lambda_2^2 + \lambda_3^2 \tag{2.11}$$

where I_1 is the first invariant of the left Cauchy–Green deformation tensor, λ_i's are the principal stretch ratios and $\mu = E/3$ is the small strain shear modulus.

The surface stress σ, is assumed to be a material constant independent of deformation and composition [3]. Surface tension was modelled by augmenting the finite element model by a set of user-defined 2-node linear surface elements, which discretize the exposed gel surface [21]. Since the deformed surface is a long cylinder, one of the principal curvatures is zero; let the other be denoted

by κ. The tractions **T** on the deformed solid body are related to the rate of change of tangent **t** to the surface, i.e., the surface curvature, by the Young–Laplace equation

$$\mathbf{T} = \frac{\sigma d\mathbf{t}}{ds} \tag{2.12}$$

where s is the arc length of the deformed cross-section curve. Hence the net nodal force applied on the body due to a small patch of surface spanning two surface elements is

$$\mathbf{F} = \int_1^2 \mathbf{T} ds = \sigma\left(\mathbf{t}_2 - \mathbf{t}_1\right) \tag{2.13}$$

where **t** is the tangent vector of the surface elements, 1 and 2 refer to the surface elements before and after the node [21].

Fig. 2.4 shows the deformed shape of a typical demoulded gel sample (E = 44 kPa, σ = 200 mN m^{-1}) predicted by FEM simulation.

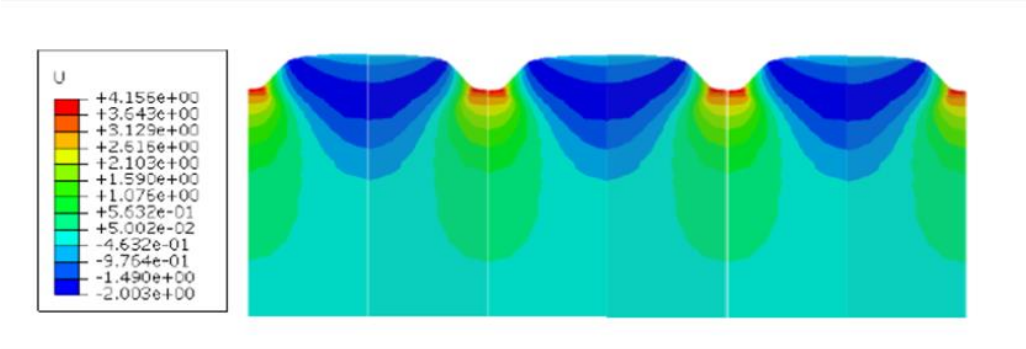

Figure 2.4 Deformed configuration of a typical demoulded gel sample predicted by FEM simulation for E = 44 kPa, σ = 200 mN/m. Contours represents the vertical displacement U (μm).

Fig. 2.5 shows the deformed surface profile calculated by FEM for a high ridge geometry (h = 13 μm, λ = 34.15 μm, w = 11 μm, E = 44 kPa) in the experiment with increasing surface stress. As expected, a larger value of surface stress causes more rounding at the edges and lower deformed height.

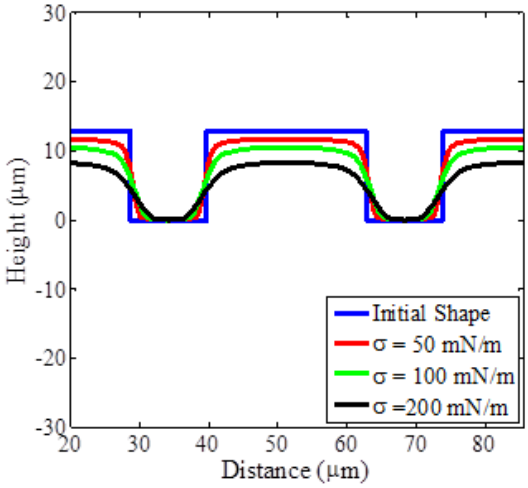

Figure 2.5 Simulation results for the shape deformation of the high periodic ridge geometry (h = 13 μm) with a Young's modulus E = 44 kPa and λ =34.15 μm as a function of increasing surface stress.

Fig. 2.6 shows the line scans (circle symbols) across the measured surface profile of a PDMS master and its gel replica (E = 35 kPa, $\lambda \sim$ 35 μm) for the case of ridge height $h \sim$ 13 μm. The least square fit results using FEM analysis are also presented alongside. The ratio of the deformed gel height h_d to the initial height h of the PDMS master (square symbols) is plotted in Fig. 2.6b for three different periodic spacings λ (symbols: circles, triangles and inverted triangles represent, respectively, spacings of $\lambda \sim$ 35, 50 and 65 μm, see Table 2.1) and five different moduli (E). Using least square fits based on the FEM model a surface stress value of 130.0 ± 21.5 mN m^{-1} was

estimated (lines in Fig. 2.6b). The surface profile predicted by FEM simulation closely matches the experimental result as shown in Fig. 2.6a. As previously stated, the precision of the fitted surface stress represents a 95% confidence interval [17]. The data showing the deformed gel heights h_d in comparison to their starting ridge height are given in Appendix 2. The values of surface stress obtained in this case are similar to those estimated for shallow ridge geometry.

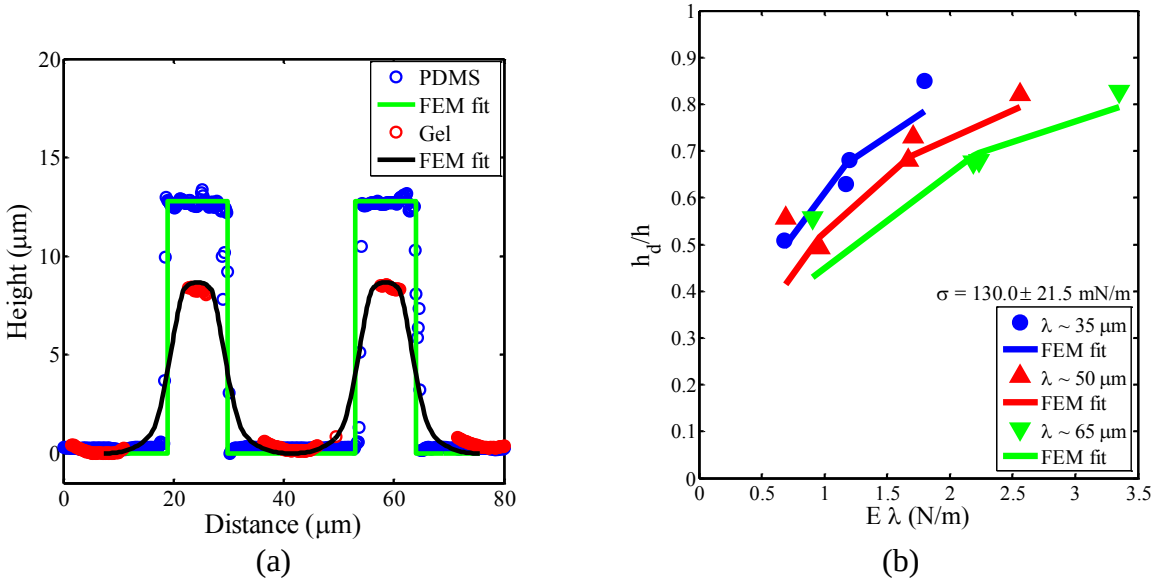

Figure 2.6 (a) Line scans across measured surface profile of periodic ridge geometry for PDMS master and its gel replica (circle symbols) with E = 35 kPa, λ ~ 35 μm and initial height h ~ 13 μm. Predicted shape for the PDMS and gel profile (continuous lines) using FEM analysis. (b) Measured reduction in gel height (ratio of deformed to initial height, h_d/h) as a function of several elastic moduli (E) and periodic separations (λ); symbols circles, triangles and inverted triangles represent, respectively, spacing 35, 50 and 65 μm. Least square fit of FEM results to experimental data yields an estimate of the surface stress as 130.0±21.5 mN/m.

FEM analysis for the case of h ~ 2.7 μm (see Appendix 2) yielded a value of 105.0 ± 17.6 mN m^{-1} for surface stress, in good agreement with that obtained using small strain theory, 100.0 ± 9.4 mN

m^{-1}. The difference in surface stress needed (130 mN m^{-1}) for the higher profile samples could be due to departure from the neo-Hookean model used – our purpose here is mainly to demonstrate that larger surface-stress deformations can be modelled numerically.

2.4 Discussion and Conclusions

We measured and characterized surface deformations in patterned organo-gels due to their surface stress. When a gel moulded into a patterned (PDMS) master is subsequently separated from it, a new gel–air interface is created. This interface has a surface stress, in response to which the gel deforms, setting up internal stresses that balance the surface stress. We show that the surface stress is able to drive significant deformation owing to the relatively low elastic moduli of the gels.

The characteristic strains encountered for samples with a shallow profile are of the order of $2\pi(h - h_d)/\lambda$, which is small compared to unity, indicating that strains in the sample are generally small except at the corners, where strains are very large (if the corner is perfectly sharp, the strain is theoretically infinite). For shallow-profile samples, since $h/\lambda << 1$ and the average strain is small, we employed an analytical model based on periodic loading of a flat surface. The periodic surface is represented by a Fourier series and the higher Fourier modes of the surface profile suffer greater deformation (eq. (2.3) and (2.9)) [9, 22]. The predicted gel profiles using small strain theory for shallow geometry as well as the FEM analysis in the high ridge geometry case match the experimentally measured profiles quite well (Fig. 2.2b and 2.3a). We estimated surface stress σ =

100.0 ± 9.4 and 114.2 ± 11.5 mN m^{-1}, respectively for $h \sim 2.7$ and 1.7 μm (with an average of the two estimates of surface stress $\sigma = 107 \pm 7$ mN m^{-1}).

For the case of high ridges ($h \sim 13$ μm), the characteristic strains are moderately large, of the order of $2\pi(h - h_d)/h > 100\%$. Using a FEM model in which the gel was assumed to be incompressible with neo-Hookean elasticity, we showed how such deformations can be modelled. We have assumed a single surface tension value for a given set of samples independent of their solid content and its surrogate, the elastic modulus. The quality of the resulting fits generally supports this hypothesis. Because the gel composition is dominated by the solvent, which constitutes roughly 90% of the solid gel, it would appear that surface stress should be determined primarily by surface tension of the water–glycerol mixture. However, the overall surface stress of 107 ± 7 mN m^{-1} is significantly higher than that expected from the surface tension values of the glycerol–water mixture (for aqueous glycerol with ~60 wt% glycerol, surface tension $\sigma = 68.5$ mN m^{-1} (ref. 23)). One possibility is that the ternary system (solid component and the two liquids that constitute the gel) forms significantly different structures. We hypothesize the formation of a new surface structure to explain the high overall stress. Water–glycerol mixtures with high concentrations of glycerol (>60 wt%) have been known to show enhancement of structured water [24]. Timasheff [25] found that a perturbation in the chemical potential of glycerol in the presence of the polypeptide protein gelatine results in the formation of new ternary phases consisting of water–gelatine–glycerol. Sanwlani *et al.* have shown, using Raman analysis, that for such a ternary system glycerol enhances structuring of water molecules (ice-like structure) causing gelatine molecules to compartmentalize to regions where glycerol-free water is available [24]. We point to the plausibility

that a new structure of the water–glycerol–gel–solid mixture could result in surface stress that differs from what one would expect from a rule of mixtures.

The confidence in the estimated surface stress values also depends on the accuracy and the precision of independently measured Young's moduli of the gels. Two methods, beam bending and load-displacement measurements with a flat punch, were employed to determine the modulus. The possible inaccuracy in the independent measurement of the modulus limits the accuracy of the presented surface tension data.

The periodic ridge geometry is relatively easy to fabricate and may serve as a model for determination of the surface stress of compliant solids. For cases where patterned surfaces are shallow ($h << \lambda$) the application of small strain elasticity theory successfully estimates the surface stress if the elastic properties of the gel are independently known. For the more general case, we have shown how finite element analysis can be used to analyse arbitrary deformation driven by surface tension.

Arrays of parallel channels are routinely fabricated in applications such as microfluidics using replica moulding. Our work shows that when soft elastomers or gels are used in the fabrication, the shape of replica can be significantly different from the original mould. The analysis in the work presents a methodology to characterize the final shape of these replicas.

Acknowledgements

This work was supported primarily by the U.S. Department of Energy, Office of Basic Energy Sciences, Division of Materials Science and Engineering under award DEFG02-07ER46463. DP was supported partially (1/3rd of his total time spent on this project) by INM-Leibniz Institute for New Materials and would like to thank Prof. E. Arzt for this support. AJ would like to acknowledge the suggestion of A. Ghatak (Indian Institute of Technology, Kanpur) for measurement of modulus by beam bending under its own weight.

Appendix 2 Supplementary Information

Determination of Young's modulus

a) Cylindrical Punch Indentation Experiment

The purpose of this brief note is to put down the relations needed to extract Young's modulus from a compliance measurement made by indenting a sample using a rigid cylindrical punch.

In the schematic Fig. A.2.1, a circular cylindrical punch with radius a indents an elastic foundation that is very large in the plane of the contact, i.e., $L>>a$. However, its thickness, h, may or may not be large compared to a.

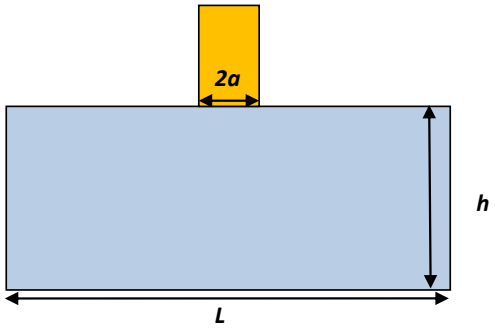

Figure A.2.1 Schematic of flat cylindrical punch with diameter *2a* used to indent a gel block of height *h* and diameter *L*.

In the limit when $h>>a$, we have indentation by a rigid circular punch of an elastic half space. In this case [16, 24],

$$\left.\frac{d\delta}{dP}\right|_{h/a\to\infty} = C_\infty = \frac{1}{2E^*a} \tag{A.2.1}$$

where δ is the displacement of the indenter, P is the measured load, C_∞ is the compliance in the limit $h>>a$ or $h/a\to\infty$, $E^* = E/\left(1-\nu^2\right)$ is the plane strain Young's modulus, and ν is Poisson's ratio. If the material is incompressible, then $\nu = 1/2$, and equation (A.2.1) becomes

$$\left.\frac{d\delta}{dP}\right|_{h/a\to\infty} = C_\infty = \frac{1}{2E^*a} = \frac{1-\nu^2}{2Ea} = \frac{3}{8Ea} = \frac{1}{8Ga} \tag{A.2.2}$$

where we have used the relation $G = E/\left(2\left(1+\nu\right)\right)$. This is the same result as given in Long *et al.*[16] (equations 24 a, b) who have additionally shown that for finite *h*, the compliance *C*, can be written in terms of C_∞ in the following way:

$$\frac{d\delta}{dP} = C = C_\infty \frac{1}{\left(1+\chi(\eta)\right)};\ \eta = a/h$$
$$\chi(\eta) = \left(1.095\eta + 1.3271\eta^2 + 0.1431\eta^4\right)/0.9717 \qquad \text{(A.2.3)}$$

So, since C is the measured quantity, our expression for Young's modulus is

$$E^* = \frac{1}{2aC}\frac{1}{\left(1+\chi(\eta)\right)};\ \eta = a/h$$
$$\chi(\eta) = \left(1.095\eta + 1.3271\eta^2 + 0.1431\eta^4\right)/0.9717 \qquad \text{(A.2.4)}$$

A typical load-displacement plot is shown in Fig. A.2.2.

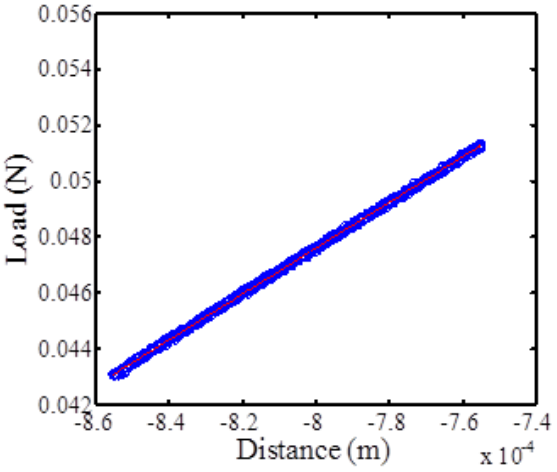

Figure A.2.2 Load measured as a function of indentation depth (Distance) in a typical contact compliance test. The compliance C is the inverse of the slope.

b) Beam bending

The modulus was measured using the linear elastic moment-curvature relationship of beam theory

$$M = EI\kappa \tag{A.2.5}$$

where M is the moment on the beam fixed at one end, I is the moment of inertia of the rectangular cross-section of the beam and κ is the curvature of the bent beam.

Equation (A.2.5) can be re-written in terms of the distance s along the neutral axis of the beam

$$\frac{M(s)}{EI} = \frac{d\theta}{ds} \tag{A.2.6}$$

Integrating (A.2.6),

$$\int M(s)\,ds = EI \int d\theta \tag{A.2.7}$$

That is, the integral of the moment is linearly related to change in angle, and the slope is EI. The integral of the moment is plotted as a function of the angle and from the slope the modulus is obtained (Fig. A.2.3).

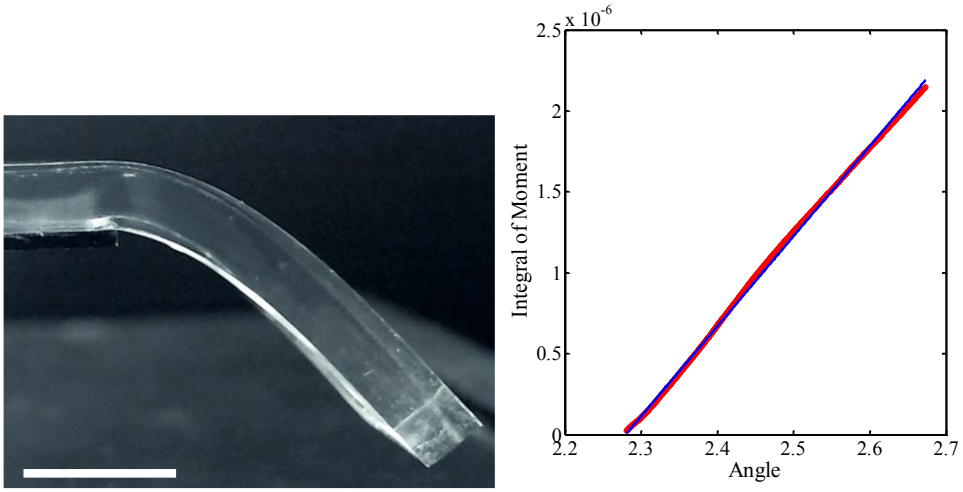

(a) (b)

Figure A.2.3 (a) Picture of a gel beam fixed at one end and freely hanging on the other (scale bar ~ 1cm). The profile of the beam is read using MATLAB code for determination of the curvature. (b) Integral of moment versus angle plot.

Confirmation that gel fills the patterned PDMS

We re-confirmed the assumption that the liquid gel wets the PDMS master completely. A section of the PDMS master was cut and laid flush on the bottom of the petri-dish such that the ridges were orientated perpendicular to it. After filling and gelation images were taken through the transparent base of the petri-dish. Fig. A.2.4 shows the optical micrographs of gel filled PDMS master.

(a) (b)

Figure A.2.4 Optical micrographs (scale bar 100 μm) of gel (E ~ 23 kPa) filled PDMS master prior to moulding for periodic ridge geometry (a) h ~ 13 μm, λ ~ 35 μm and (b) h ~ 2.7 μm, λ ~ 25 μm .

High ridge geometry height reduction

In the experimental results part of the main text we noted the variation of the ratio of deformed to initial height for the high ridge geometry. Fig. A.2.5 shows the absolute heights of the PDMS and the deformed gel samples for the ridge geometry with h ~ 13 μm. A lower deformed height (h_d) was measured for a gel with lower modulus (E).

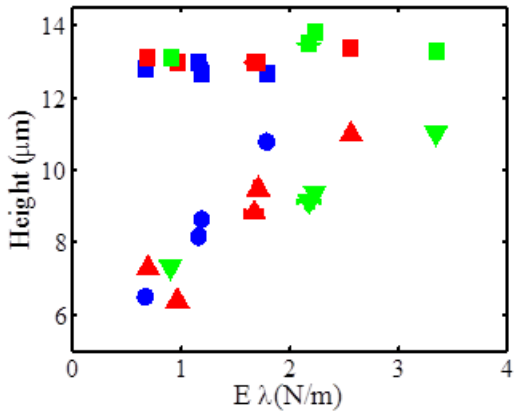

Figure A.2.5 Measured initial height of ridge/channel in PDMS h ~ 13 μm (square symbols) and the corresponding gel height (h_d) for three different periodic spacing λ (symbols circles, triangles and inverted triangles represent, respectively, spacing of λ ~ 35, 50 and 65 μm, see Table 2.1 ($\lambda = s+w$) and five different moduli (E).

FEM analysis for low height (h~ 2.7 µm)

To test the validity of the small strain theory, we applied also applied the FEM analysis to the case of shallow ridges for which small strain theory satisfactorily predicted the full deformed profile of the gel after demoulding. Fig. A.2.6 shows that the least square fitting results of FEM analysis to experimental data yield a surface tension σ of 105.0±17.6 mN/m which quite similar to that obtained from the small strain theory (σ = 100.0±9.4 mN/m).

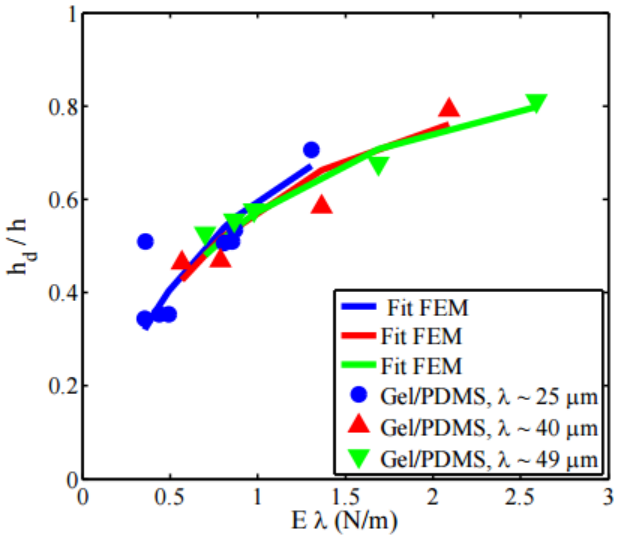

Figure A.2.6 Measured reduction in gel height (ratio of final to initial height) and FEM analysis based least square fits (continuous h/h_0 lines) for the height reduction as a function of varying elastic moduli E and three different periods λ (symbols circles, triangles and inverted triangles represent, respectively, spacing of λ ~ 25, 40 and 49 µm).

FEM analysis: Validity of neo-Hookean model

We applied an alternate model to the neo-Hookean to ascertain its validity. The linear elastic model was used to estimate the deformed heights. (Fig. A.2.6). We observe that for the surface tension

of approximately 110 mN/m, which is close to estimated surface stress for low strain case, the two models deviate by less than 8% (Fig. A.2.7).

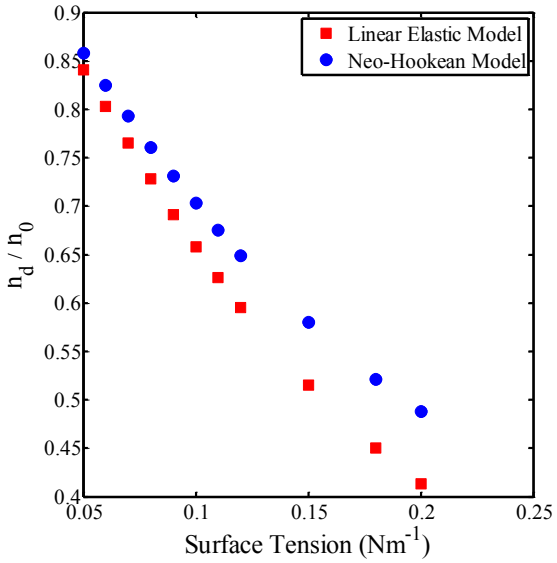

Figure A.2.7 Comparison of deformed heights for a given surface tension for the neo-Hookean versus linear elastic material models.

References

[1]. Shuttleworth, R. (1950). The surface tension of solids. Proceedings of the Physical Society. Section A, 63(5), 444.

[2]. Cammarata, R. C., & Sieradzki, K. (1994). Surface and interface stresses. Annual Review of Materials Science, 24(1), 215-234.

[3]. Hui, C. Y., & Jagota, A. (2013). Surface tension, surface energy, and chemical potential due to their difference. Langmuir, 29(36), 11310-11316.

[4]. Hui, C. Y., Jagota, A., Lin, Y. Y., & Kramer, E. J. (2002). Constraints on microcontact printing imposed by stamp deformation. Langmuir, 18(4), 1394-1407.

[5]. Roman, B., & Bico, J. (2010). Elasto-capillarity: deforming an elastic structure with a liquid droplet. Journal of Physics: Condensed Matter, 22(49), 493101.

[6]. Mora, S., Phou, T., Fromental, J. M., Pismen, L. M., & Pomeau, Y. (2010). Capillarity driven instability of a soft solid. Physical review letters, 105(21), 214301..

[7]. Jerison, E. R., Xu, Y., Wilen, L. A., & Dufresne, E. R. (2011). Deformation of an elastic substrate by a three-phase contact line. Physical Review Letters, 106(18), 186103.

[8]. Marchand, A., Das, S., Snoeijer, J. H., & Andreotti, B. (2012). Capillary pressure and contact line force on a soft solid. Physical review letters, 108(9), 094301.

[9]. Jagota, A., Paretkar, D., & Ghatak, A. (2012). Surface-tension-induced flattening of a nearly plane elastic solid. Physical Review E, 85(5), 051602.

[10]. Gibbs, J. W. (1878). On the equilibrium of heterogeneous substances. American Journal of Science, (96), 441-458.

[11]. De Gennes, P. G., Brochard-Wyart, F., & Quéré, D. (2013). Capillarity and wetting phenomena: drops, bubbles, pearls, waves. Springer Science & Business Media.

[12]. Style, R. W., Boltyanskiy, R., Che, Y., Wettlaufer, J. S., Wilen, L. A., & Dufresne, E. R. (2013). Universal deformation of soft substrates near a contact line and the direct measurement of solid surface stresses. Physical review letters, 110(6), 066103.

[13]. Nadermann, N., Hui, C. Y., & Jagota, A. (2013). Solid surface tension measured by a liquid drop under a solid film. Proceedings of the National Academy of Sciences, 110(26), 10541-10545.

[14]. Singh, A. K., Bai, Y., Nadermann, N., Jagota, A., & Hui, C. Y. (2012). Adhesion of microchannel-based complementary surfaces. Langmuir, 28(9), 4213-4222.

[15]. Baumberger, T., Caroli, C., & Martina, D. (2006). Solvent control of crack dynamics in a reversible hydrogel. Nature materials, 5(7), 552-555.

[16]. Long, R., Hui, C. Y., Kim, S., & Sitti, M. (2008). Modeling the soft backing layer thickness effect on adhesion of elastic microfiber arrays. Journal of Applied Physics, 104(4), 044301.

[17]. Berendsen, H. J. (2011). A student's guide to data and error analysis. Cambridge University Press.

[18]. Hertz, H. (1896). Miscellaneous papers. Macmillan.

[19]. Johnson, K. L. Contact mechanics, 2003. Cambridge University Press, UK. ISBN 0, 521(34796), 3.

[20]. Ogden, R. W. (1997). Non-linear elastic deformations. Courier Corporation.

[21]. Xu, X., Jagota, A., Peng, S., Luo, D., Wu, M., & Hui, C. Y. (2013). Gravity and surface tension effects on the shape change of soft materials. Langmuir, 29(27), 8665-8674.

[22]. Hui, C. Y., Jagota, A., Lin, Y. Y., & Kramer, E. J. (2002). Constraints on microcontact printing imposed by stamp deformation. Langmuir, 18(4), 1394-1407.

[23]. Sanwlani, S., Kumar, P., & Bohidar, H. B. (2011). Hydration of Gelatin Molecules in Glycerol–Water Solvent and Phase Diagram of Gelatin Organogels. The Journal of Physical Chemistry B, 115(22), 7332-7340.

[24]. Timasheff, S. N. (2002). Protein-solvent preferential interactions, protein hydration, and the modulation of biochemical reactions by solvent components. Proceedings of the National Academy of Sciences, 99(15), 9721-9726.

[25]. Vajpayee, S., Long, R., Shen, L., Jagota, A., & Hui, C. Y. (2009). Effect of rate on adhesion and static friction of a film-terminated fibrillar interface. Langmuir, 25(5), 2765-2771.

CHAPTER 3

SURFACE TENSION MEASUREMENT FROM INDENTATION OF CLAMPED THIN FILMS *

Abstract

We developed an indentation technique to measure the surface tension of relatively stiff solids. In the proposed method, a suspended thin solid film is indented by a rigid sphere and its deflection is measured by optical interferometry. The film deflection is jointly resisted by surface tension, elasticity and residual stress. Using a version of nonlinear von Karman plate theory that includes surface tension, we are able to separate the contribution of elasticity to the total tension in the film. Surface tension is determined by extrapolating the sum of surface tension and residual stress to zero film thickness. We measured surface tension of polydimethylsiloxane (PDMS) using this technique and obtained a value of 19.5 mN/m, consistent with the surface energy of PDMS reported in the literature.

---

* Xu, X., Jagota, A., Paretkar, D. and Hui, C.Y., (2016) submitted to *Soft Matter*.

3.1 Introduction

It has been known for a long time that surface stresses exist in solids [1-4]. While the effects of surface stresses on the mechanical behaviour of stiff materials are typically negligible, these stresses can dominate the behaviour in soft materials. For example, surface stress can flatten soft patterned surfaces [5], causes large local deformation at the contact line of a liquid drop resting on a soft substrate [6-10] and drives instabilities in very soft gels [11, 12]. In other situations, surface tension can resist deformation, for example, in the studies of liquid droplets on a thin film [13-16], nucleation of creases in soft solid surface [17] and surface instability of a strained soft solid [18].

Surface stresses and surface energies in solids are different in two important ways. First, surface energy is a scalar while surface stress $\boldsymbol{\sigma}_s$ is a 2D tensor [19]. Even when surface stress is isotropic, that is $\boldsymbol{\sigma}_s = \sigma \mathbf{I}_s$, where $\mathbf{I}_s$ is the 2D isotropic surface tensor (σ is commonly called the surface tension), surface energy need not be numerically equal to surface tension. The range of length scales, over which surface tension dominates bulk elasticity, can be characterized by an elasto-capillary length σ / E, where E is the Young's modulus [20]. For compliant solids (E < 100 kPa), this length is usually larger than micrometre scale. Their surface tensions can be measured by monitoring the deformed solid surface in regions where surface tension is dominant [5-6]. However for stiff solids, the elasto-capillary length is on the order of nanometres or smaller, and hence the effect of surface tension can be neglected in typical engineering structures. Nevertheless, even in stiff solids, its effect can be amplified using slender geometries. Examples include bending of a micro-cantilever with different surface tensions on each of its sides [4, 21], deformation of a thin film

induced by liquid droplets [13-16], bulging of thin polymer films [22-24] as well as bending of metallic nanowires and polymer nanotubes [25-26]. Therefore, the surface tension of a stiff material could be indirectly determined by monitoring its deformation using a slender sample geometry. Most existing methods [21-22, 26-27] using this approach require nanoscale samples and are hence limited by sample fabrication and measurement resolution.

In this work, we propose a method to determine the surface tension of a relatively stiff polydimethylsiloxane (PDMS) material by monitoring the deflection of clamped circular thin film samples by a rigid indenter. The idea behind this proposed technique is similar to the key finding of a previous work [13, 14], in which we showed that the deflection driven by the capillary forces of a liquid drop on a thin PDMS film is resisted by a combination of elasticity and surface tension in the film. In this present work, elasticity and surface tension (along with other possible bulk residual stresses resulting from film preparation) both act to resist the film deflection by the rigid indenter. The pre-tension in the film, consisting of surface tension and residual stresses, is extracted by analysing the deflected film profile using a model that accounts for both bending and stretching of the film. Since the portion of the pretension (N/m) due to residual stresses increases linearly with thickness while the part due to surface tension does not, linear extrapolation of total tension to zero film thickness provides an estimate of the surface tension.

There are two principal differences in the work presented here compared to our previous work [13, 14]: (a) a rigid indenter (rather than capillary forces) is used to drive the deformation, and (b) the

mechanical response of the film is analysed to separately account for the contributions of elasticity, surface tension and residual stress to the deformation of the film.

3.2 Experiments

(a) Suspended circular thin film. The sample comprised a thin PDMS film bonded on top of an annulus made of the same material. A side view of our experimental setup is shown in Fig. 3.1(a). Preparation of samples was similar to that described by Nadermann *et al.* [13], with a few key differences. PDMS liquid thin films were spun onto polystyrene-coated glass slides and pre-cured for 16 hours before the solid PDMS substrates were placed onto the thin films. Together, the samples were cured for over 48 hours. The curing of PDMS (substrates and films) was conducted at room temperature (25 ˚C) to minimize thermal and shrinkage-induced residual stresses. Five films of thicknesses in the range of 7-20 μm were used in the experiment.

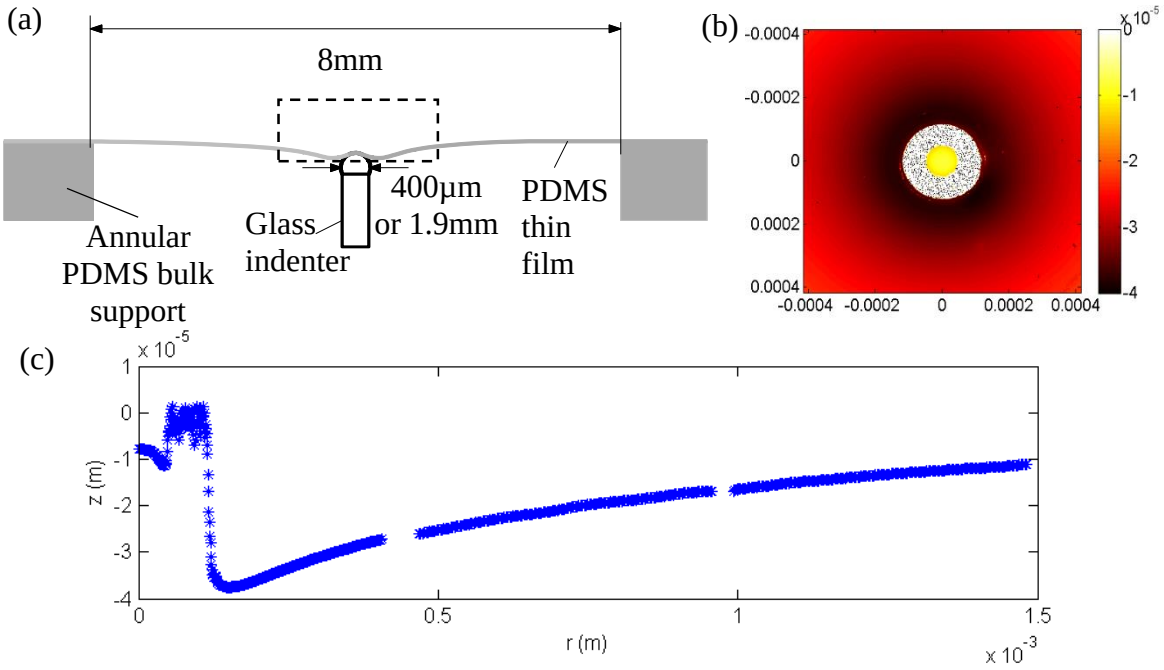

Figure 3.1 (a) A schematic of the side view of the experimental setup. (b) Profile of the top surface of a film (~12 µm thick) deflected by a spherical glass indenter, showing the contact (yellowish circle) in the centre between the film and indenter. (c) Deflections at points of equal distance from the sphere centre are averaged and plotted versus the distance. The azimuthally averaged radial deflection profile corresponds to the portion of the film inside the dashed box in (a).

(b) Indentation of the film. A glass indenter with spherical end of radius 200 µm (or 0.95 mm for the two thicker films) was centred and then brought into contact with a clamped thin circular PDMS film. A motion controller (3 Axis Motion Controller/Driver, Newport) was used to move the indenter in small steps to achieve different contact radii and deflections of the film.

(c) Young's modulus and thickness measurements. Leftover PDMS liquid from the spin coating of thin films were poured into weighing dishes and went through the same curing cycle as the film samples to form thick slabs of PDMS bulk solids (>5 mm thick). We then measured the Young's modulus of these PDMS bulk solids using indentation tests. The Johnson-Kendall-Roberts (JKR)

model [28] was used to extract Young's modulus from the load versus contact radius curve. Our film samples have Young's moduli of approximately 770 kPa with the exception of the 12 μm film of 630 kPa due to shorter aging time. Film thicknesses were measured by a white light interferometer (Zegage; Zygo Corporation) with a resolution of about 2 nm. The five film thicknesses measured are 7.5 μm, 9.5 μm, 12 μm, 17.5 μm and 20 μm. See Appendix 3.1 for details on the indentation test and thickness measurements.

(d) Deformation measurements. Deflections of the films were monitored from above by a white-light interferometer (Zegage; Zygo Corporation) with a resolution of about 2 nm. Fig. 3.1(b) shows a deflected profile of the top surface of the PDMS film (~12 μm thick). Deflections along radial lines were extracted using ZMAP functions in MatLab®, and the azimuthally averaged radial deflection profiles (as plotted in Fig. 3.1(c)) were used to fit against the results obtained from the numerical model. On initial contact, the surface profile was usually axisymmetric. However as the indenter moved to obtain different deflections, axisymmetry could be lost due to imperfect alignment. In such cases, data were not used in fitting.

3.3 Numerical Model

For many isotropic materials, the surface stresses are expected to be approximately isotropic [4, 29]. We assume that the surface of PDMS film is isotropic and homogeneous, hence the surface stress of the PDMS film is an isotropic surface tensor characterized by its surface tension σ_{sv}. Since the maximum deflections in our experiments were no more than several times of the film thicknesses, we used a modified von Karman plate model [30] to capture both the bending and stretching of the

deflected films. The part of film outside the contact is modelled as a pre-stressed thin annular plate. Specifically, the undeformed film is assumed to be under a pre-biaxial tension T_0, which includes the contribution of surface tension and any bulk residual stresses in the film. Fig. 3.2 shows the deformed configuration of the plate (grey) and the spherical indenter in a cylindrical coordinate system (r, θ, z) with the origin placed at the centre of the film.

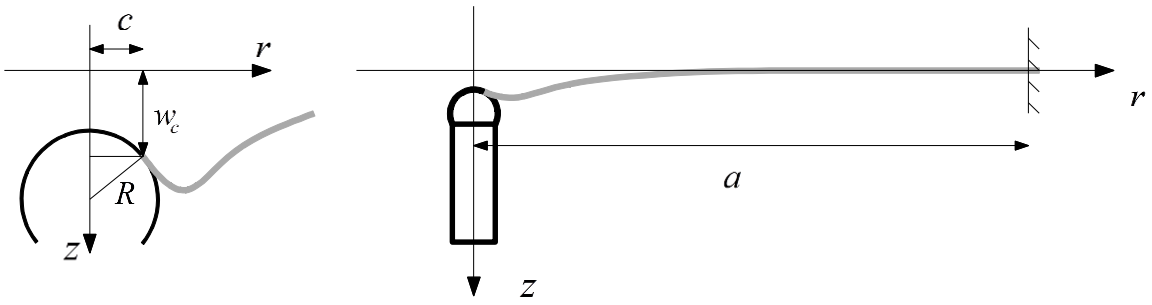

Figure 3.2 The axisymmetric von Karman thin plate theory is used to model the film outside contact (right). Geometric parameters at the contact line are defined on the left. Cylindrical coordinates (r, θ, z) are convenient for this problem. Here z is positive downwards and is the distance of a point from the mid-plane of the plate

Although the maximum deflection is on the order of several film thicknesses, the strains in the film were small, so a small strain constitutive model can be used to relate radial and hoop line forces N_r, N_θ to radial and hoop strains ε_r, ε_θ. Subscripts r and θ indicate components in radial and hoop directions respectively.

$$N_r = T_0 + \frac{Eh}{1-\nu^2}\left(\varepsilon_r + \nu\varepsilon_\theta\right) \qquad N_\theta = T_0 + \frac{Eh}{1-\nu^2}\left(\varepsilon_\theta + \nu\varepsilon_r\right) \tag{3.1}$$

where $\varepsilon_r = u' + \left(w'\right)^2/2 \qquad \varepsilon_t = u/r$ (3.2)

Here, u and w are displacements in r and z directions, h the initial thickness of the film, E the Young's modulus and ν the Poisson's ratio. Since PDMS is practically incompressible, we set ν = 1/2. In (3.2), the prime denotes differentiation with respect to r.

Equations of equilibrium are [30]

$$N_r - N_\theta + rN_r' = 0 \tag{3.3}$$

$$-D\left(\left(rw'\right)'/r\right)' + N_r w' = \frac{P}{2\pi r} \tag{3.4}$$

where $D = \frac{Eh^3}{12\left(1-\nu^2\right)}$ is flexural rigidity of the film and P the indentation force (positive downwards). Substituting the constitutive relations (3.1) and (3.2) into equilibrium equations (3.3) and (3.4), we obtain

$$\begin{aligned} u'' + \frac{u'}{r} - \frac{u}{r^2} &= -\frac{1-\nu}{2r}\left(w'\right)^2 - w'w'' \\ D\left(w''' + \frac{w''}{r} - \frac{w'}{r^2}\right) &= \left[T_0 + \frac{Eh}{1-\nu^2}\left(u' + \frac{\left(w'\right)^2}{2} + \frac{\nu u}{r}\right)\right]w' + \frac{P}{2\pi r} \end{aligned} \tag{3.5a, b}$$

The outer edge of the film at $r = a$ was bonded to the annular PDMS bulk support, and hence was modelled as a clamped edge with zero displacements and zero slope. The vertical displacement $w(c)$ and slope $w'(c)$ at the inner edge were determined by the contact radius c and the position of the indenter with respect to the clamped edge of the film. Hence, we solved (3.5a, b) subject to the following boundary conditions,

$$w(r=c)=w_c;\quad w'(r=c)=\sin^{-1}(c/R);\quad u(r=c)=u_c;$$
$$w(r=a)=w'(r=a)=u(r=a)=0 \tag{3.6}$$

where u_c and w_c are the displacements at the contact line in radial and vertical directions, respectively (see Fig. 3.2 left). Experimentally, we can measure the vertical position of the indenter with resolution of about 10nm while the contact radius can only be measured to an accuracy of ±5 μm. Hence the contact radius c is used as a fitting parameter along with T_0 and u_c when the numerical solution of $w(r)$ is fitted against the experimental deflection profile. Details of the numerical solution and fitting procedures are included in Appendix 3.1. Fig. 3.3(a) shows a typical fitted profile of the deflected thinnest film (~7.5 μm).

For each sample, we fit at least 5 experimental profiles at different indentation depth. Fig. 3.3(b) shows the deflected profiles of the thinnest film with corresponding values of T_0. The extracted value of T_0 is substantially independent of indentation depth, consistent with the supposition that T_0 is the constant pre-tension of the undeformed film.

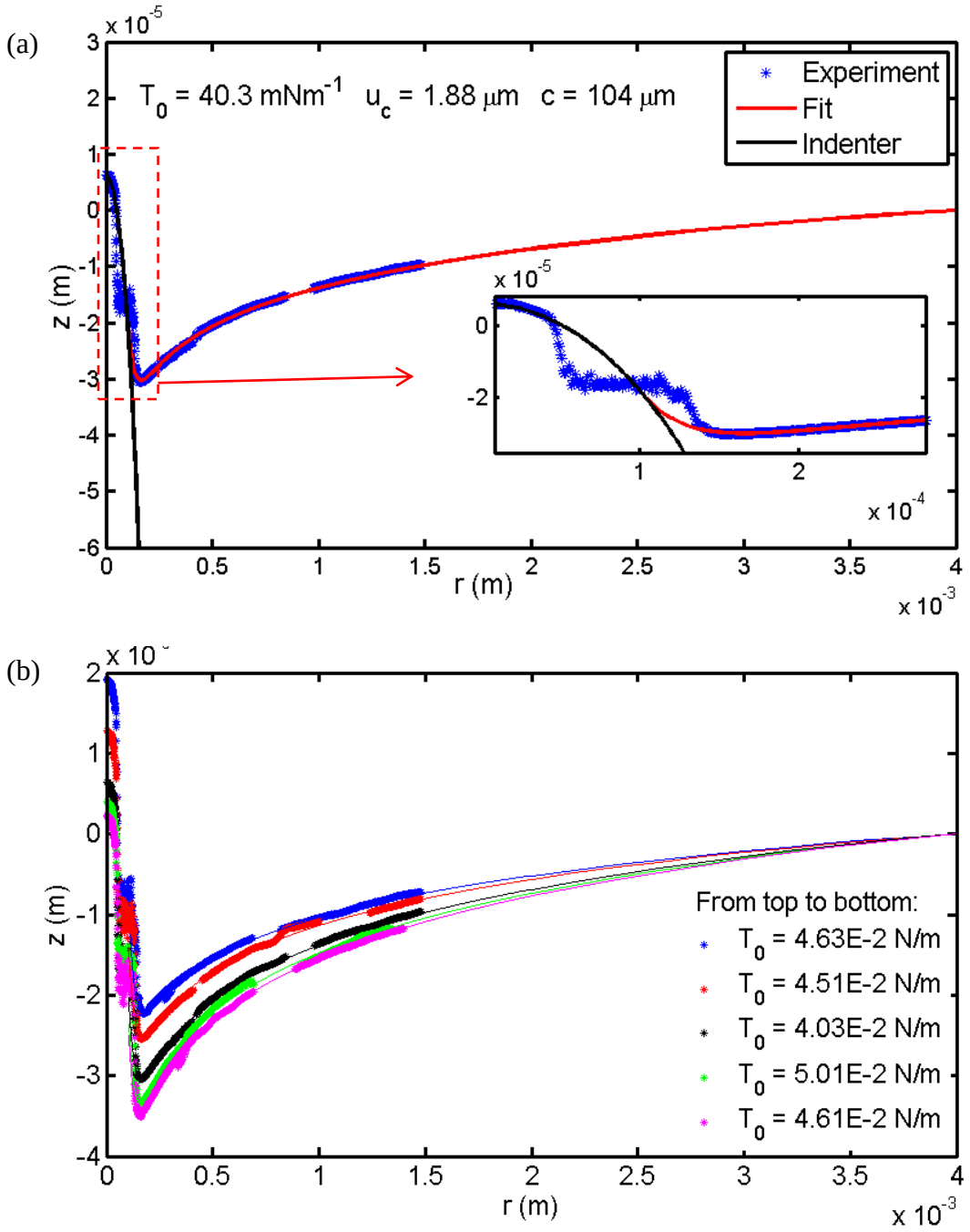

Figure 3.3 Fitting the deflections of the thinnest film (~7.5 μm thick) for different indentation depths. (a) Fitted profile in red for one value of deflection is plotted together with the experimental profile in blue and the indenter surface in black. (b) Fitted profiles for different deflections and the corresponding extracted values of T_0.

3.4 Results and Discussion

The tension T_0 arises due to (i) bulk residual stresses; (ii) surface tension of both the top and bottom surfaces of the film. The former, which we denote by $T_{residual}$ is most likely caused by the shrinkage [31] accompanying curing of PDMS liquid film (since thermal stresses were minimized by curing at room temperature), and can be expressed as

$$T_{residual} = Eh\varepsilon_{residual} / (1-\nu) \tag{3.7}$$

where the residual strain $\varepsilon_{residual}$ is expected to vary little among films of different thickness. Due to the clamped boundary condition, the surface tension contribution to T_0 is twice the solid-air surface tension of PDMS σ_{sv}, counting both the top and bottom surfaces of the film. Therefore,

$$T_0 = Eh\varepsilon_{residual} / (1-\nu) + 2\sigma_{sv} \tag{3.8}$$

To separate the bulk residual stress from the surface tension, we plot the fitted values of T_0 against Eh in Fig. 3.4. The linearly extrapolated value of tension at Eh = 0 is hence interpreted as the surface tension contribution that equals twice the solid-air surface tension of PDMS. The residual strain $\varepsilon_{residual}$ obtained by fitting is 0.21% as shown in Fig. 3.4, which is consistent with an independent study on shrinkage of PDMS (see Appendix 3.1). The value we obtained for surface tension of PDMS, with a 95% confidence interval, is 19.5±3.63 mN/m, which is comparable to its surface energy in the range of 15-24 mN/m [32-35]. Our result is also consistent with a recent work by Mondal *et al.* [27] using a different experimental method.

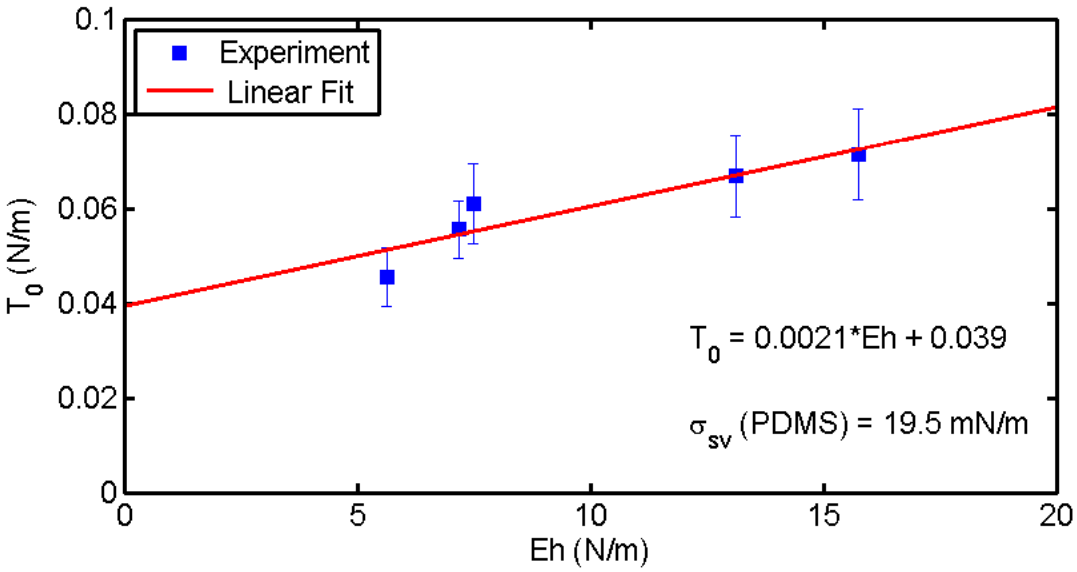

Figure 3.4 Extrapolation of film pre-tension to zero *Eh* value yields twice the surface tension of PDMS. The error bar represents 95% confidence intervals for each film sample.

In our previous attempt at measuring surface tension by suspending a liquid droplet under a PDMS film [13, 14], we estimated the total tensions in the film based on force balance but did not separate out the contribution due to elasticity. This, we supposed, would be handled automatically by linear extrapolation to zero thickness. We previously found surface tension for the PDMS film to be much higher than its surface energy. The source of the discrepancy lies in the assumption that both the residual tension and the tension due to stretching are directly proportional to *h*. Whereas this is true for the residual tension in equation (3.7), this assumption is incorrect for the tension due to stretching, which has a different dependence on *h.* The von-Karman plate model used in this work explicitly accounts for the pretension in the film and for its elasticity, and hence, we believe, yields a more robust and accurate estimate of the surface tension.

The deflections observed in the experiments are small in comparison with the film radii but are not small in comparison with the thicknesses. In the process of fitting the numerical solution to experimental data, we have found that fitted value of T_0 was quite sensitive to the profile close to the contact line, where bending is dominant. Neglecting bending near the contact line would result in a higher estimate of the tension. The von Karman plate model used in this work can capture both bending and stretching in the film provided that the deflection is limited to several times the film thickness. This offers an advantage to use thicker samples especially when the material has a low breaking stress. However there are no difficulties in using a pure bending plate model for deflections much smaller than the thickness or in using a membrane model for much larger deflections.

Our experimental method is limited by the ability to fabricate the sample which may be quite fragile, drying if the system has a liquid phase (such as a hydrogel) as well as the resolution of measurement system. The version of the method we have presented here works well with stable elastic polymeric films. With some further development it could be used to investigate predictions such as the theory proposed by Weijs *et al.* [36], which states that surface tension will be different from surface energy for compressible elastic materials. It could also be extended to study surface stresses coupled to more complex bulk behaviour such as viscoelasticity and poroelasticity, although this will additionally require extension of the theoretical model.

Despite these limitations, our method offers several advantages over the existing techniques [5, 6, 12, 13, 21, 23, 24, 26] in the literature. The compliant geometry of film samples makes it applicable to

relative stiff materials (E > 100kPa), of which the surface tension is difficult to measure using methods based on contact line deformation [5, 6, 12, 13]. Several studies [21, 23, 24, 26, 37] have captured the effect of surface tension using the bulge test technique [38-41] on stiff polymer or metal films. The inclusion of bending in our model permits the use of thicker samples and smaller deflections than these studies. Compared to the ultrathin samples used in these studies, the film samples in our experiments are three orders of magnitude thicker and larger. In this regard, sample handling is easier in this present method, and more importantly the deformation measurement has a higher level of accuracy. In addition, the key benefits of using a solid indenter (as opposed to a liquid droplet [13]) to deflect the film include more stable systems (i.e. less film fluctuation), better control of the deflection, longer measurement time and no transient contact line motion.

Acknowledgement

This work was supported by the U.S. Department of Energy, Office of Basic Energy Sciences, Division of Materials Sciences and Engineering under Award DE-FG02-07ER46463.

Appendix 3.1 Supplementary Information

Thickness measurement. After the sample was cut out and peeled from the glass slide, white light interferometer was used to locate the newly exposed glass surface and the free surface of remaining

film on the glass slide. Thickness measurements were taken at various points on one slide and mean thickness of each sample was calculated. The range of film thickness is 7-20 μm.

Young's Modulus measurement. Young's modulus of the PDMS was measured by an indentation test. A spherical glass indenter was brought into contact with thicker slabs (>5mm) of PDMS made from the same liquid PDMS mixture and undergoing the same curing cycle as the films. During one measurement, the indenter slowly indented into the sample with uniform speed and was then slowly lifted up until detaching from the sample. The contact area was captured by a microscope and the indenting force P was measured using a load cell. The Young's modulus E and work of adhesion W_{ad} can be obtained by fitting the experimental data using JKR theory [15],

$$\left(P-\frac{4E^{*}a^{3}}{3R}\right)^{2}=8\pi W_{ad}E^{*}a^{3},\ \text{where}\ \frac{1}{E^{*}}=\frac{1-\nu^{2}}{E}=\frac{3}{4E} \tag{A.3.1.1}$$

Solving von Karman plate equations. Normalize equations (3.5a, b) in this chapter using the following scheme,

$$w=w_{c}\bar{w},\ r=c\eta,u=\frac{w_{c}^{2}}{c}\bar{u},\ \ T_{0}=\frac{Ehw_{c}^{2}}{c^{2}}\bar{T}_{0},P=\frac{Ehw_{c}^{3}}{c^{2}}\bar{P} \tag{A.3.1.2}$$

Hence equations (3.5a, b) in this chapter become

$$\varepsilon \frac{d}{d\eta}\left[\frac{1}{\eta}\frac{d}{d\eta}\left(\eta\frac{d\bar{w}}{d\eta}\right)\right]=\left[\bar{T}_0+\frac{1}{1-\nu^2}\left(\frac{d\bar{u}}{d\eta}+\frac{1}{2}\left(\frac{d\bar{w}}{d\eta}\right)^2+\nu\frac{\bar{u}}{\eta}\right)\right]\frac{d\bar{w}}{d\eta}+\frac{\bar{P}}{2\pi\eta}$$

$$\frac{d^2\bar{u}}{d\eta^2}+\frac{1}{\eta}\frac{d\bar{u}}{d\eta}-\frac{\bar{u}}{\eta^2}=-\frac{1-\nu}{2\eta}\left(\frac{d\bar{w}}{d\eta}\right)^2-\frac{d\bar{w}}{d\eta}\frac{d^2\bar{w}}{d\eta^2} \qquad \text{(A.3.1.3a,b)}$$

where $\varepsilon=\frac{1}{12\left(1-\nu^2\right)}\left(\frac{h}{w_c}\right)^2$ (A.3.1.4)

From equation (A.3.1.4), the importance of bending depends on the square of the ratio of film thickness to imposed displacement at the inner edge.

Normalized boundary conditions are,

$$\bar{w}\left(\eta=1\right)=1,\bar{u}\left(\eta=1\right)=\frac{u_c c}{w_{c^2}}$$

$$\frac{d\bar{w}}{d\eta}\left(\eta=1\right)=\frac{c}{w_c}\sin^{-1}\left(c/R\right)\approx\frac{c^2}{Rw_c}\left(\text{small contact}\right) \qquad \text{(A.3.1.5)}$$

$$\bar{w}\left(\eta=a/c\right)=\frac{d\bar{w}}{d\eta}\left(\eta=a/c\right)=\bar{u}\left(\eta=a/c\right)=0$$

Equations (A.3.1.3a, b) need to be solved using an iterative numerical scheme for boundary value problems with MatLab®. The key idea is to increase w_c in small steps over a number of iterations. An analytical solution can be obtained, when a sufficiently small w_c is used, so that bending is dominant and nonlinear terms in equation (A.3.1.3a) can be neglected,

$$\varepsilon \frac{d}{d\eta}\left[\frac{1}{\eta}\frac{d}{d\eta}\left(\eta\frac{d\bar{w}}{d\eta}\right)\right]=\bar{T}_0\frac{d\bar{w}}{d\eta}+\frac{\bar{P}}{2\pi\eta} \qquad \text{(A.3.1.6)}$$

Subject to boundary conditions,

$$\begin{aligned}
&\bar{w}^0(\eta=1)=1\\
&\frac{d\bar{w}^0}{d\eta}(\eta=1)=\frac{c^2}{Rw_c^0}\\
&\bar{w}^0(\eta=a/c)=\frac{d\bar{w}^0}{d\eta}(\eta=a/c)=0
\end{aligned} \tag{A.3.1.7}$$

where a superscript ^{0} denotes the value used in the first iteration.

Let $\eta=\bar{r}\sqrt{\frac{\varepsilon}{\bar{T}_0}}$, the solution to equation (A.3.1.6) is,

$$\bar{w}^0(\bar{r})=\frac{-a_1K_0(\bar{r})+a_2\left(I_0(\bar{r})-1\right)}{\bar{T}_0}-\frac{\bar{P}}{\bar{T}_0}f(\bar{r})+\frac{A}{\bar{T}_0} \tag{A.3.1.8}$$

where

$$f(\bar{r})=\frac{G_{3,5}^{2,3}\left(\bar{r},\frac{1}{2}\middle|\begin{matrix}1/2,1,1\\1,1,0,0,0\end{matrix}\right)}{8\pi^{3/2}}+\frac{\sqrt{\pi}G_{5,7}^{2,3}\left(\bar{r},\frac{1}{2}\middle|\begin{matrix}\frac{1}{2},1,1,\frac{3}{4},\frac{5}{4}\\1,1,0,0,0,\frac{3}{4},\frac{5}{4}\end{matrix}\right)}{4}+\frac{\log(\bar{r})}{2\pi} \tag{A.3.1.9}$$

$$\begin{bmatrix}a_1\\a_2\\\bar{P}\\A\end{bmatrix}=\begin{bmatrix}K_1(\bar{r}_0) & I_1(\bar{r}_0) & -J(\bar{r}_0) & 0\\ K_1(\bar{r}_\infty) & I_1(\bar{r}_\infty) & -J(\bar{r}_\infty) & 0\\ -K_0(\bar{r}_0) & I_0(\bar{r}_0)-1 & -f(\bar{r}_0) & 1\\ -K_0(\bar{r}_\infty) & I_0(\bar{r}_\infty)-1 & -f(\bar{r}_\infty) & 1\end{bmatrix}^{-1}\begin{bmatrix}\frac{c^2\sqrt{\varepsilon\bar{T}_0}}{Rw_c^0}\\0\\\bar{T}_0\\0\end{bmatrix},\quad \bar{r}_0=\sqrt{\frac{\bar{T}_0}{\varepsilon}},\bar{r}_\infty=\frac{a}{c}\sqrt{\frac{\bar{T}_0}{\varepsilon}} \tag{A.3.1.10}$$

Solution to equation (A.3.1.3b) is

$$\bar{u}^0(\bar{r}) = \frac{1}{\bar{T}_0}\sqrt{\frac{1}{\varepsilon\bar{T}_0}}\left(b_1\bar{r} + b_2/\bar{r} - 2\bar{r}\int_{\bar{r}_0}^{\bar{r}} F(\bar{r}')d\bar{r}' + 2\bar{r}^{-1}\int_{\bar{r}_0}^{\bar{r}} (\bar{r}')^2 F(\bar{r}')d\bar{r}' \right) \tag{A.3.1.11}$$

where

$$\begin{aligned}
F(\bar{r}) &\equiv -\frac{1-\nu}{2\bar{r}}\left(\Phi(\bar{r})\right)^2 - \Phi(\bar{r})\frac{d\Phi(\bar{r})}{d\bar{r}} \\
\Phi(\bar{r}) &= a_1 K_1(\bar{r}) + a_2 I_1(\bar{r}) - \bar{P}\frac{K_1(\bar{r})I_0(\bar{r}) + I_1(\bar{r})K_0(\bar{r})}{2\pi} \\
b_1 &= \left[2\int_{\bar{r}_0}^{\bar{r}_\infty} F(\bar{r}')d\bar{r}' - \frac{2}{\bar{r}_\infty^2}\int_{\bar{r}_0}^{\bar{r}_\infty} (\bar{r}')^2 F(\bar{r}')d\bar{r}' - \frac{\bar{r}_0 c\bar{T}_0\sqrt{\varepsilon\bar{T}}u_c}{w_c{}^2\bar{r}_\infty^2} \right] \Big/ \left(1 - \frac{\bar{r}_0^2}{\bar{r}_\infty^2}\right) \\
b_2 &= -b_1\bar{r}_0^2 + \bar{r}_0\frac{c\bar{T}_0\sqrt{\varepsilon\bar{T}}}{w_c{}^2}u_c
\end{aligned} \tag{A.3.1.12}$$

In our iteration scheme, equations (A.3.1.8) and (A.3.1.11) were used as the initial guess to solve equations (A.3.1.3a, b) with the 'bvp4c' function in MatLab® in the first iteration. At the following iterations of increasing w_c, equations (A.3.1.3a, b) were solved numerically using the solution obtained from the previous iteration as the initial guess.

Fitting experimental profile. Fitting the numerical solution to experimental film profile was performed through a least square fitting scheme using $\{T_0, u_c, c\}$ as fitting parameters. While T_0 and u_c were free to vary, the contact radius c was constrained based on the approximated measurement in a range of ±5 μm. Fitting was performed on each film sample at 5-11 different indentation depths where deflections showed good axisymmetry.

Approximate measurement of residual strain in cured PDMS. A thin layer of PDMS (~200 μm) was moulded into a silicon master patterned with parallel microchannel structures of width 10 μm and centre-to-centre spacing 20 μm. After the PDMS layer was cured in the same manner as the film samples, it was peeled off from the silicon master. We then aligned and re-attached the PDMS layer to its silicon master. Misalignment induced by shrinkage was monitored using a microscope, and the residual strain was computed to be approximately (0.2 ± 0.001) %.

Appendix 3.2 Energy Release Rate of the Indented Circular Film

We consider the problem in this Chapter with geometry shown in Fig. A.3.2.1 below. Let us treat contact as an external ring crack and allow the crack grows along the surface of the sphere for a length *dl*. Then the external energy needed to bring back the initial configuration is calculated. Fig. A.3.2.1b shows a close-up at the crack tip, where solid line shows initial configuration, dashed line shows configuration after crack growth of *dl*. Note that Fig. A.3.2.1b is drawn locally, due to the non-zero bending rigidity, the film is always tangential to the surface of sphere at the contact line.

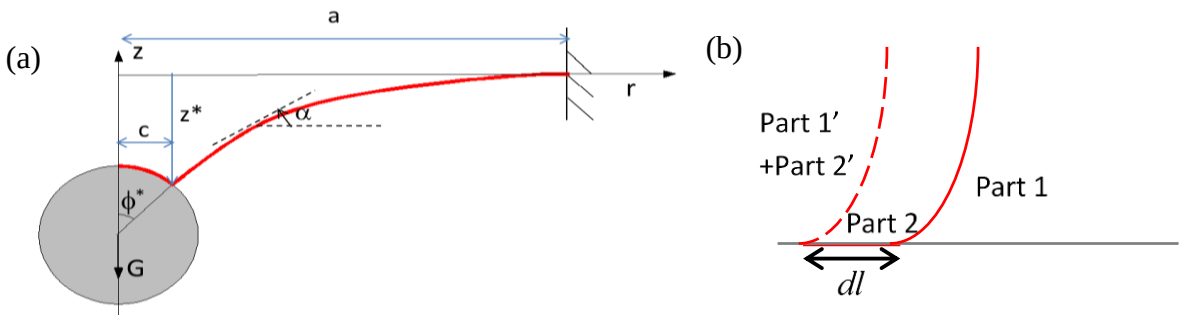

Figure A.3.2.1 Schematic figure of a pre-stretched thin elastic solid film deflected by a rigid indenter. (a), deformed configuration; (b) close-up of the ring crack tip formed between the film and the indenter.

At the end of $r = a$, displacement is prescribed. We assume $c << a$ such that the curvature goes to zero at far end. There is no work done at this end. At the end of $r = c$, the energy supplied include work done by shear force $Q(c)$, two bending moments $M_r(c)$, $M_t(c)$ and in-plane radial tension T_r all defined per unit length. The work done by the moments is

$$\delta U_1 - \delta W_1 = 2\pi c dl\left(-M_r(c)w"(c) - \mathrm{M}_t(c)w'(c)/c + T_r^+\left(\varepsilon_r^+ - \varepsilon_r^-\right)\right) \tag{A.3.2.1}$$

where ε_r^+ and ε_r^- are the two radial strains outside and inside contact line respectively. The work done by the shear force is neglected at this end because local slope is zero so that $\delta w \approx O\left(dl^2\right)$. Hoop stretch is continuous at the contact line, hence the contribution from hoop stretch is also zero.

The strain energy change from part 2'to part 2 is

$$\delta U_2 = 2\pi c dl\left(\frac{M_r(c)w"(c)}{2} + \frac{\mathrm{M}_t(c)w'(c)}{2c} + \frac{\left(T_r^-\varepsilon_r^- - T_r^+\varepsilon_r^+\right)}{2}\right) \tag{A.3.2.2}$$

The surface energy change due to the contact is (assuming rigid sphere surface)

$$\delta U_{ST} = -T_0 \delta A = -2\pi c T_0 dl \tag{A.3.2.3}$$

Therefore the total change in potential energy is

$$\begin{aligned} \delta\Pi &= \delta U_1 - \delta W_1 + \delta U_2 + \delta U_{ST} \\ &= 2\pi c dl \left\{ \frac{-M_r(c)w"(c)}{2} + \frac{-\mathrm{M}_t(c)w'(c)}{2c} + \frac{T_r^+\varepsilon_r^+ + T_r^-\varepsilon_r^- - 2T_r^+\varepsilon_r^-}{2} - T_0 \right\} \end{aligned} \tag{A.3.2.4}$$

The elemental area is $\delta A = -2\pi c dl$. Hence the energy release rate,

$$G = -\frac{\delta\Pi}{\delta A} = \left[\frac{-M_r(c)w"(c)}{2} + \frac{-\mathrm{M}_t(c)w'(c)}{2c} + \frac{T_r^+\varepsilon_r^+ + T_r^-\varepsilon_r^- - 2T_r^+\varepsilon_r^-}{2} - T_0 \right] \tag{A.3.2.5}$$

where under the assumption of small deflection,

$$M_r = -D\left(w"+\frac{\nu}{r}w' \right) \quad M_t = -D\left(\frac{1}{r}w'+\nu w" \right) \tag{A.3.2.6}$$

Since we are only look at the local picture in Fig. A.3.2.1b, slope at contact line is 0,

$$\begin{aligned} \varepsilon_r^+ &= u'\left(c^+\right) + \frac{\left[w'\left(c^+\right)\right]^2}{2} = u'\left(c^+\right) \\ \varepsilon_r^- &= u'\left(c^-\right) + \frac{\left[w'\left(c^-\right)\right]^2}{2} = u'\left(c^-\right) \end{aligned} \tag{A.3.2.7}$$

$$T_r^+ = \frac{Eh}{1-\nu^2}\left[u'\left(c^+\right)+\frac{\nu u(c)}{c}\right]+T_0$$
$$T_r^- = \frac{Eh}{1-\nu^2}\left[u'\left(c^-\right)+\frac{\nu u(c)}{c}\right]+T_0 \qquad \text{(A.3.2.8)}$$

where E is the Young's modulus, $D=\frac{Eh^3}{12\left(1-\nu^2\right)}$ is the bending stiffness.

Appendix 3.3 Deflection of a Pre-Tension Circular Film due to a Liquid Drop

Here we consider a liquid drop (blue) suspended under a thin circular plate (red) of radius L that is clamped at the far ends as shown in Fig. A.3.3.1.

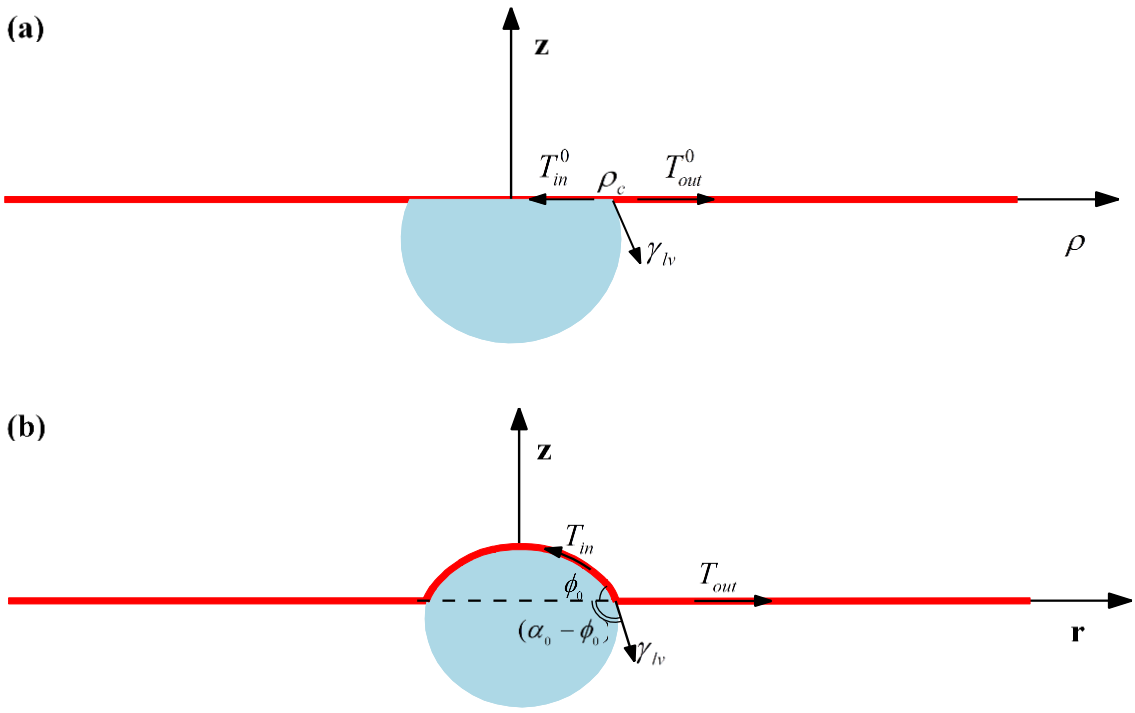

Figure A.3.3.1 Schematic figure of a liquid drop hanging underneath a pre-stretched thin elastic solid film. (a), referential configuration; (b) deformed configuration.

Membrane limit. Assume the thickness of the film *h* is so small that the mechanical behaviour of the plate approaches to 'membrane' limit. Upon deformation, the part of membrane in contact with the liquid drop (referred as the inner part) bulges upwards due to the pressure induced by liquid surface tension, and the other part of membrane (referred as the outer part) is stretched accordingly. A material point at (ρ, θ, 0) in the referential configuration (Fig. A.3.3.1a) displaces to (r, θ, z) in the deformed configuration (Fig. A.3.3.1b). Solid membrane, liquid drop and vapour are assumed to meet at a material line (i.e. the contact line) (ρ_c, θ, 0) in the referential configuration (Fig. A.3.3.1a) and (a, θ, 0) in the deformed configuration (Fig. A.3.3.1b). The contact line is assumed to be pinned to the material point in membrane. Angles formed by the membrane with lower liquid

drop surface and the horizontal axis at the contact line are θ_0 and ϕ_0 respectively as shown in Fig. A.3.3.1b. Furthermore, all surface tensions/energies are assumed to be uniform. Hence in the referential state, the pre-stretch due to surface energies in the membrane shown in Fig. A.3.3.1a are

$$T_0^{in} = \sigma_{sl} + \sigma_{sv} \qquad T_0^{out} = 2\sigma_{sv} \tag{A.3.3.1}$$

We first carry out force balance analysis on the whole configuration (Fig. A.3.3.2a), lower section of the liquid drop (Fig. A.3.3.2b), triple-phase contact point (Fig. A.3.3.2c) and the outer part of membrane (Fig. A3.3.2d). Fig. A.3.3.2a shows the vertical forces on the whole structure,

$$R_z = \frac{G}{2\pi L} \tag{A.3.3.2}$$

From Fig. A.3.3.2b,

$$P_c \pi a^2 + G_L = 2\pi a \sigma_{lv} \sin\left(\alpha_c - \phi_c\right) \tag{A.3.3.3}$$

where G_L is the weight of lower section of the liquid drop, P_c is the pressure at the level of triple-phase contact point. In Fig. A.3.3.2c, forces are balanced at the triple-phase contact point,

$$\begin{aligned} T_\xi^{in}\left(\rho_c\right)\sin\phi_c + T_s^{out}\left(\rho_c\right)\sin\omega_c &= \sigma_{lv}\sin\left(\alpha_c - \phi_c\right) \\ T_\xi^{in}\left(\rho_c\right)\cos\phi_c + \sigma_{lv}\cos\left(\alpha_c - \phi_c\right) &= T_s^{out}\left(\rho_c\right)\cos\omega_c \end{aligned} \tag{A.3.3.4a,b}$$

Finally in Fig. A.3.3.2d, force is balanced in vertical direction,

$$T_{\xi}^{in}(\rho_c)\sin\phi_c + R_z = \sigma_{lv}\sin(\alpha_c - \phi_c) \tag{A.3.3.5}$$

Hence if gravity is neglected in the case of small drop, R_z is zero, tension in the inner part balances liquid surface tension in the vertical direction, and angle ω is zero, i.e. the outer part is flat.

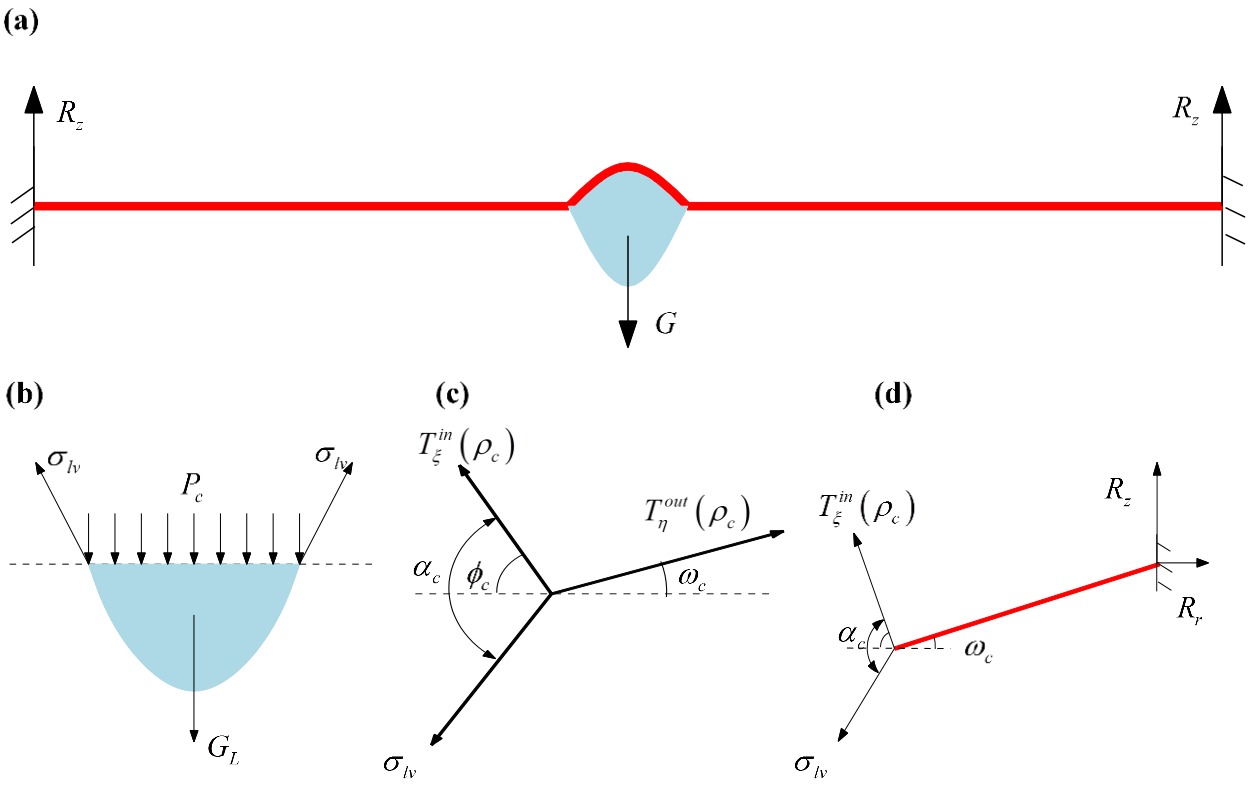

Figure A.3.3.2. Figures of force balance: (a) on the whole structure; (b) on the lower section of the drop; (c) at the contact line; (d) on the outer part of membrane.

From a mechanics point of view, we assume all the surface tensions/energies are known together with the volume (weight) of the liquid drop V (G) and initial radius and thickness of the membrane L and h_0. Deformed configuration is then determined from analytical calculation. Fig. A.3.3.1a shows schematically the referential undeformed configuration of the problem, in which, the

membrane is subjected to two different surface tensions on the inner and outer parts. The position of contact line ρ_c can be determined from the drop volume and its equilibrium contact angle α_c on the solid as defined by the fundamental Young's law

$$\cos\alpha_c = \frac{2\sigma_{sv} - (\sigma_{sl} + \sigma_{sv})}{\sigma_{lv}} \tag{A.3.3.6}$$

From the well-established pendant drop method, three ODEs are derived from hydro-mechanical equilibrium and geometry

$$\begin{cases} \dfrac{d\alpha}{ds} = \dfrac{2}{R_0} + \dfrac{\rho g z}{\sigma_{lv}} - \dfrac{\sin\alpha}{\rho} \\ \dfrac{d\rho}{ds} = \cos\alpha \\ \dfrac{dz}{ds} = \sin\alpha \end{cases} \tag{A.3.3.7}$$

where R_0 is radius of curvature at the apex and s is the arc length measured from the lowest point of the drop . The boundary conditions are

$$\begin{aligned} &\alpha(s=0) = 0 \quad z(s=0) = z_0 \quad \rho(s=0) = 0 \\ &z(s=s_c) = 0 \quad \alpha(s=s_c) = \alpha_c \end{aligned} \tag{A.3.3.8}$$

The unknowns are $\{\alpha, z, \rho, R_0, s_c, z_0\}$ and we need one more constrain on volume

$$\int_{z_0}^{0} \pi\rho^2 dz = V \tag{A.3.3.9}$$

Once solving equation (A.3.3.6), we can determine the location of contact line $\rho_c = \rho\left(s = s_c\right)$. Note that our assumption of pinned contact line implies that its location in undeformed configuration is fixed for a given drop.

In the case of small liquid drop, gravity is neglected. The shape of lower surface is a spherical cap. Then ρ_c can be approximated from geometry. For a spherical cap, volume and contact radius are related

$$V = \frac{\pi}{3}\left(\frac{\rho_c}{\sin\alpha_c}\right)^3\left(2+\cos\alpha_c\right)\left(1-\cos\alpha_c\right)^2 \Rightarrow \rho_c = \sin\alpha_c\left(\frac{3V}{\pi\left(2+\cos\alpha_c\right)\left(1-\cos\alpha_c\right)^3}\right)^{1/3} \quad \text{(A.3.3.10)}$$

Small strain limit. In small strain analysis, the material has elastic modulus *E* and Poisson's ratio *v*. Due to surface tension, total stress in the membrane relates to strains are

$$\begin{cases} \varepsilon_r = \frac{1}{E}\left(T_r - T_0\right) - \frac{\nu}{E}\left(T_\theta - T_0\right) \\ \varepsilon_\theta = \frac{1}{E}\left(T_\theta - T_0\right) - \frac{\nu}{E}\left(T_r - T_0\right) \end{cases} \Rightarrow \begin{cases} \varepsilon_r = \frac{1}{E}\left(T_r - \nu T_\theta\right) - \varepsilon_0 \\ \varepsilon_\theta = \frac{1}{E}\left(T_\theta - \nu T_r\right) - \varepsilon_0 \end{cases} \quad \text{(A.3.3.11)}$$

where $\varepsilon_0 = \frac{(1-\nu)}{E}T_0$. Consider the outer part, in small strain theory, the equilibrium equation for polar coordinates,

$$\frac{dT_r^{out}}{dr} + \frac{T_r^{out} - T_\theta^{out}}{r} = 0 \quad \text{(A.3.3.12)}$$

The strain-displacement relations are,

$$\varepsilon_r^{out} = \frac{du_r}{dr}, \varepsilon_\theta^{out} = \frac{u_r}{r} \tag{A.3.3.13}$$

$$\text{where} \quad \begin{aligned} T_r^{out} &= \frac{E}{1-\nu^2}\left[\left(\varepsilon_r^{out} + \varepsilon_0^{out}\right) + \nu\left(\varepsilon_\theta^{out} + \varepsilon_0^{out}\right)\right] \\ T_\theta^{out} &= \frac{E}{1-\nu^2}\left[\left(\varepsilon_\theta^{out} + \varepsilon_0^{out}\right) + \nu\left(\varepsilon_r^{out} + \varepsilon_0^{out}\right)\right] \end{aligned} \tag{A.3.3.14}$$

Substitute equation (A.3.3.13) and (A.3.3.14) into (A.3.3.12),

$$\frac{d^2u_r}{dr^2} + \frac{1}{r}\frac{du_r}{dr} - \frac{u_r}{r^2} = 0 \Rightarrow u_r = A_1 r + \frac{A_2}{r} \tag{A.3.3.15}$$

The membrane is clamped at far ends, assuming that the membrane is infinitely large, then $A_1 = 0$.

At the contact line, we have the second boundary condition

$$\begin{aligned} &a - \rho_c = u_r\left(\rho_c\right) = \frac{A_2}{\rho_c} \Rightarrow A_2 = \rho_c\left(a - \rho_c\right) \\ &\Rightarrow \varepsilon_r^{out} = \frac{\rho_c^2 - \rho_c a}{r^2}, \varepsilon_\theta^{out} = \frac{-\rho_c^2 + \rho_c a}{r^2} \end{aligned} \tag{A.3.3.16}$$

Substitute it back into equation (A.3.3.14),

$$\begin{aligned} T_r^{out}\left(\rho_c\right) &= \frac{E}{1+\nu}\left(1 - \frac{a}{\rho_c}\right) + T_0^{out} \\ T_\theta^{out}\left(\rho_c\right) &= \frac{-E}{1+\nu}\left(1 - \frac{a}{\rho_c}\right) + T_0^{out} \end{aligned} \tag{A.3.3.17}$$

Note that the T_r^{out} is tension along the membrane direction only in the case where gravity is neglected, when $\omega \neq 0$, tension along the membrane direction

$$T_s^{out}(\rho) = T_r^{out}(\rho) / \cos\omega(\rho) \tag{A.3.3.18}$$

When gravity is neglected, cos ω = 1

$$T_s^{out}(\rho_c) = T_r^{out}(\rho_c) = \frac{-E}{1+\nu}\left(1-\frac{\rho_c}{a}\right) + T_0^{out} \tag{A.3.3.19}$$

In addition, hoop stress

$$T_\theta^{out} = \frac{E}{1+\nu}\left(\frac{\rho_c}{r^2}(a-\rho_c)\right) + T_0^{out} \tag{A.3.3.20}$$

Hoop stress is always positive for sufficiently large *r*. However the hoop stress can be compressive unless $T_0^{out} > \frac{E}{1+\nu}\left(1-\frac{a}{\rho_c}\right)$. In this study, we assume T_0^{out} is large, so that no wrinkling can occur.

For the inner part, we assume that the slope angle at contact line ϕ_c is close to zero. Since the inner part has very small deformation, it is reasonable to assume the Laplace pressure applied to the inner membrane is uniform. If we assume no gravity, lower section of the liquid drop is part of a sphere. In addition, inner part of the membrane is approximated as a spherical cap of unknown radius R_m.

Under this assumption, pressure inside the drop is uniformed and the membrane is under biaxial tension T^{in}. From the force balance equation (A.3.3.3),

$$P_c = 2\sigma_{lv}\sin\left(\alpha_c - \phi_c\right)/a \tag{A.3.3.21}$$

By equilibrium, $P_c = 2T^{in}/R_m$.

From the geometry assumption of the membrane, $R_m = a/\sin\phi_c$. Therefore,

$$T^{in}\sin\left(\phi_c\right) = \sigma_{lv}\sin\left(\alpha_c - \phi_c\right) \tag{A.3.3.22}$$

Equation (A.3.3.22) is essentially the vertical force balance at the contact line in Fig.A.3.3.2c. In the radial direction, force balance from equation (A.3.3.4b) gives

$$T^{in}\cos\phi_c + \sigma_{lv}\cos\left(\alpha_c - \phi_c\right) = T_s^{out} \tag{A.3.3.23}$$

Volume should be constrained,

$$V = \frac{\pi a^3}{3}\left[\frac{\left(1-\cos\phi_c\right)^2}{\sin^3\phi_c}\left(2+\cos\phi_c\right) + \frac{\left(1-\cos\left(\alpha_c-\phi_c\right)\right)^2}{\sin^3\left(\alpha_c-\phi_c\right)}\left(2+\cos\left(\alpha_c-\phi_c\right)\right)\right] \tag{A.3.3.24}$$

Now we are trying to solve for the deformed configuration, i.e. $a, \phi_c, \left(\alpha_c - \phi_c\right)$. Substitute (A.3.3.22) and (A.3.3.20) into (A.3.3.23),

$$\frac{\sigma_{lv}\sin\left(\alpha_c-\phi_c\right)}{\tan\phi_c} + \sigma_{lv}\cos\left(\alpha_c-\phi_c\right) = \frac{E}{1+\nu}\left(1-\frac{a}{\rho_c}\right) + T_c^{out} \tag{A.3.3.25}$$

The next equation comes from matching in hoop strain $\varepsilon_\theta^{in} = \varepsilon_\theta^{out}$,

$$\frac{1-\nu}{E}\left(T^{in} - T_0^{in}\right) = \frac{a}{\rho_c} - 1 \Rightarrow \frac{1-\nu}{E}\left(\frac{\sigma_{lv}\sin\left(\alpha_c - \phi_c\right)}{\sin\phi_c} - T_0^{in}\right) = \frac{a}{\rho_c} - 1 \quad \text{(A.3.3.26)}$$

Note that in equation (30), (31) and (32), the only unknowns are $a, \phi_0, \left(\alpha_0 - \phi_0\right)$. An analytical solution can be obtained.

References

[1]. De Gennes, P. G., Brochard-Wyart, F., & Quéré, D. (2013). Capillarity and wetting phenomena: drops, bubbles, pearls, waves. Springer Science & Business Media.

[2]. Gibbs, J. W. (1906). The scientific papers of J. Willard Gibbs (Vol. 1). Longmans, Green and Company.

[3]. Roman, B., & Bico, J. (2010). Elasto-capillarity: deforming an elastic structure with a liquid droplet. Journal of Physics: Condensed Matter, 22(49), 493101.

[4]. Cammarata, R. C., & Sieradzki, K. (1994). Surface and interface stresses. Annual Review of Materials Science, 24(1), 215-234.

[5]. Paretkar, D., Xu, X., Hui, C. Y., & Jagota, A. (2014). Flattening of a patterned compliant solid by surface stress. Soft Matter, 10(23), 4084-4090.

[6]. Style, R. W., Boltyanskiy, R., Che, Y., Wettlaufer, J. S., Wilen, L. A., & Dufresne, E. R. (2013). Universal deformation of soft substrates near a contact line and the direct measurement of solid surface stresses. Physical review letters, 110(6), 066103.

[7]. Jerison, E. R., Xu, Y., Wilen, L. A., & Dufresne, E. R. (2011). Deformation of an elastic substrate by a three-phase contact line. Physical Review Letters, 106(18), 186103.

[8]. Marchand, A., Das, S., Snoeijer, J. H., & Andreotti, B. (2012). Contact angles on a soft solid: from Young's law to Neumann's law. Physical review letters, 109(23), 236101.

[9]. Hui, C. Y., & Jagota, A. (2014, July). Deformation near a liquid contact line on an elastic substrate. In Proc. R. Soc. A (Vol. 470, No. 2167, p. 20140085). The Royal Society.

[10]. Cao, Z., & Dobrynin, A. V. (2015). Polymeric Droplets on Soft Surfaces: From Neumann's Triangle to Young's Law. Macromolecules, 48(2), 443-451.

[11]. Mora, S., Phou, T., Fromental, J. M., Pismen, L. M., & Pomeau, Y. (2010). Capillarity driven instability of a soft solid. Physical review letters, 105(21), 214301.

[12]. Chakrabarti, A., & Chaudhury, M. K. (2013). Direct measurement of the surface tension of a soft elastic hydrogel: Exploration of elastocapillary instability in adhesion. Langmuir, 29(23), 6926-6935.

[13]. Nadermann, N., Hui, C. Y., & Jagota, A. (2013). Solid surface tension measured by a liquid drop under a solid film. Proceedings of the National Academy of Sciences, 110(26), 10541-10545.

[14]. Hui, C. Y., Jagota, A., Nadermann, N., & Xu, X. (2015). Deformation of a Solid Film with Surface Tension by a Liquid Drop. Procedia IUTAM, 12, 116-123.

[15]. Schulman, R. D., & Dalnoki-Veress, K. (2015). Liquid Droplets on a Highly Deformable Membrane. Physical Review Letters, 115(20), 206101.

[16]. Schroll, R. D., Adda-Bedia, M., Cerda, E., Huang, J., Menon, N., Russell, T. P., ... & Davidovitch, B. (2013). Capillary deformations of bendable films. Physical review letters, 111(1), 014301.

[17]. Chen, D., Cai, S., Suo, Z., & Hayward, R. C. (2012). Surface energy as a barrier to creasing of elastomer films: An elastic analogy to classical nucleation. Physical review letters, 109(3), 038001.

[18]. Mora, S., Abkarian, M., Tabuteau, H., & Pomeau, Y. (2011). Surface instability of soft solids under strain. Soft Matter, 7(22), 10612-10619.

[19]. Gurtin, M. E., & Murdoch, A. I. (1975). A continuum theory of elastic material surfaces. Archive for Rational Mechanics and Analysis, 57(4), 291-323.

[20]. Xu, X., Jagota, A., Peng, S., Luo, D., Wu, M., & Hui, C. Y. (2013). Gravity and surface tension effects on the shape change of soft materials. Langmuir, 29(27), 8665-8674.

[21]. Butt, H. J. (1996). A sensitive method to measure changes in the surface stress of solids. Journal of colloid and interface science, 180(1), 251-260.

[22]. Xu, S., O'Connell, P. A., & McKenna, G. B. (2010). Unusual elastic behavior of ultrathin polymer films: Confinement-induced/molecular stiffening and surface tension effects. The Journal of Chemical Physics, 132(18), 184902.

[23]. Zhai, M., & McKenna, G. B. (2014). Elastic modulus and surface tension of a polyurethane rubber in nanometer thick films. Polymer, 55(11), 2725-2733.

[24]. Mondal, S., Phukan, M., & Ghatak, A. (2015). Estimation of solid–liquid interfacial tension using curved surface of a soft solid. Proceedings of the National Academy of Sciences, 112(41), 12563-12568.

[25]. Cuenot, S., Frétigny, C., Demoustier-Champagne, S., & Nysten, B. (2003). Measurement of elastic modulus of nanotubes by resonant contact atomic force microscopy. Journal of applied physics, 93(9), 5650-5655.

[26]. Cuenot, S., Frétigny, C., Demoustier-Champagne, S., & Nysten, B. (2004). Surface tension effect on the mechanical properties of nanomaterials measured by atomic force microscopy. Physical Review B, 69(16), 165410.

[27]. Berger, R., Delamarche, E., Lang, H. P., Gerber, C., Gimzewski, J. K., Meyer, E., & Güntherodt, H. J. (1997). Surface stress in the self-assembly of alkanethiols on gold. Science, 276(5321), 2021-2024.

[28]. Maugis, D. (2013). Contact, adhesion and rupture of elastic solids (Vol. 130). Springer Science & Business Media.

[29]. Pethica, B. A., & Pethica, T. J. P. (1957). The contact angle equilibrium. In Second International Congress on Surface Activity (p. 131).

[30]. Timoshenko, S. P., & Woinowsky-Krieger, S. (1959). Theory of plates and shells. McGraw-hill.

[31]. Lee, S. W., & Lee, S. S. (2008). Shrinkage ratio of PDMS and its alignment method for the wafer level process. Microsystem Technologies, 14(2), 205-208.

[32]. Mullins, W. W. (1959). Flattening of a nearly plane solid surface due to capillarity. Journal of Applied Physics, 30(1), 77-83.

[33]. LeGrand, D. G., & Gaines, G. L. (1975). Immiscibility and interfacial tension between polymer liquids: dependence on molecular weight. Journal of Colloid and Interface science, 50(2), 272-279.

[34]. Owen, M.J. in *First International Congress on Adhesion Science and Technology*, edited by W.J. van Ooij and H.R. Anderson, Jr. (VSP, Utrecht, The Netherlands, 1998), p. 258.

[35]. Wu, S. in *Polymer Handbook*, 3rd Ed. by Brandrup, J. and Immergut, E.H. (Wiley-Interscience, New York, NY, 1989), p. VI: 414.

[36]. Weijs, J. H., Snoeijer, J. H., & Andreotti, B. (2014). Capillarity of soft amorphous solids: A microscopic model for surface stress. Physical Review E, 89(4), 042408.

[37]. Lu, T., Chen, C., Zhao, K., Zhang, W., & Wang, T. J. (2013). Bulge test at nano-scale: The surface effects. Applied Physics Letters, 103(5), 053110.

[38]. Vlassak, J. J., & Nix, W. D. (1992). A new bulge test technique for the determination of Young's modulus and Poisson's ratio of thin films. Journal of Materials Research, 7(12), 3242-3249.

[39]. Small, M. K., & Nix, W. D. (1992). Analysis of the accuracy of the bulge test in determining the mechanical properties of thin films. Journal of Materials Research, 7(06), 1553-1563.

[40]. Allen, M. G., Mehregany, M., Howe, R. T., & Senturia, S. D. (1987). Microfabricated structures for the insitu measurement of residual stress, young's modulus, and ultimate strain of thin films. Applied Physics Letters, 51(4), 241-243.

[41]. Mehregany, M., Howe, R. T., & Senturia, S. D. (1987). Novel microstructures for the insitu measurement of mechanical properties of thin films. Journal of Applied Physics, 62(9), 3579-3584.

CHAPTER 4

EFFECT OF SURFACE TENSION ON THE ADHESIVE CONTACT OF A RIGID SPHERE TO A COMPLIANT SUBSTRATE*

Abstract

In problems of indentation of an elastic half-space by a rigid sphere, the effect of surface tension outside the contact zone is not accounted by classical theories of contact mechanics. However surface tension plays a dominant role in determining the mechanics of this adhesive contact when the half-space becomes very compliant and the sphere is very small. Using a finite element method (FEM), we present a numerical solution of such a problem showing the transition between classical Johnson-Kendall-Roberts (JKR) deformation and liquid-like deformation in the absence of external load and gravity. The numerical model is in good agreement with experiments, [R.W. Style *et al.*, Nature communications 4 (2013)].

---

* Xu, X., Jagota, A. and Hui, C.Y., (2014). *Soft matter*, 10(26): 4625-4632.

4.1 Introduction

A canonical problem of central importance in the study of adhesion and contact mechanics is the mechanics of interaction between solid spheres [1]. Consider a rigid sphere of radius R brought into contact with an elastic half-space as shown in Fig. 4.1(a). (As is well-known in contact mechanics, the general problem of two smooth ellipsoidal surfaces can be mapped onto this problem by substituting for R an effective radius [1].) The sphere attains an equilibrium contact area A with the half-space even in the absence of external load due to the adhesion between the solid surfaces. The standard model for this process balances marginal adhesion energy that drives the increase of contact area, with marginal increase in strain energy that resists the increase of contact area. As long as the deformation is small, specifically, when the indentation depth δ and contact radius a are small in comparison with R, the solution is usually well described by the Johnson, Kendall and Roberts (JKR) [2] theory for soft materials. JKR theory predicts that the equilibrium contact radius a and indentation depth δ in the absence of external load are given by [1, 3]:

$$\frac{a}{R} = \left(\frac{6\pi W_{ad}}{KR} \right)^{1/3} \tag{4.1}$$

$$\frac{\delta}{R} = \left(\frac{2\pi W_{ad}}{\sqrt{3}KR} \right)^{2/3} \tag{4.2}$$

where W_{ad} is the work of adhesion, $K = \frac{4}{3}\frac{E}{1-\nu^2}$, E is the Young's modulus and ν is the Poisson ratio of the elastic half-space. For incompressible materials, $K = 16\mu/3$, where μ is the small strain shear modulus of the half-space. For $W_{ad} = 0$, the JKR theory reduces to Hertz theory [1].

Johnson (1998) [1] has pointed out that the adhesive forces between the solid surfaces become relatively more important with reduction in the product of contact size and elastic modulus. Muller *et al.* (1980) [4] presented a numerical calculation that indicated the JKR theory applies for soft solids, large radius of curvature and large energy of adhesion. For the sphere-plane geometry specifically, the JKR model is found to be valid in the domain of large sphere radius and a compliant half-space. In addition, even though JKR theory is based on small strain theory, a numerical study by Lin *et al.* [5] using large deformation elasticity theory has shown that the JKR model is accurate even for moderately large contact radius (half of the radius of the sphere). There are few studies that account for the effect of surface tension, although in simulations of the time-dependent growth of contacts, it has been shown that work of adhesion and surface tension can both play a role [6, 7].

It is therefore interesting to note that recently observed deformations of the soft substrates, such as plasticized polystyrene [8], hydrogels [9] and silicone gels [10] caused by adhesion of hard microparticles or nanoparticles deviate greatly from the JKR theory. For example, Chaudhury *et al.* [9] and Style *et al.* [10] have both reported that the exponent of power-law relationship in equations (3.1) and (3.2) between the contact radius (indentation depth) and the radius of sphere changes from 2/3 (or 1/3) to 1 as the sphere reduces in size or the substrates becomes softer. A similar result was also

obtained by Carrillo and Dobrynin [11] using molecular dynamics simulations. In these simulations, nanoparticles of different sizes are brought into contact with a rigid half-space and for soft small particles the reduction in their height is found to be proportional to their radii. It has been proposed that the departure from JKR scaling represents the increasing influence and contribution of solid surface stress in resisting deformation [10, 11]. Salez *et al.* (2013) [12] included surface tension in their analytical model of a similar problem where an spherical elastic particle is placed on a rigid substrate. Using a thermodynamic approach, they demonstrated a continuous change of the deformation mechanics from JKR adhesion to wetting with increasing contribution of surface tension. We therefore expect a transition in the contact mechanics of particles on an elastic foundation from a limit in which deformation is resisted principally by elasticity to a second limit in which resistance to deformation is provided mainly by surface tension.

JKR theory can be derived by minimizing the total potential energy of the system. In the absence of external loads, the theory considers two energy terms: the stored elastic energy U_E of the half-space and the surface energy of the interface, U_S. Specifically, the JKR model does not account for the role of surface tensions of the solid surfaces in resisting deformation. That is, the work done by the surface tensions upon change in surface area is neglected in the equation of energy balance. In addition, because surface tension changes the deformation field, the elastic energy itself is different from that given by JKR theory. For a very soft elastic half-space indented by small spheres, the contribution of surface tension to the energy balance becomes more significant, resulting in the breakdown of JKR theory. In the limit where the half-space is so soft that it behaves

like a liquid, neglecting gravity, the surface of the half-space outside the contact will remain flat and the sphere will move until the Young's equation is satisfied at the line of contact, where

$$\gamma_{sg} + \sigma \cos\theta = \gamma_{sa} \tag{4.3}$$

where γ's are the surface energies, the subscripts *s, g, a* stand for rigid sphere, compliant substrate (gel) and air respectively, σ is the surface tension on the exposed gel surface and θ is the contact angle as indicated in Fig. 4.1(b), which shows the deformed configuration in this limit. Equation (4.3) can be rewritten in a more revealing form:

$$\sigma\left(1+\cos\theta\right) = W_{ad}^{0} \tag{4.4}$$

The left hand side of equation (4.4) is the energy release rate due to a peeling of a thin membrane at (π - θ) degree [13, 14] and the right hand side is the work of adhesion of the sphere/solid interface, where the superscript zero denotes the particular case where the half-space has vanishing modulus. We have assumed that there is no sliding in the contact region, i.e., the surface tension of the region in contact is trapped in the same state as the region outside the contact.

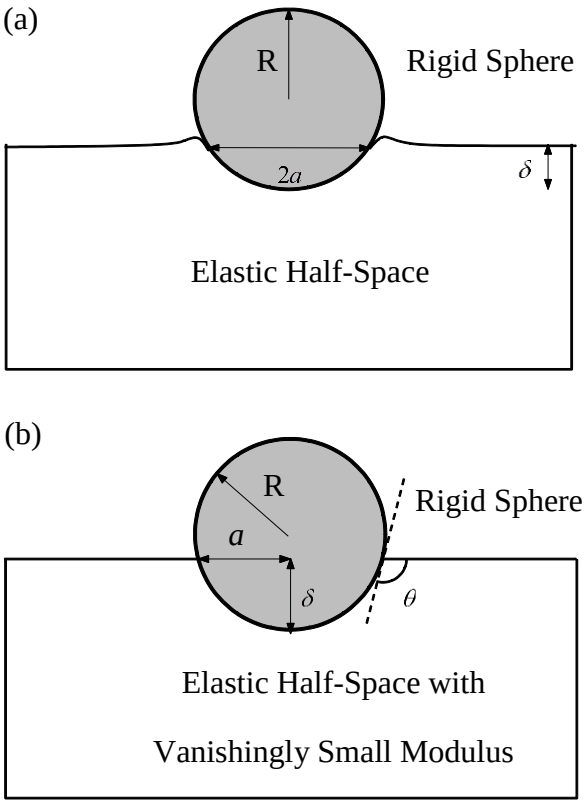

Figure 4.1 (a) A rigid sphere is brought into contact with an elastic half-space. A finite contact area is attained in the absence of external loads. (b) The deformed configuration when the modulus of the half-space is vanishingly small.

In this work we simulate contact between a rigid sphere and an elastic half-space from the elasticity-dominated to surface-tension-dominated limit using large deformation Finite Element Model (FEM) which incorporates surface tension in addition to elasticity. Specifically, we study the significant departure from JKR that occurs when the dimensionless parameter $\sigma/\mu R$ is large. In the surface-tension-dominated regime, elastic deformation is very large and the use of small strain theory is difficult to justify. This means that the nonlinear theory of elasticity, which accounts for

geometrical and material nonlinearity, is needed to determine the deformation. Consistent with Style *et al.* [10], we assume the surface tension is constant and isotropic. We show that our numerical results accurately capture recent experiments reported by Style *et al.* [10]. In addition, we compare our numerical result with an approximate analytical expression derived by Style *et al.* [10] and show that this expression is an excellent approximation to describe the new theory.

4.2 Dimensional Analysis and the Two Limits

In the following, we shall assume that the elastic half-space is incompressible, isotropic and homogeneous. For simplicity, the nonlinear elastic behaviour is given by the classical neo-Hookean model [15] with small strain shear modulus μ.

Dimensional analysis shows that the normalized indentation depth δ/R and contact radius a/R (see Fig. 4.1(a)) can be expressed as functions of two dimensionless parameters ($W_{ad}/\mu R$, W_{ad}/σ),

$$\frac{\delta}{R} = f_1\left(\frac{W_{ad}}{\mu R}, \frac{W_{ad}}{\sigma}\right) \tag{4.5}$$

$$\frac{a}{R} = f_2\left(\frac{W_{ad}}{\mu R}, \frac{W_{ad}}{\sigma}\right) \tag{4.6}$$

Note that the surface tension of the sphere does not enter in the analysis since the sphere is rigid.

In the elasticity-dominated regime, surface tension is negligibly small, $\sigma/\mu R \to 0$, and the deformation is completely determined by $W_{ad}/\mu R$. In this regime, for small contacts, equations (4.5) and (4.6) reduce to JKR theory given by (4.1) and (4.2).

In the other limit where the half-space becomes liquid-like, its shear modulus vanishes and $\sigma/\mu R \to \infty$. Using the geometric relation $\delta/R = \cos\theta + 1$ and equation (4.4), the condition of contact line equilibrium results in

$$\frac{\delta}{R} = \frac{W_{ad}}{\sigma} \tag{4.7}$$

$$\frac{a}{R} = \sqrt{1 - \left(\frac{W_{ad}}{\sigma} - 1\right)^2} \tag{4.8}$$

i.e. the deformation depends only on W_{ad}/σ. Thus, the behaviours of functions f_1 and f_2 in the surface-tension-dominated limit are completely determined. Notably, for equation (4.8) to apply, the work of adhesion cannot be more than twice of the surface tension. In this limit, both the contact radius and the indentation depth are directly proportional to the radius of the sphere, consistent with recent experimental findings [10].

In the intermediate regime, where both W_{ad}/σ and $W_{ad}/\mu R$ are important, f_1 and f_2 cannot be determined in closed form. To study the transition from JKR to the surface-tension-dominated limit, we carry out finite element analysis using ABAQUS®.

4.3 Finite Element Model

In our FEM model, the sphere is analytically rigid and the elastic half-space is modelled using axisymmetric quadratic elements with a neo-Hookean strain energy density function

$$W = \frac{\mu}{2}(I_1 - 3) \tag{4.9}$$

where $I_1 = \lambda_1^2 + \lambda_2^2 + \lambda_3^2$ is the first invariant of the left Cauchy-Green deformation tensor and the λ_i's are the principal stretch ratios. A set of user-defined axisymmetric surface tension elements [16] are attached to the half-space surface, transmitting surface tractions caused by the curvature of the deformed surface to the material.

We employ a similar loading scheme to the original JKR model in our FEM simulation. The system consisting of the rigid sphere and the elastic half-space is loaded in three steps (Fig. 4.2(a)): (1) surface tension is applied incrementally to the surface elements and stays at the final value σ in the following two steps. No deformation occurs in this step and it is performed first as a matter of convenience; (2) a vertical point force P is applied incrementally on the north pole of the rigid sphere, pushing it into the half-space, which results in a finite contact radius a; (3) the point force P is reduced to zero incrementally with the contact radius *a held fixed*, i.e. no separation of previously contacting regions is allowed in this step. The elastic energy is calculated as the net work done in the last two steps. The loading cycle is then repeated with different contact radii.

We assume no-slip boundary condition at the contact. The two surfaces in contact are not allowed to slide with respect to each other. Under this boundary condition, we only need to specify the surface tension on the substrate surface outside the contact. (Without no-slip boundary conditions we would need to introduce a new parameter into the model – the interfacial surface tension in the contacting region – and the surface-tension-dominated limit would be different.)

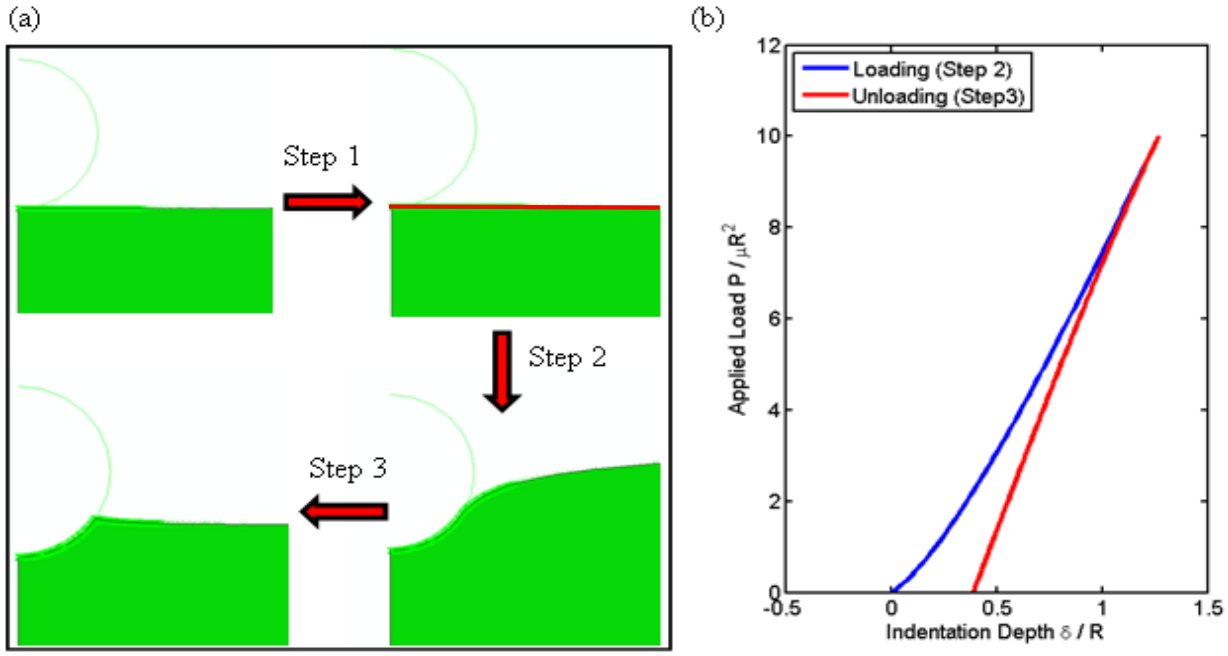

Figure 4.2 (a) Deformation of the half-space near the contact region after each loading step in a simulation with $\sigma / \mu R = 1$, $P / \mu R^2 = 10$. Only a trace of the axisymmetric system in the *r*-*z* plane is shown. The thin red layer on the surface after step 1 symbolizes non-zero surface stress. (b) The loading curve corresponding to steps 2 and 3. The elastic energy stored in the system is the area between the blue and red lines.

The last two steps allow us to calculate the energy release rate [17]. In step 2, the work done by the applied force on the half-space to make an indentation δ_P is $\int_0^{\delta_P} P_{load}(\delta')d\delta'$. Upon unloading, the total strain energy is

$$\Gamma = \int_0^{\delta_P} P_{load}(\delta')d\delta' + \int_{\delta_p}^{\delta} P_{unload}(\delta')d\delta' \tag{4.10}$$

where $P_{load}(\delta')$ and $P_{unload}(\delta')$ denote the loading and unloading curves (Fig. 4.2(b)) in step 2 and 3 respectively. The energy release rate G with respect to contact area is calculated by numerically evaluating

$$G = -\frac{\partial \Gamma}{\partial A} \tag{4.11}$$

using the central difference method. $A = 2\pi R\left(R - \sqrt{R^2 - a^2}\right)$ is the area in contact (for small deformation, $A \approx \pi a^2$). Since the surface tension is present throughout the loading and unloading steps, the surface and elastic energy induced by surface tension is accounted for in the computation of energy release rate. The equilibrium contact radius a and indentation depth δ is determined by the energy balance condition $W_{ad} = G$.

It is useful to consider the results as shown in equations (4.5) and (4.6), with a/R and δ/R as functions of ($W_{ad}/\mu R$, W_{ad}/σ), because in the elasticity-dominated limit the behaviour depends only on $W_{ad}/\mu R$ whereas in the surface-tension-dominated limit it depends only on W_{ad}/σ. However, in our numerical procedure, we control $\sigma/\mu R$ and a/R, each FE simulation yields a value for $W_{ad}/\mu R$.

These three numbers are then used to create triads of (a/R, $W_{ad}/\mu R$, W_{ad}/σ) and (δ/R, $W_{ad}/\mu R$, W_{ad}/σ), which create the two numerically-defined surfaces we desire.

4.4 Finite Element Results

A. Elasticity-Dominated and Surface-Tension-Dominated Limits

The FEM results at $\sigma/\mu R = 0$ (Fig. 4.3(a)) are in good agreement with the JKR model, except for large contacts where the small strain assumptions of JKR theory are no longer valid. Fig. 4.3(b) also shows that at $\sigma/\mu R = 50$, the FEM results are very close to the analytical solutions in surface-tension-dominated limit of equations (4.7) and (4.8).

(a)

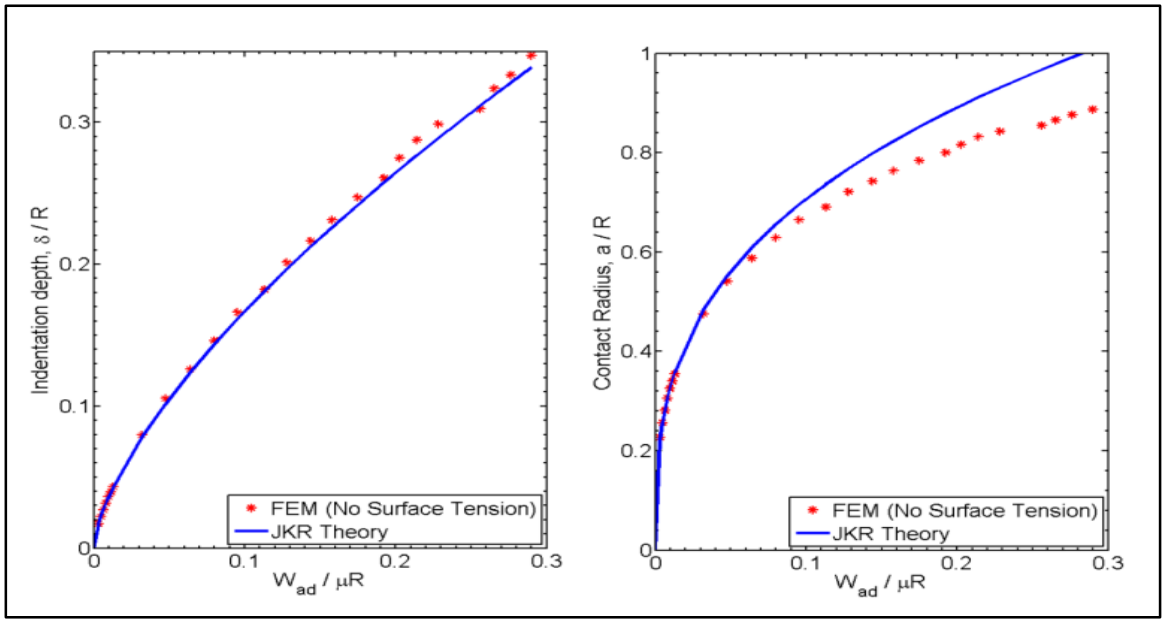

(b)

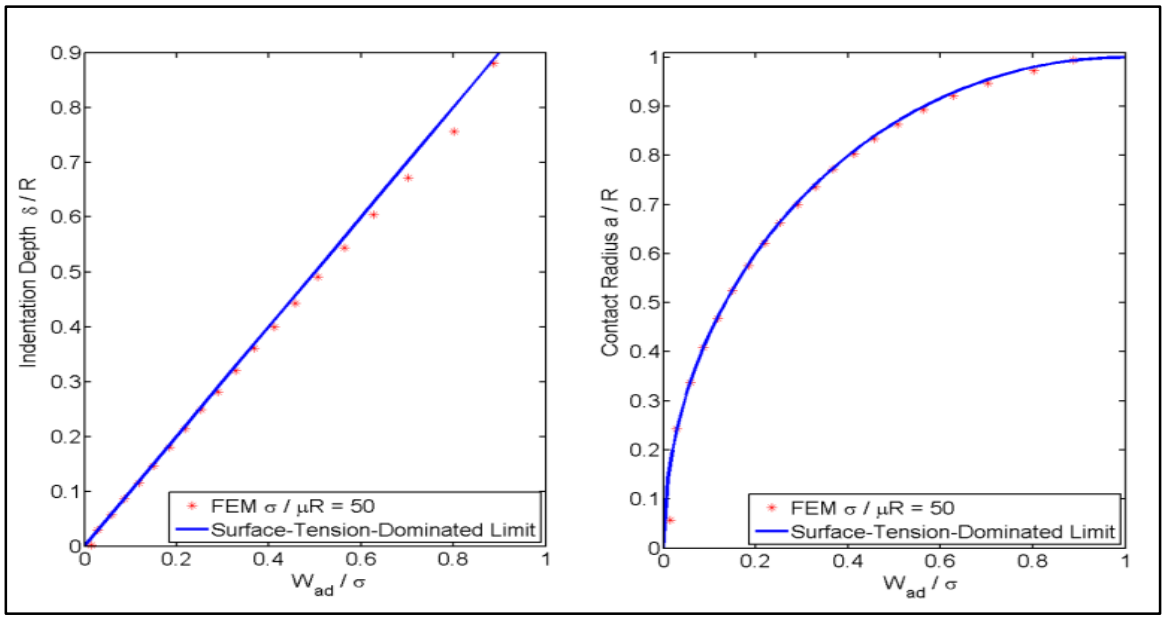

Figure 4.3 (a) $\sigma/\mu R = 0$. Plots of indentation depth (left) and contact radius (right) against the work of adhesion. (b) $\sigma/\mu R = 50$. Plots of indentation depth (left) and contact radius (right) against the ratio of work of adhesion to surface tension.

B. Transition from Elasticity-Dominated to Surface-Tension-Dominated Limit

The transition from the elasticity-dominated limit to surface-tension-dominated limit occurs with increasing $\sigma/\mu R$. Fig. 4.4(a) plots the transition by varying $\sigma/\mu R$ from 0 to 50 in the simulation at constant $W_{ad}/\sigma = 1$. In the elasticity-dominated limit, $\sigma/\mu R \rightarrow 0$, the FEM result approaches to the JKR theory in blue. As $\sigma/\mu R$ increases, δ/R increases asymptotically to the surface-tension-dominated limit in green.

The deformed surface profile near the contact line at different surface tension can be used to picture the transition. Fig. 4.4(b-d) shows the same sphere making contacts of same area with three half-spaces at increasing $\sigma/\mu R$. From left to right, the peak at the contact line gets smoothed out as $\sigma/\mu R$ increases. At $\sigma/\mu R = 50$, where surface tension dominates, the surface outside the contact becomes almost flat, and the half-space behaves like a liquid in the absence of gravity.

(a)

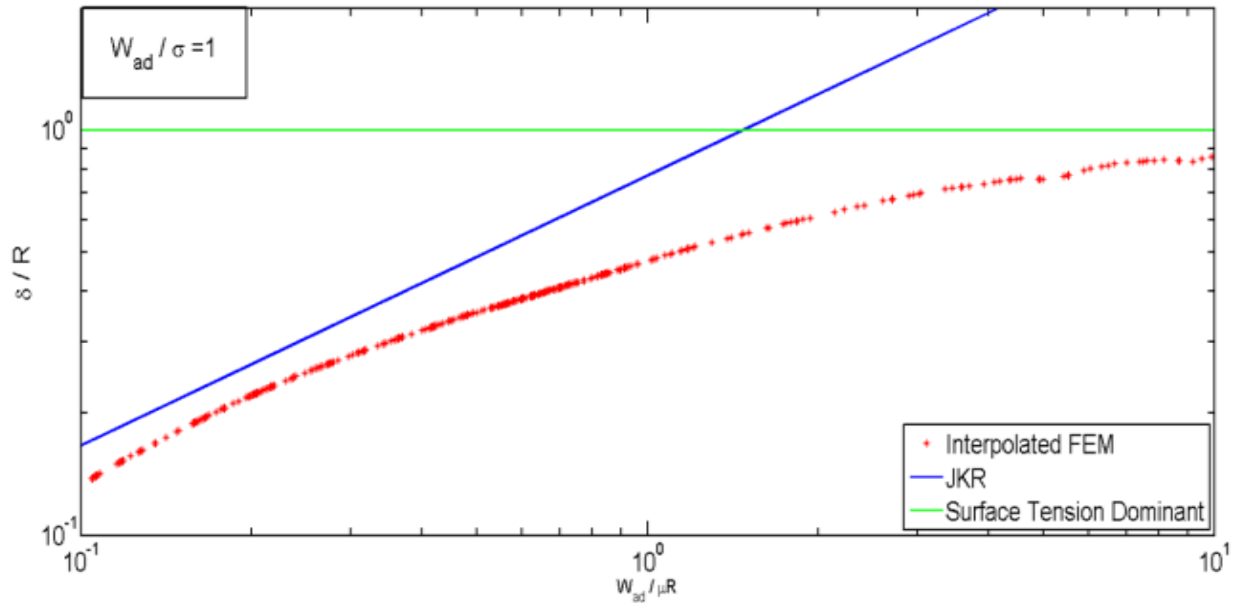

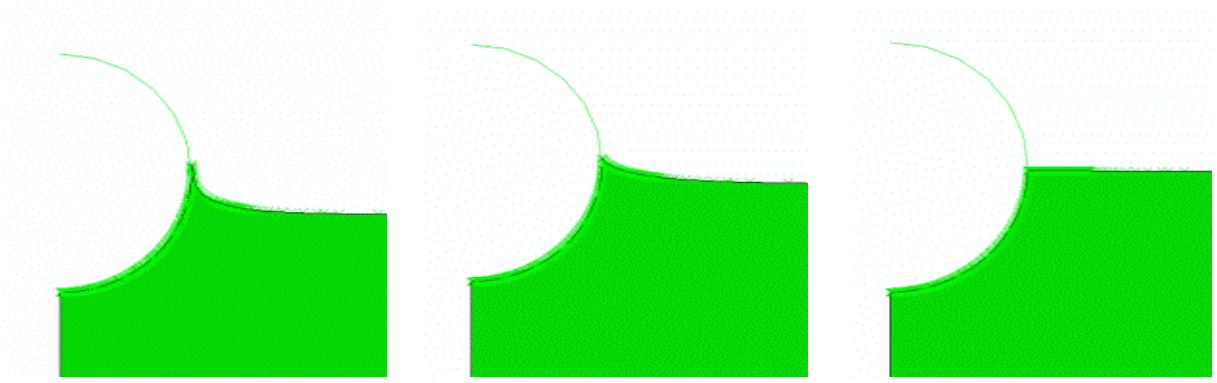

(b) $\sigma / \mu R = 0$ $W_{ad} / \mu R = 0.83$ (c) $\sigma / \mu R = 1$ $W_{ad} / \mu R = 1.93$ (d) $\sigma / \mu R = 50$ $W_{ad} / \mu R = 45$

Figure 4.4 (a) Indentation depth δ/R is plotted against $W_{ad}/\mu R$ at $W_{ad}/\sigma = 1$. (b) Deformed surface profiles in simulations of the same contact area at: $\sigma/\mu R = 0$; (c) $\sigma/\mu R = 1$; (d) $\sigma/\mu R = 50$.

C. Comparison with Experiments

Style *et al.* [10] recently studied contact between glass spheres and compliant silicone substrates with Young's moduli ranging from 3 to 500 kPa. They observed significant deviation of the substrate's deformation from the prediction of JKR theory for their softer gels. Because the glass spheres in their study are at the micron scale, gravity loading can be neglected. We fitted their experimental results using our FEM models and estimated the values of work of adhesion and surface tension for four silicone gels of known values of Young's moduli. Details of our fitting procedure are provided in Appendix 4. The fitted results are shown in Fig. 4.5.

For the stiffest substrate (green), where E = 500 kPa, $\sigma/\mu R$ is relatively small and the deformation is in the elasticity-dominated limit. The softest substrate (blue) deforms like a liquid as the plot of a versus R is almost linear. Our fitting estimates that the work of adhesion is 52-64 mN/m and surface tensions is 32-43 mN/m, both slightly lower than the values suggested by Style *et al.* [10] (the work of adhesion of 71 mN/m and surface tension of 45 mN/m). Note that there is a discrepancy between the experimental results and its numerical fit in the plot of δ against R for the softest gel (blue). The translation in log scale suggests that the numerical fit differs from the experimental results by a constant factor.

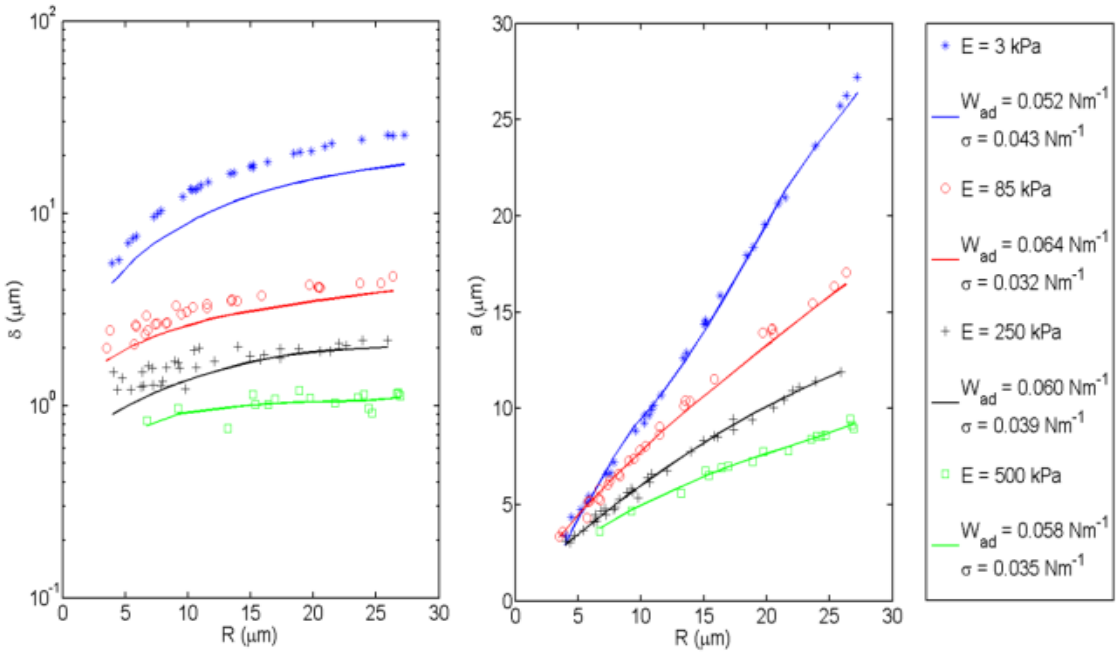

Figure 4.5 Experimental results (scattered points) of Style *et al.* [10] are fitted by interpolating the results of FEM simulations (solid lines). The corresponding fitted values of work of adhesion and surface tension are provided in the legends. Note that the blue line in the right figure should be linear by theory; the nonlinearity is due to the limitations of interpolation.

4.5 Approximate Formula for Deformation

Style *et al.* [10] proposed the following approximate relationship between the normalized indentation depth, work of adhesion and surface tension:

$$\frac{16}{\sqrt{3}}\left(\frac{\delta}{R}\right)^{3/2}+2\pi\frac{\sigma}{\mu R}\frac{\delta}{R}-2\pi\frac{W_{ad}}{\mu R}=0 \tag{4.12}$$

Equation (4.12) reproduces the JKR result at $\sigma/\mu R = 0$ and yields the result in surface tension-dominated limit as $\sigma/\mu R \to \infty$. In Fig. 4.6 (left) we verified equation (4.12) (solid lines) against our FEM results (stars). It shows that equation (4.12) is very accurate even at intermediate values of $\sigma/\mu R$.

We propose the following phenomenological interpolated relationship between the normalized indentation depth and contact radius,

$$\bar{a}^2 = 2\bar{\delta} - \bar{\delta}^2 + \frac{1}{2\pi\left(\sigma / \mu R\right) + 1/\left(\bar{\delta} + \bar{\delta}^2\right)} \tag{4.13}$$

where $\bar{a} = a / R$ and $\bar{\delta} = \delta / R$. Equation (4.13) reduces to the JKR theory as $\sigma/\mu R \to 0$, and it also gives the correct geometric relationship in the surface-tension-dominated limit as $\sigma/\mu R \to \infty$. Using equations (4.12) and (4.13), $\bar{a}$ is plotted against $W_{ad}/\mu R$ (solid lines) and compared to the FEM results (stars) in Fig. 4.6 (right). As mentioned earlier, the JKR theory breaks down when the contact radius is large (Fig. 4.3(a)). The discrepancy between the FEM results (stars) and this approximation (solid lines) of equations (4.12) and (4.13) is also relatively large at small values of $\sigma/\mu R$ when a/R is large. However, for the cases where surface tension is important, the proposed approximation gives very close estimates even at large scale contact.

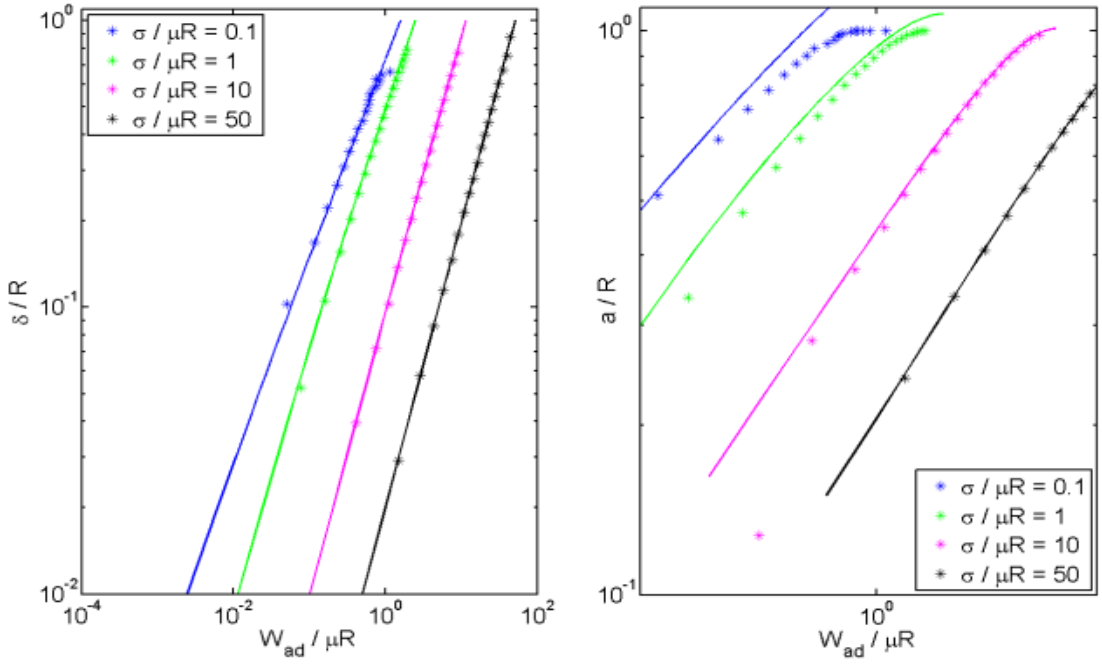

Figure 4.6 Normalized indentation depth (left) and contact radius (right) are plotted against normalized work of adhesion and it shows good agreements between FEM results (stars) and Equation (4.12-4.13) (solid lines).

4.6 Conclusion

For sufficiently compliant materials and small particles, surface tension can play a dominant role in determining the mechanics of adhesive contact between two surfaces. We present a numerical study of the transition between classical JKR deformation and surface-tension-dominated deformation of a compliant elastic half-space indented by a rigid sphere in the absence of external

load and gravity. Using a newly developed surface tension element, we are able to simulate very large contact, which is usually observed when very small spheres (micron scale) and very soft (less than 100kPa) substrates are brought into contact. The indentation depth and contact radius due to adhesive contact without applied external load are characterized completely by two dimensionless parameters ($W_{ad}/\mu R$, W_{ad}/σ).

There are two theories for deformable solid surfaces in adhesive contact, the JKR theory and the one presented by Derjaguin, Müller and Toporov [18] (the DMT theory). The validity of these two theories for specific cases can be examined by calculating the Tabor parameter $\mu_{Tabor} = \left(\frac{RW_{ad}^2}{E^{*2} z_0^3} \right)^{1/3}$, where $E^* = E/\left(1-\nu^2\right) = 4\mu$ is the effective elastic modulus and z_0 is the range of interactions between molecules. In the experiments of Style *et al.* [10], the value of Tabor parameter is in the order of (10^4) [21], and hence we replace explicit adhesive interaction with energy balance method as in the JKR theory. However, our FEM can be extended to include explicit adhesive interactions, e.g. to investigate contacts of spheres with stiffer substrates [6, 7]. We further note that the difference between DMT and JKR is relatively minor compared to the qualitative change when surface tension replaces elasticity as the dominant term resisting adhesive contact.

Although in the JKR analysis, there are no specified boundary conditions at the contact, we employ a no-slip boundary condition during the loading and unloading process in our FEM simulations. This is consistent with our analysis at the surface-tension-dominated limit analogous to Kendall's peel test. An extra parameter that would potentially affect the phenomenon, namely interfacial

tension, is also rendered irrelevant by this no-slip condition. In our FEM model, surface elements are applied on the entire surface of the half-space. However due to the no-slip boundary condition in the contact zone, surface traction applied to surface elements within the contact is balanced by the boundary constraint. Therefore surface tension is only applied effectively at the exposed surface of the half-space. No doubt that this no-slip boundary condition is not appropriate for all situations. However, it is also easy to incorporate frictionless boundary condition in our FEM model.

The largest deformation achieved in our FEM simulations is at $a/R = 1$. The deformation limit is imposed by the meshing of the FEM model. However larger deformations (i.e. passing the point of $a/R = 1$), can be achieved with some adaptive finite element re-meshing techniques.

We presume that in the experiments of Style *et al.* [10], the contact area increases monotonically and the work of adhesion is the work released upon contact growth. However, this remains an assumption as it is possible that in the process of depositing particles onto the substrate, contact area may decrease following an initial increase. In which case, the work of adhesion may not be a unique quantity and the effect of contact angle hysteresis becomes important [22].

Lastly, we neglect gravity in our study because the sphere is very small and the indentation is mainly a result of the action of adhesive forces between the two solid surfaces. In the surface-tension-dominated limit, because there is no external force, the net component of the surface tension for any sections outside the contact must not have a vertical component, and the surface is flat. However if the sphere is sufficiently large, gravity also plays a part in causing the deformation.

Especially in the surface-tension-dominated limit, the surface outside the contact is no longer flat, because gravity induces a gradient in pressure difference as one move away from the contact line. According to Young-Laplace equation, this will result in a changing surface curvature.

Acknowledgements

We thank Robert W. Style and Eric R. Dufresne for providing their experimental data and helpful discussions and comments. This work was supported by the U.S. Department of Energy, Office of Basic Energy Sciences, Division of Materials Sciences and Engineering under Award DE-FG02-07ER46463.

Appendix 4 Supplementary Information

From the FEM results, we generate surfaces of normalized indentation depth δ/R and contact radius a/R in terms of ($W_{ad}/\mu R$, W_{ad}/σ). A spline interpolation method using Green function approach [b] is employed to interpolate the scattered FEM results. Physically this corresponds to forcing a thin elastic plate to pass through the known data points with a shape that minimizes its strain energy.

[b] Sandwell, D.T., *Biharmonic spline interpolation of GEOS-3 and SEASAT altimeter data.* . Geophysical research letters, 1987. **14**(2): p. 139-142.

Note that in the attempt of extrapolating *a/R*, the result may be greater than 1, which is incorrect. Here we assume that the surface is symmetric about *a/R* = 1, so if the extrapolated value for $(a/R)_{extrapolated} > 1$, $(a/R) = 2-(a/R)_{extrapolated}$. Figure A.4.1 below shows the generated surface plotted with the FEM results in black dots.

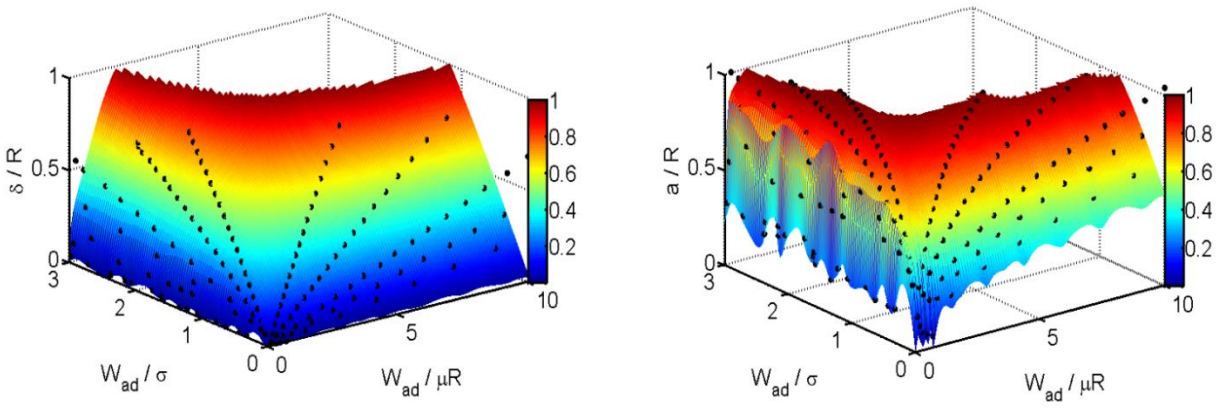

Figure A.4.1 The surfaces of indentation depth (left) and contact radius (right) are interpolated over a grid of ($W_{ad}/\mu R$, W_{ad}/σ). The colour maps indicate values of δ/R and a/R. The scattered black dots are results from FEM simulations.

When conducting least-square fit of the experimental results reported by Style *et al.* [c] using the surfaces interpolated from FEM results, we use ($W_{ad}/\mu R$, W_{ad}/σ) as the fitting parameters. The fitted results shown in Fig. 4.6a and 4.6b in the manuscript are obtained from two fitting methods. In Fig. 4.6a, ($W_{ad}/\mu R$, W_{ad}/σ) are chosen such that sum of squares of errors in both the contact radius and the indentation depth is minimized. We noticed that experimental measurements of the

[c] Style, R.W., Hyland, C., Boltyanskiy, R., Wettlaufer, J. S., & Dufresne, E. R., *Surface tension and contact with soft elastic solids.* arXiv preprint, 2013. **arXiv:1308**(1934).

contact radius were less scattered than those of the indentation depth. Hence in Fig. 4.6b, ($W_{ad}/\mu R$, W_{ad}/σ) used only minimizes the sum of squares of errors in the contact radius. We then plotted the resulting indentation depths to compare with the measurements in experiments.

The pair of ($W_{ad}/\mu R$, W_{ad}/σ) is not unique to result in a specific deformation. Hence some physical ground is required in attempts to interpreting experimental results correctly using the surfaces of deformation constructed by FEM simulations. For example if the contact scale is small and the material is relatively stiff, JKR theory should be used first to get a reasonable value of $W_{ad}/\mu R$. Then a fitting against the FEM results can be done in the proximity of that value to obtain more accurate values of ($W_{ad}/\mu R$, W_{ad}/σ). This approach is used in the fittings of the cases where Young's moduli are 500 kPa (green in Fig. 4.6) and 250 kPa (black in Fig. 4.6). Similarly if the material is so soft that it behaves like a liquid (the red and blue cases in Fig. 4.6), the equations of surface tension dominated limit should be used to obtain a rough estimate of W_{ad}/σ, before fitting the FEM results to experimental data.

References

[1]. Johnson, K. L. (1998). Mechanics of adhesion. Tribology International, 31(8), 413-418.

[2]. Johnson, K. L., Kendall, K., & Roberts, A. D. (1971, September). Surface energy and the contact of elastic solids. In Proceedings of the Royal Society of London A: Mathematical, Physical and Engineering Sciences (Vol. 324, No. 1558, pp. 301-313). The Royal Society.

[3]. Maugis, D. (2013). Contact, adhesion and rupture of elastic solids (Vol. 130). Springer Science & Business Media.

[4]. Muller, V. M., Yushchenko, V. S., & Derjaguin, B. V. (1980). On the influence of molecular forces on the deformation of an elastic sphere and its sticking to a rigid plane. Journal of Colloid and Interface Science, 77(1), 91-101.

[5]. Lin, Y. Y., & Chen, H. Y. (2006). Effect of large deformation and material nonlinearity on the JKR (Johnson–Kendall–Roberts) test of soft elastic materials. Journal of Polymer Science Part B: Polymer Physics, 44(19), 2912-2922.

[6]. Jagota, A., Argento, C., & Mazur, S. (1998). Growth of adhesive contacts for Maxwell viscoelastic spheres. Journal of applied physics, 83(1), 250-259.

[7]. Lin, Y. Y., Hui, C. Y., & Jagota, A. (2001). The role of viscoelastic adhesive contact in the sintering of polymeric particles. Journal of colloid and interface science, 237(2), 267-282.

[8]. Rimai, D. S., Quesnel, D. J., & Busnaina, A. A. (2000). The adhesion of dry particles in the nanometer to micrometer-size range. Colloids and surfaces A: Physicochemical and engineering aspects, 165(1), 3-10.

[9]. Chakrabarti, A., & Chaudhury, M. K. (2013). Direct measurement of the surface tension of a soft elastic hydrogel: Exploration of elastocapillary instability in adhesion. Langmuir, 29(23), 6926-6935.

[10]. Style, R. W., Hyland, C., Boltyanskiy, R., Wettlaufer, J. S., & Dufresne, E. R. (2013). Surface tension and contact with soft elastic solids. Nature communications, 4.

[11]. Carrillo, J. M. Y., & Dobrynin, A. V. (2012). Contact mechanics of nanoparticles. Langmuir, 28(29), 10881-10890.

[12]. Salez, T., Benzaquen, M., & Raphaël, É. (2013). From adhesion to wetting of a soft particle. Soft Matter, 9(45), 10699-10704.

[13]. Long, R., Shull, K. R., & Hui, C. Y. (2010). Large deformation adhesive contact mechanics of circular membranes with a flat rigid substrate. Journal of the Mechanics and Physics of Solids, 58(9), 1225-1242.

[14]. Kendall, K. (1975). Thin-film peeling-the elastic term. Journal of Physics D: Applied Physics, 8(13), 1449.

[15]. Treloar, L. R. G. (1948). Stresses and birefringence in rubber subjected to general homogeneous strain. Proceedings of the Physical Society, 60(2), 135.

[16]. Xu, X., Jagota, A., Peng, S., Luo, D., Wu, M., & Hui, C. Y. (2013). Gravity and surface tension effects on the shape change of soft materials. Langmuir, 29(27), 8665-8674.

[17]. Vajpayee, S., Hui, C. Y., & Jagota, A. (2008). Model-independent extraction of adhesion energy from indentation experiments. Langmuir, 24(17), 9401-9409.

[18]. Derjaguin, B. V., Muller, V. M., & Toporov, Y. P. (1975). Effect of contact deformations on the adhesion of particles. Journal of Colloid and interface science, 53(2), 314-326.

[19]. Tabor, D. (1977). Surface forces and surface interactions. Journal of colloid and interface science, 58(1), 2-13.

[20]. Sandwell, D. T. (1987). Biharmonic spline interpolation of GEOS‐3 and SEASAT altimeter data. Geophysical research letters, 14(2), 139-142.

[21]. Israelachvili, J. N. (2011). Intermolecular and surface forces: revised third edition. Academic press.

[22]. Pitois, O., & Chateau, X. (2002). Small particle at a fluid interface: Effect of contact angle hysteresis on force and work of detachment. Langmuir, 18(25), 9751-9756.

CHAPTER 5

EFFECTS OF SURFACE TENSION AND LARGE DEFORMATION ON CONTACT OF SOFT SOLIDS*

Abstract

We study the coupled effect of surface tension and large deformation on contact behaviour of solids for two geometries. One is a rigid sphere indenting on an elastic half space. The other is an elastic sphere contacting with rigid plates. We develop finite element models for these two geometries and simulate both non-adhesive and adhesive contacts in large deformation regime. Surface tension is included in our model through a set of user-defined surface elements on the free surface of the elastic body. We also explore the difference between frictionless and no slip contacts. Our results of no slip contact are used to assess the applicability of the small strain theory proposed by Hui et al. (2015), which extends the classic Hertz and JKR theory to include surface tension.

---

* Xu, X., Liu, T., Jagota, A. and Hui, C.Y., (2016) submitted to *JMPS*.

5.1 Introduction

Understanding the mechanics of contact between non-conforming solid surfaces is of great importance in many circumstances [1, 2]. Examples include recent studies on colloidal dispersion [3], latex particles [4], biological cells [5] and micro-patterned substrates [6]. Also, microscopic indentation method [7] and atomic force microscopy (AFM) are frequently used to characterize the mechanical behaviour of biological materials. For example, the moduli of biological gels are often determined by measuring the amount of indentation due to the weight of a rigid sphere placed on the surface of substrate. To determine elastic modulus from these measurements, the biologists often used classical Hertz theory, which describes the small contact behaviour of solids in the absence of surface interactions (i.e. without considering adhesion and surface tension). Even though Hertz theory has been successful in deriving Young's modulus of many soft materials when adhesion is not significant [7, 9-11], its application to model soft contacts is still limited by its disregard of substrate surface stress and material nonlinearity.

In problems where adhesion forces are important, the standard theory is given by Johnson, Kendall and Roberts (JKR) [12]. The JKR theory treats the air gap between the sphere and the substrate as an external crack, and accounts for adhesion by computing the energy release rate G of this crack. The amount of contact is determined using Griffith's criterion of energy balance, that is $G = W_{ad}$, where W_{ad} is the effective work of adhesion. For ideal surfaces without hysteresis and governed by dispersive interaction, W_{ad} can be considered as the Dupré's work of adhesion. Although the JKR theory was successful at its inception, contact behaviours that deviated from the theory have

been reported in many recent experimental and theoretical studies on soft materials at small scales [13-15].

To understand the discrepancies between experimental results and Hertz or JKR predictions, it is necessary to highlight the major assumptions in these two theories. Both theories are based on small strain linear elasticity theory and hence are restricted to small contacts where the ratio of contact radius a to sphere radius R is much less than 1. As a result, the deformation of solid surfaces can be calculated as if they were half spaces. Also, because of small deformation, a linear constitutive relation between strain and stress is used. However, the small strain assumption breaks down for many problems of practical interest. For instance, many biological or polymeric materials typically have moduli on the order of kPa, so even relatively weak forces can cause very large shape change and hence these materials no longer obey a linear stress-strain relation. Furthermore, a clear distinction between the undeformed and deformed configurations has to be made in a large deformation setting. Lin and Chen (2006) [16] have studied the effect of material and geometry nonlinearities in the absence of surface tension on both the Hertz and JKR theories using finite element models (FEM). To be consistent with the theories, their finite element model assumed a frictionless contact condition.

Another assumption that is often challenged in recent studies [13, 17-23] is the neglect of surface stress outside the contact. Physically, one expects that surface stress resists indentation. Hence the amount of indentation will be less for a given external load, if surface stress is accounted for. The effect of surface stress is often characterized by the elasto-capillary number $\alpha = \sigma / \mu R$, where σ is

a measure of the surface stress and μ is the shear modulus of the elastic body. It has been noted that in the limit of infinitely large elasto-capillary number $\alpha \to \infty$, the mechanics of contact should be similar to wetting, which is governed by Young's equation [13]. By including the contribution of surface tension σ outside the contact in their finite element models, Xu *et al.* [18] successfully captured the transition from JKR adhesion to wetting for the contact between a rigid sphere and an elastic half space in the absence of external or gravitational load. Cao *et al.* [19] also reported the crossover between adhesion and wetting using molecular dynamics simulations for the same contact configuration. The case of spherical contact under finite external load has also been studied by Hui *et al.* [21], who proposed analytical modifications of Hertz and JKR theories to incorporate effect of surface tension outside the contact. Similar results are also obtained by a more recent work by Long *et al.* [23]. The problem of an elastic sphere placed on a rigid substrate was considered by Carriloo & Dobrynin [22] using molecular dynamics and Salez *et al.* [20] using an approximate energy approach. Notably, both the theoretical framework proposed by Salez *et al.* [20] and Hui *et al.* [21] are based on the linear elasticity theory, in which the difference between current and undeformed states is infinitesimally small. However the effect of surface tension is intrinsically non-linear, because the Laplace pressure is induced by deformation in the current state. This additional source of nonlinearity also adds uncertainties to the contact behaviour of soft solids in large deformation regime.

There is little discussion in the literature on the contact condition, particularly on the role of interfacial shear stresses. In the original small strain Hertz and JKR theories as well as Lin and Chen's [16] finite element studies, contacts are assumed to be frictionless. In Hui *et al.*'s [21] small

strain theory (SST), a no-slip contact condition is prescribed. Under the small strain assumption, the no-slip condition also gives zero shear interfacial stress when one of the contacting bodies is rigid and the other an incompressible elastic *half space* [24]. Hence both frictionless and no-slip conditions give the same results. However this need not be the case for large deformation. To further complicate matters, when contact is frictionless one needs to specify the portion of the interfacial surface stress that acts on the elastic body, which is difficult to do since the rigid body can in principal support any stress.

The objectives of this paper are therefore three-fold. First, to assess the coupled effect of nonlinearities (arising from geometry, material and surface tension) in non-adhesive and adhesive contacts. Second, to assess the applicability of the small strain theory proposed by Hui *et al.* [21] in the large deformation regime. Finally, the third objective is to study the difference between frictionless and no-slip contact conditions when the contact is large. Specifically, we use finite element method to study two contact systems: (1) a rigid sphere with an elastic half space and (2) an elastic sphere with a rigid substrate. In both systems, we explore the effect of surface tension by varying the elasto-capillary number α.

5.2.1 Finite Element Model

There are two contact geometries studied in the literature, a rigid sphere indenting on an elastic half space and an elastic sphere contacting with a rigid substrate. Modelling the former is straight forward as shown in Fig. 5.1a. However applying external load to the latter geometry requires

more careful consideration because of large deformation. Here we choose a symmetric loading system as shown in Fig. 5.1b, where equal and opposite vertical loads are applied to two rigid plates compressing the elastic sphere. This loading set-up is also easy to implement in experiments. To compare results with Lin and Chen [16], the elastic parts (half space in Fig. 5.1a and sphere in Fig. 5.1b) are modelled as incompressible neo-Hookean materials. The strain energy density W of these materials are

$$W = \frac{\mu}{2}(I_1 - 3) \tag{5.1}$$

where I_1 is the trace of Cauchy-Green strain tensor.

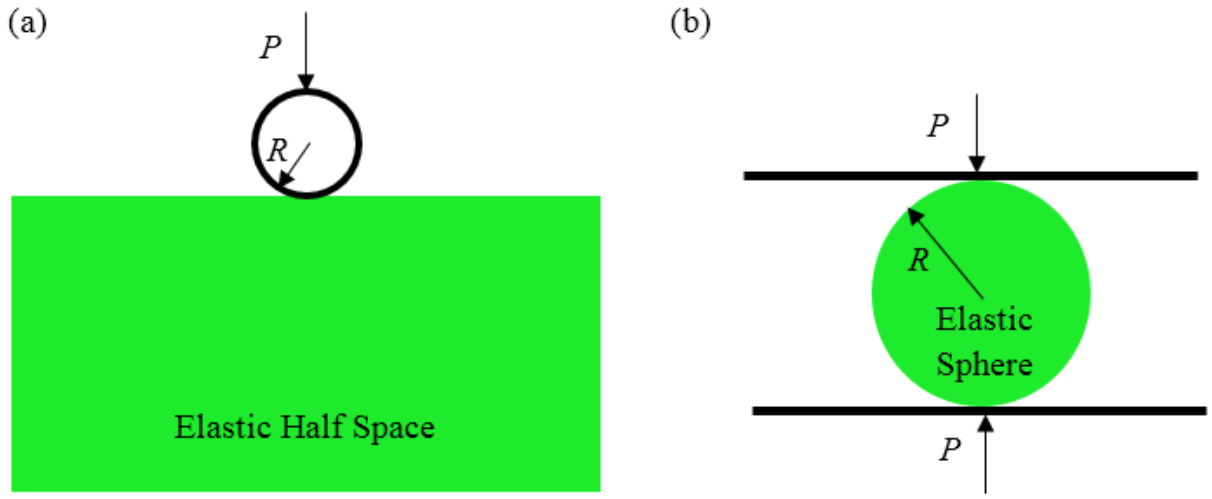

Figure 5.1. Geometries of finite element models: (a) a rigid sphere (solid black line) is brought into contact with an elastic half space; (b) an elastic sphere is sandwiched in between two rigid plates (solid black lines).

Surface tension is introduced to the system by augmenting the finite element model with a set of user-defined axisymmetric 2-node linear surface elements [18], which discretize the free surfaces of

the elastic bodies. These user defined surface elements transmit surface tractions caused by the curvature of the deformed surface to the bulk. In this study, we assume the solid-air surface stress is an isotropic tensor, with magnitude being the surface tension σ. Although not necessary [25], we assume σ is a material constant independent of surface deformation since so far all the contact analyses [13, 17-23] have employed this assumption.

We consider both frictionless and no-slip contacts. As far as computation is concerned, the contact problem is much easier to solve if no-slip condition is adopt. Indeed, even though the surface of elastic body could have different surface stresses before and after contact, these stress does not affect the solution because the continuity of displacement and no-slip condition fully determine the elastic solution. The frictionless contact condition however imposes difficulties in modelling. Prescribing a solid-solid interfacial stress generally assumes perfect bounding between the two surfaces. This is in contrary to frictionless condition, which allows the surfaces to slip. Furthermore, it is difficult to determine the portion of surface stress acting on the elastic surface when it is in contact with a rigid surface, because the rigid surface can in theory support any stress. In our simulations, we assume a constant surface stress σ for all surface elements inside and outside the contact.

To simulate contact, we employed similar loading schemes with adjustments to different geometries and interfacial conditions. All simulations are performed in steps: (step 1) surface tension is applied incrementally to the surface elements and held at the final value σ in the subsequent steps. Since the elastic body is a half space in Fig. 5.1a and an incompressible sphere

in Fig. 5.1b, no deformation occurs in this step for both geometries and it is performed first as a matter of convenience; (step 2) the vertical load is applied to the system incrementally to a final value of P_H, bringing the rigid and elastic parts closer and a finite contact radius a_H is achieved at the end of this step. Here we use a subscript H to indicate that the contact made during this loading step is non-adhesive; (step 3 *only for adhesive contacts*) the vertical load is *reduced* incrementally to a final value of P (negative value of P indicates a pulling force) while no separation from the rigid surface of previously contacting nodes is allowed. The contact radius at the end of the unloading step is a. Fig. 5.2 shows typical deformations of each geometry at the end of each step. Notice for no-slip contact, the two surfaces in contact are not allowed to slide with respect to each other; as a result, the contact radius remains unchanged during unloading step, i.e. $a = a_H$. However if frictionless boundary condition is applied, the contacting nodes can slide freely along the rigid surface (but not separate), hence $a < a_H$.

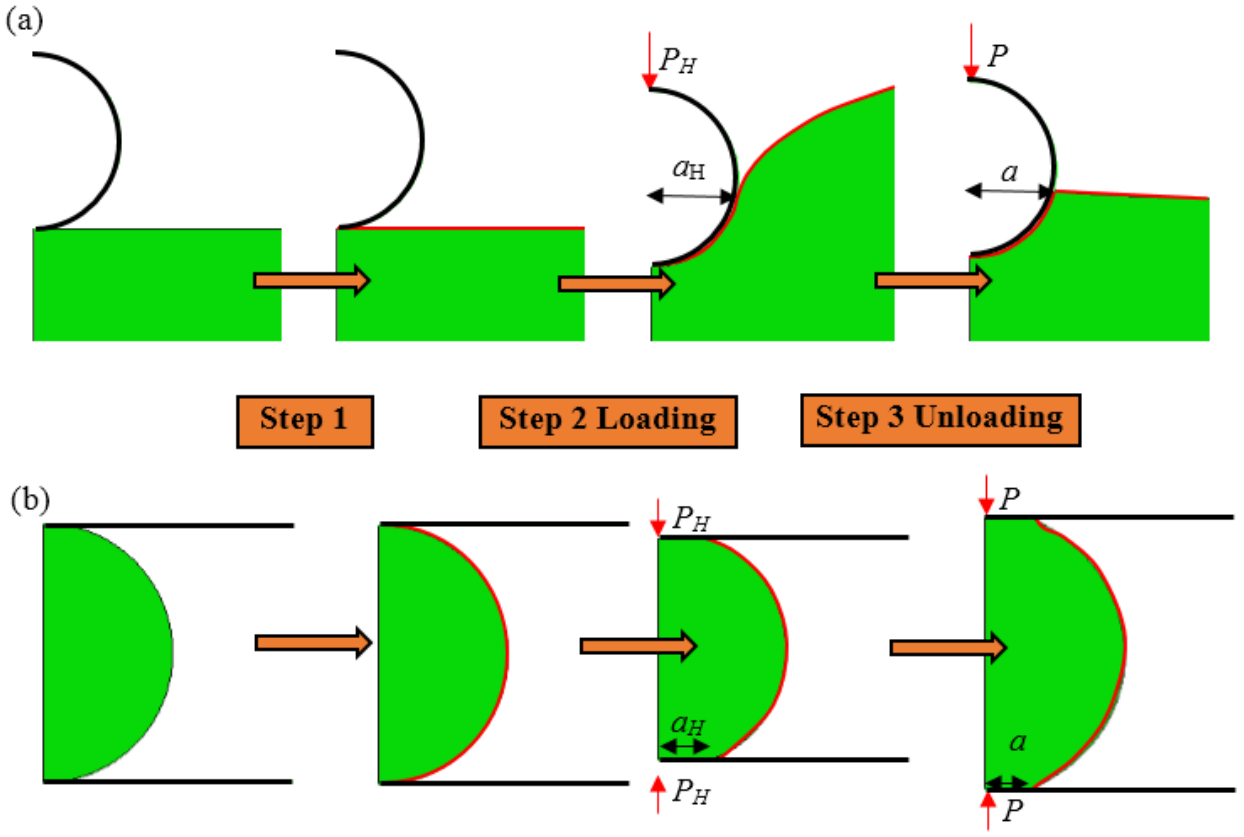

Figure 5.2. Deformation of the elastic parts after each loading step in a simulation with α = 1: (a) a rigid sphere (black line) is brought into contact with an elastic half space; (b) an elastic sphere is placed in between 2 rigid plates (black lines). The thin red layers on the free surface after step 1 symbolizes non-zero surface stress. Step 3 is performed only for adhesive contact.

To compute energy release rate G in the current configuration, we calculate the change in potential energy Π of the system, which is the sum of the elastic strain energy U_E, the surface energy U_S and the potential energy of the applied load $-P\delta$, with a virtual elemental decrease of the current contact area A, i.e.

$$G = -\frac{\partial \Pi}{\partial A}\Big|_{(P,\sigma)} = -\frac{\partial}{\partial A}\left(U_E + U_s - P\delta\right)\Big|_{(P,\sigma)} \tag{5.2}$$

Here, we compute the surface energy U_S as the multiple of constant surface tension σ and the total surface area of the substrate.

Specifically, we evaluate G by carrying out two FEM simulations. In the first, we load the system with P_H in step 2 and unload the system to P in step 3. At the end of this simulation, the contact area is A and the indentation depth is δ. In the second simulation, the system is loaded with ($P_H - dP_H$) in step 2 and unloaded to the same value of P. At the end of the second simulation, the contact area is ($A - dA$), the indentation is ($\delta - d\delta$). The information from these two simulations hence allows us to numerically compute the energy release rate with respect to current configuration using equation (5.2).

5.2.2 FEM Results: Non-Adhesive Contact

FEM results for the non-adhesive contact of two geometries are given in this section. We compare (1) FEM results with different contact conditions, frictionless (x) and no-slip (o); (2) frictionless FEM results in the absence of surface tension with Lin and Chen's prediction in frictionless non-adhesive contact; (3) no-slip FEM results with SST prediction in no-slip non-adhesive contact by Hui *et al.*, which is given by equations (A.5.3) and (A.5.4) in the Appendix 5. The results are presented by normalizing the load P_H and the indentation depth δ_H by the small strain Hertz load $16\mu a_H^2/(3R)$ and the small strain Hertz displacement a_H^2/R respectively. We define indentation depth δ_H as the vertical position of the bottom of rigid sphere with respect to the far-field free

surface of the elastic half space in Fig. 5.1a and the change in distance between the sphere centre to the plates in Fig. 5.1b.

Fig. 5.3a, b plot the normalized load against a_H/R for both geometries at various values of the elasto-capillary number α. In the absence of surface tension, our frictionless (x) FEM results are in excellent agreement with Lin and Chen's results (dashed red line) [16]. In general, the load versus contact radius relation is hardly affected by making the contact frictionless or no-slip, at least when $a_H/R < 0.5$. For larger contacts, the no-slip contact requires a slightly larger load compared to frictionless contact for a given contact area. Fig. 5.3a shows that SST underestimates the load in non-adhesive contact of a rigid sphere and an elastic half space at all values of α when $a_H/R > 0.5$. For non-adhesive contact of an elastic sphere and rigid plates (Fig. 5.3b), the SST underestimates the load for large values of α (surface-tension-dominant), but overestimates the load when α is approaching zero (elasticity-dominant). Furthermore, when α is small (blue and green), the SST seems to be more accurate for the non-adhesive contact of an elastic sphere and rigid plates at $a_H/R > 0.5$in Fig. 5.3a than that in Fig. 5.3b. A plausible reason is that for contact of a rigid sphere and an elastic half space, the SST's approximation of the rigid sphere surface profile as a parabola breaks down at large contact.

(a)

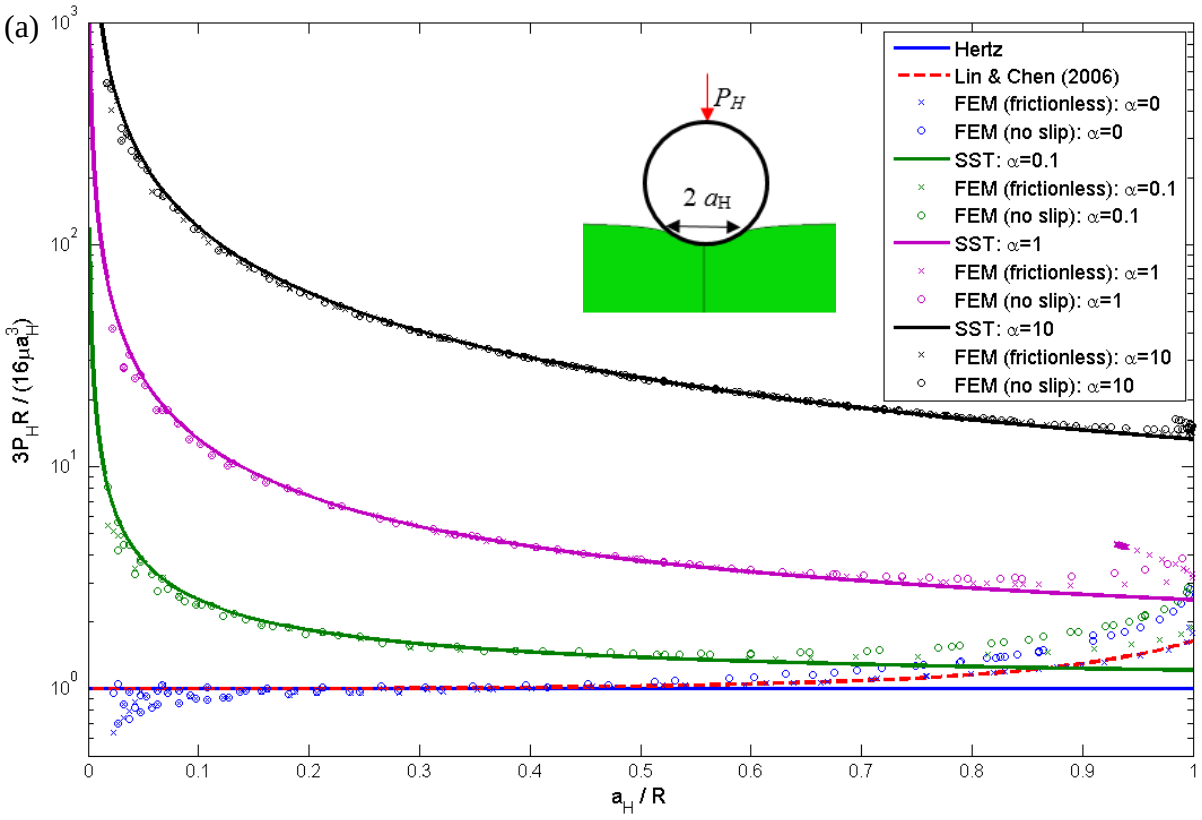
Hertz
Lin & Chen (2006)
FEM (frictionless): α=0
FEM (no slip): α=0
SST: α=0.1
FEM (frictionless): α=0.1
FEM (no slip): α=0.1
SST: α=1
FEM (frictionless): α=1
FEM (no slip): α=1
SST: α=10
FEM (frictionless): α=10
FEM (no slip): α=10
P_H
2 a_H
$3P_H R / (16\mu a_H^3)$
a_H / R
10^3
10^2
10^1
10^0
0
0.1
0.2
0.3
0.4
0.5
0.6
0.7
0.8
0.9
1

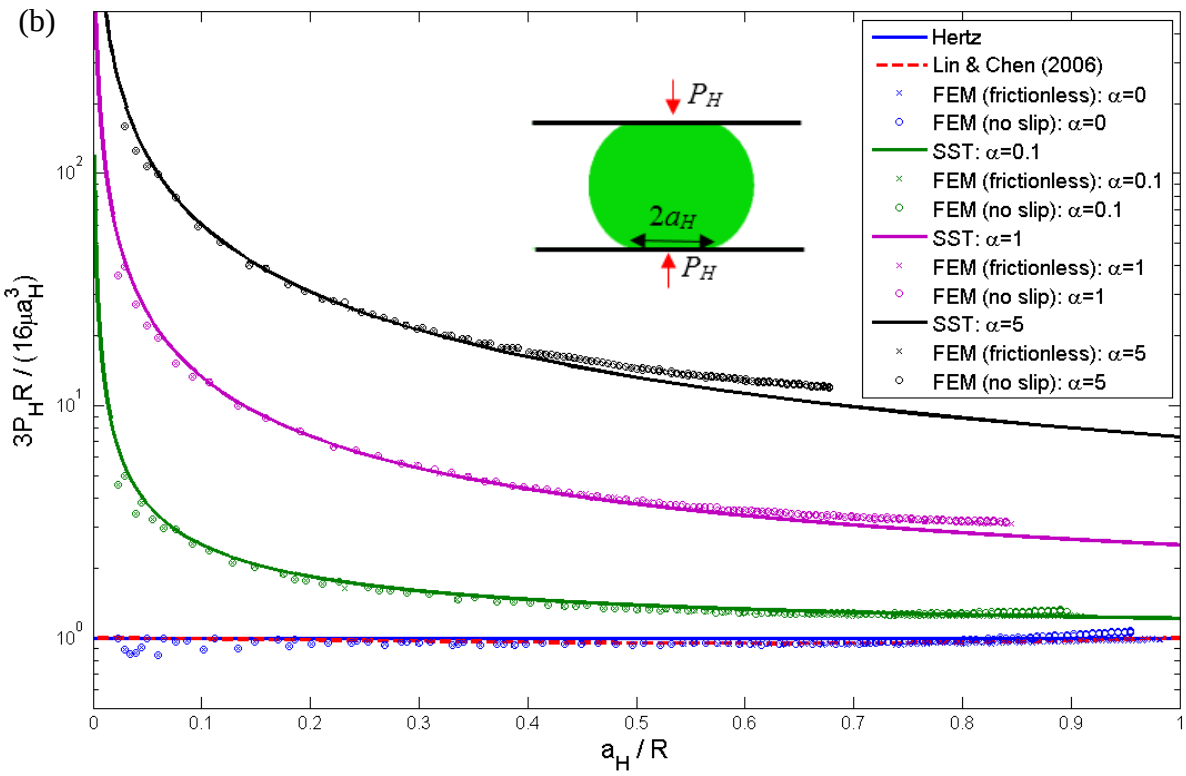

Figure 5.3. Results of non-adhesive contact: normalized load is plotted against a_H/R with varied elasto-capillary number α subject to frictionless (x) or no-slip (o) conditions. (a) A rigid sphere and an elastic half space; (b) an elastic sphere and two rigid plates. Predictions made by the SST (equation (A.5.3.3) in Appendix 5) are plotted in solid lines. Lin and Chen's results are plotted in dashed red line.

Fig. 5.4a, b plots the indentation depth versus contact radius. There is little difference between the FEM results in Fig. 5.4a, b for the frictionless and no-slip contacts, except when contact between a rigid sphere and an elastic half space (Fig. 5.4a) is large and α is small. In contrast to load versus contact radius relation (Fig. 5.3a, b), the SST performs poorly in predicting indentation depth for a given contact radius, especially for the contact between an elastic sphere and rigid plates (Fig. 5.4b). For contacts between a rigid sphere and an elastic half space, Fig. 5.4a shows that an increase in α exaggerates the error between FEM results and the SST.

(a)

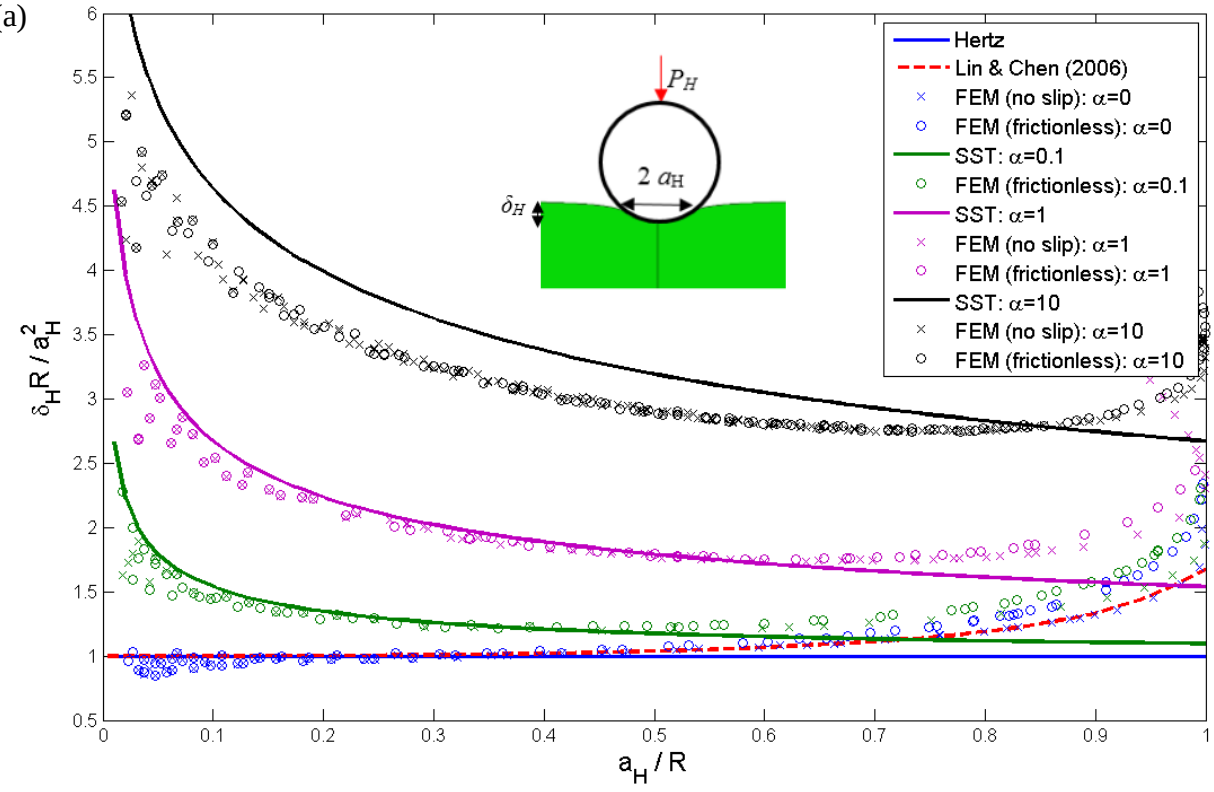
Hertz
Lin & Chen (2006)
FEM (no slip): α=0
FEM (frictionless): α=0
SST: α=0.1
FEM (frictionless): α=0.1
SST: α=1
FEM (no slip): α=1
FEM (frictionless): α=1
SST: α=10
FEM (no slip): α=10
FEM (frictionless): α=10
P_H
$2\,a_H$
δ_H
$\delta_H R / a_H^2$
a_H / R

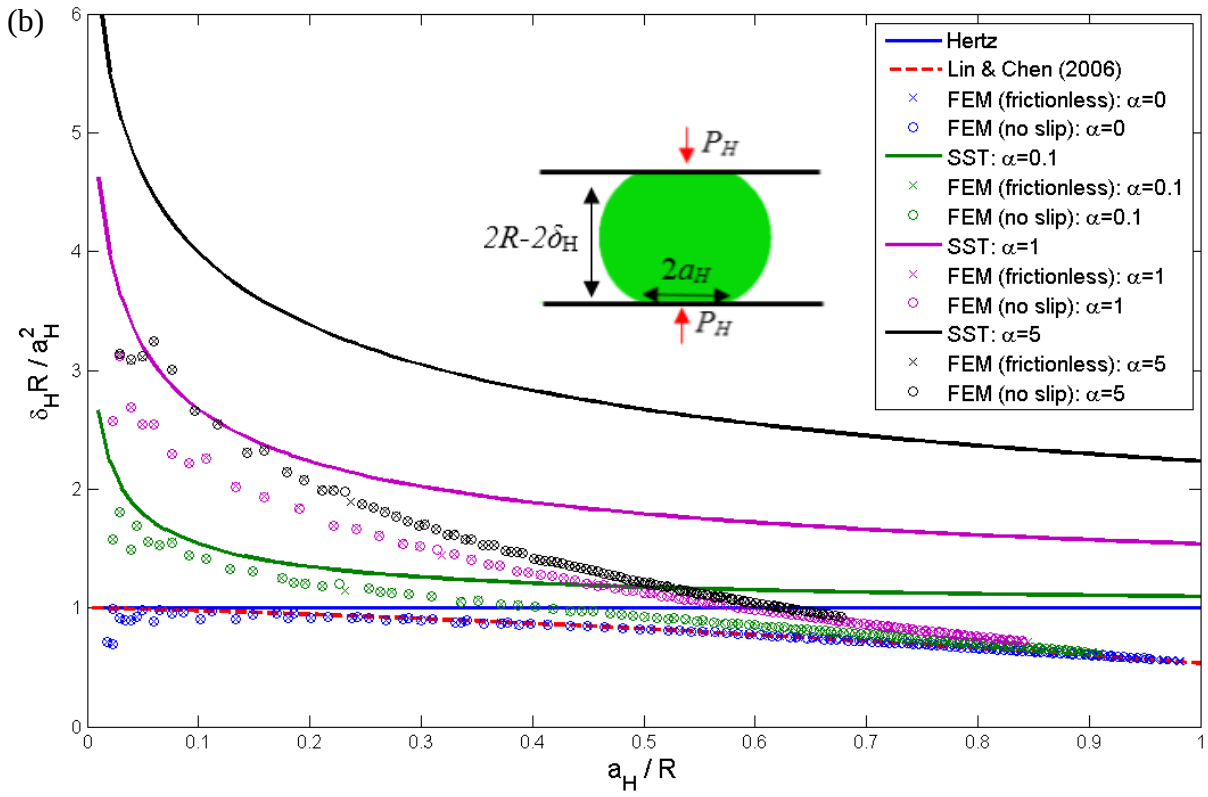

Figure 5.4. Results of non-adhesive contact: normalized indentation depth is plotted against a_H / R with varied elasto-capillary number α subject to frictionless (x) or no-slip (o) conditions. (a) A rigid sphere and an elastic half space; (b) an elastic sphere and two rigid plates.Predictions made by the SST (equation (4) in SI) are plotted in solid lines. Lin and Chen's results are plotted in dashed red line.

In the SST [21], the normalized load and indentation depth for non-adhesive contact are functions of a single parameter $\beta = \dfrac{\sigma}{2\mu a_H}$, see equation (A.5.3 – A.5.4) in Appendix 5. Fig. 5a, b show that equation (A.5.3) in Appendix 5 holds very well for both geometries with either contact condition. Its accuracy is also enhanced by increasing value of α. Consistent with Fig. 5.3a, b, FEM results only start to deviate from the red analytical curve of equation (A.5.3) in Appendix 5 when $a_H / R > 0.5$ (labelled in different colours for different values of α in Fig. 5.5a, b).

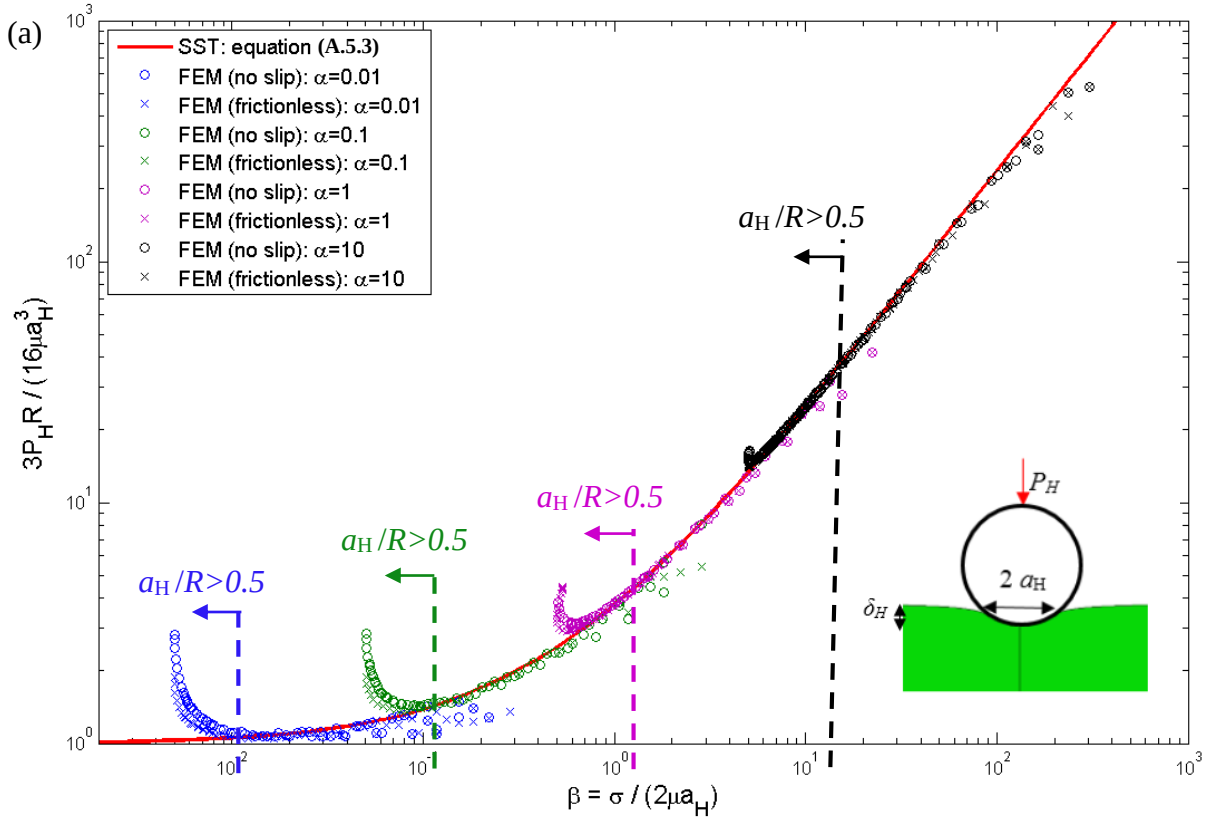
(a)
SST: equation (A.5.3)
FEM (no slip): α=0.01
FEM (frictionless): α=0.01
FEM (no slip): α=0.1
FEM (frictionless): α=0.1
FEM (no slip): α=1
FEM (frictionless): α=1
FEM (no slip): α=10
FEM (frictionless): α=10
$3P_H R / (16\mu a_H^3)$
$\beta = \sigma / (2\mu a_H)$
$a_H/R>0.5$
$a_H/R>0.5$
$a_H/R>0.5$
$a_H/R>0.5$
P_H
$2\,a_H$
δ_H

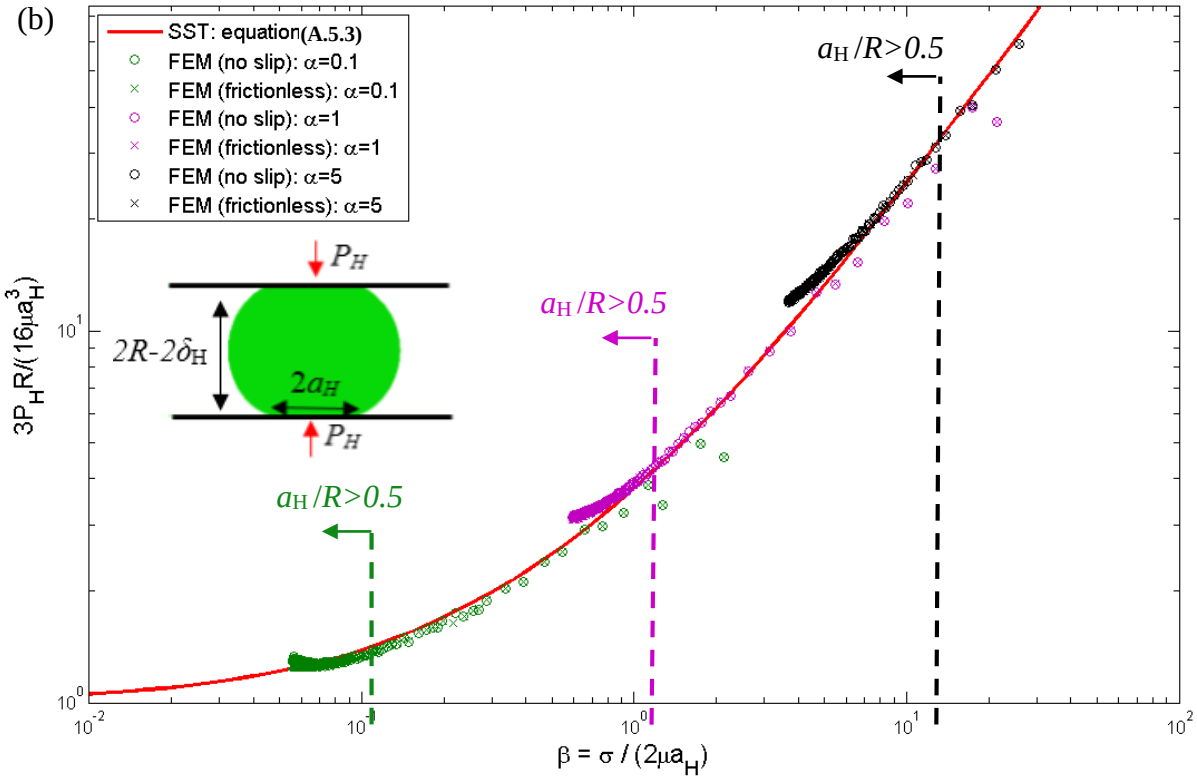

Figure 5.5. Results of non-adhesive contact: normalized load is plotted against β subject to frictionless (x) or no-slip (o) conditions. (a) A rigid sphere and an elastic half space; (b) an elastic sphere and two rigid plates. Predictions made by the SST (equation (3) in SI) are plotted in solid red line.

On the other hand, equation (A.5.4) in SST (see Appendix 5) did poorly in predicting indentation depth for a given value of β, as shown in Fig. 5.6. This is particular so in Fig. 5.6b for contact between an elastic sphere and rigid plates, equation (A.5.4) overestimates the normalized indentation depth in the whole range of β, possibly due to the finite size of the elastic sphere.

(a)

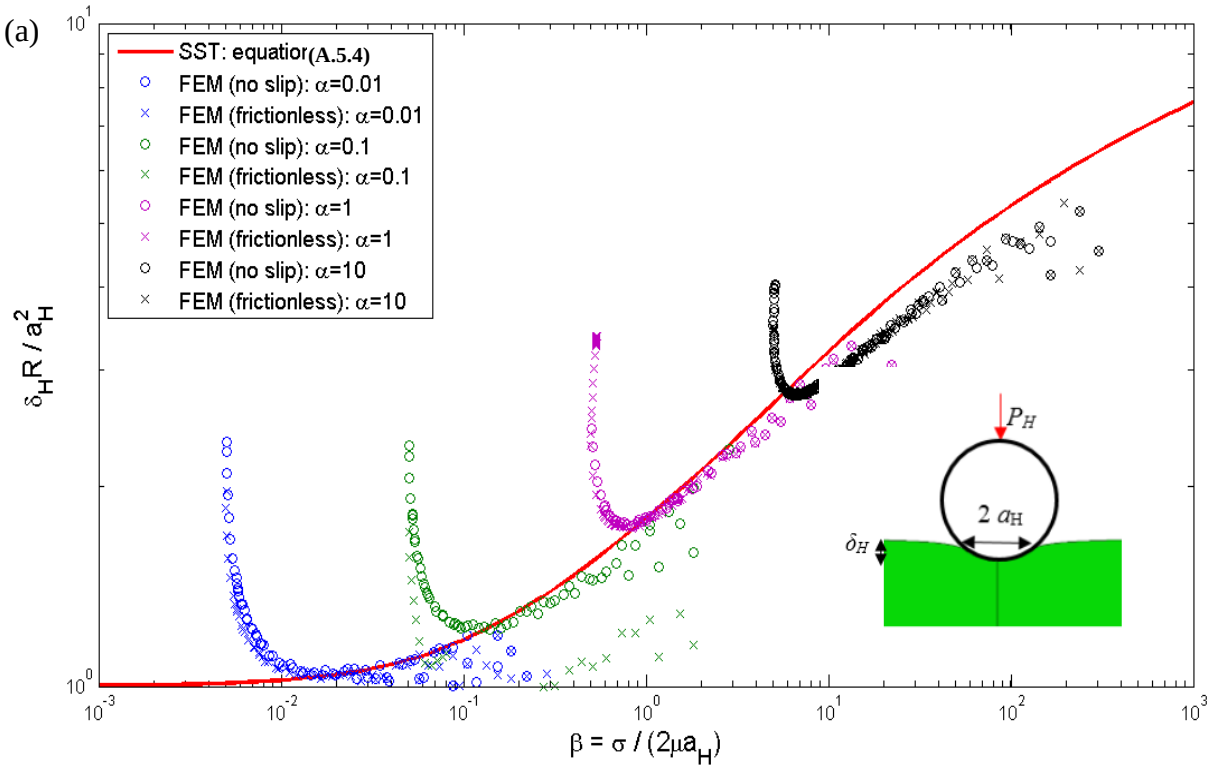
SST: equation (A.5.4)
FEM (no slip): α=0.01
FEM (frictionless): α=0.01
FEM (no slip): α=0.1
FEM (frictionless): α=0.1
FEM (no slip): α=1
FEM (frictionless): α=1
FEM (no slip): α=10
FEM (frictionless): α=10
$\delta_H R / a_H^2$
$\beta = \sigma / (2\mu a_H)$
P_H
$2\ a_H$
δ_H

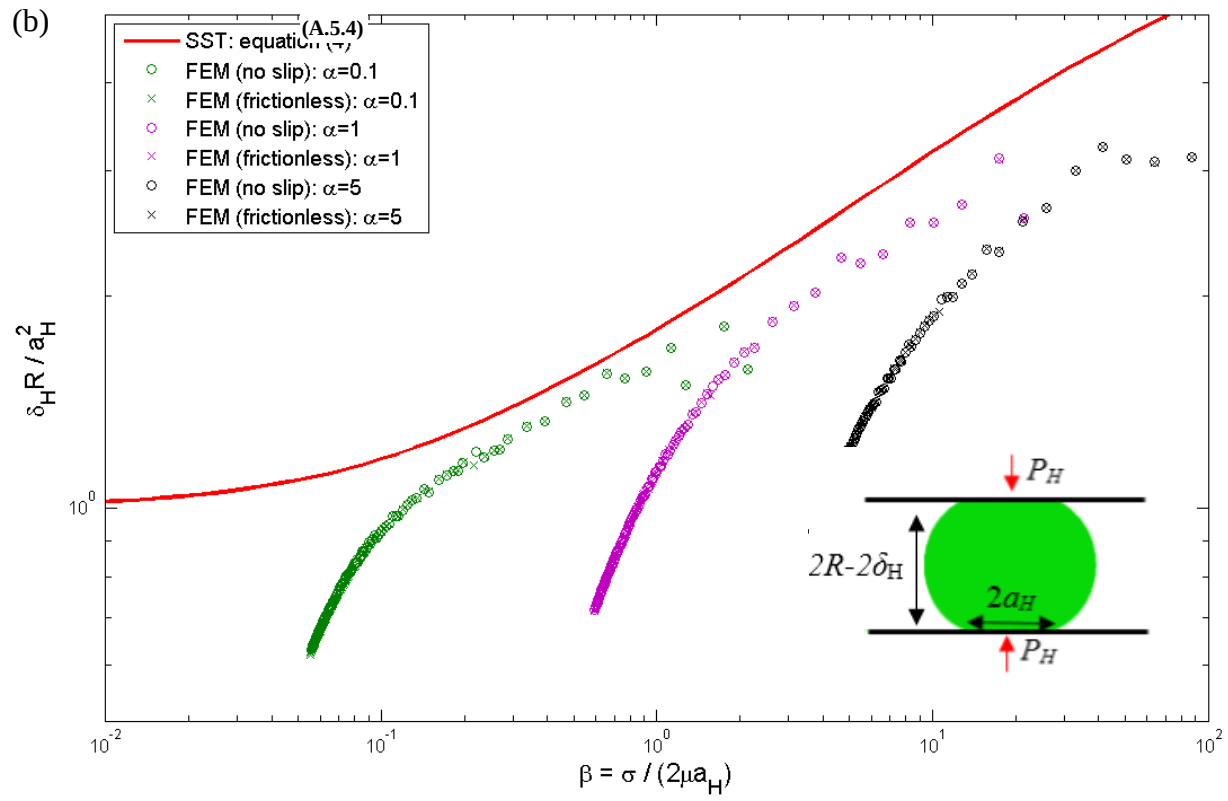

Figure 5.6. Results of non-adhesive contact: normalized indentation depth is plotted against *β* subject to frictionless (x) or no-slip (o) conditions. (a) A rigid sphere and an elastic half space; (b) an elastic sphere and two rigid plates. Prediction made by the SST (equation (A.5.4) in Appendix 5) are plotted in solid red line.

5.2.3 FEM Results: Adhesive Contact

In the previous section, we show that the SST predicts load much more accurately than indentation depth for non-adhesive contacts. Hence in this section, we only compare FEM results with the SST on relation between load and contact radius in adhesive contacts.

Lin and Chen [16] solved the adhesion problem without considering surface tension by implementing a cohesive zone model to describe the adhesive interaction. Here we follow the philosophy of JKR theory by including adhesion indirectly in our finite element model – adhesion is realized by not allowing surface separation in the contact region during unloading. Thus we are able to compute the energy release rate G with respect to the current configuration at a given load P and a contact area A via equation (5.2). A drawback of this approach is that it is difficult to enforce a fixed value of energy release rate (i.e., $G = W_{ad}$) in our simulation. To do this, we have to carry out a large number of simulations, interpolate the results to find a particular set of load and contact radius such that G is constant.

We first compare our FEM results in the absence of surface tension to JKR theory and Lin and Chen's results of frictionless adhesive contacts [16] in Fig. 5.7a, b. Here we employ the same normalization scheme as Lin and Chen [16]. Fig. 5.7a, b show that our results are consistent with theirs, thus validating our finite element method. Notice that the simulations subjected to different contact conditions (frictionless (x) or no-slip (o)) are very similar in load versus contact radius relation with this normalization scheme.

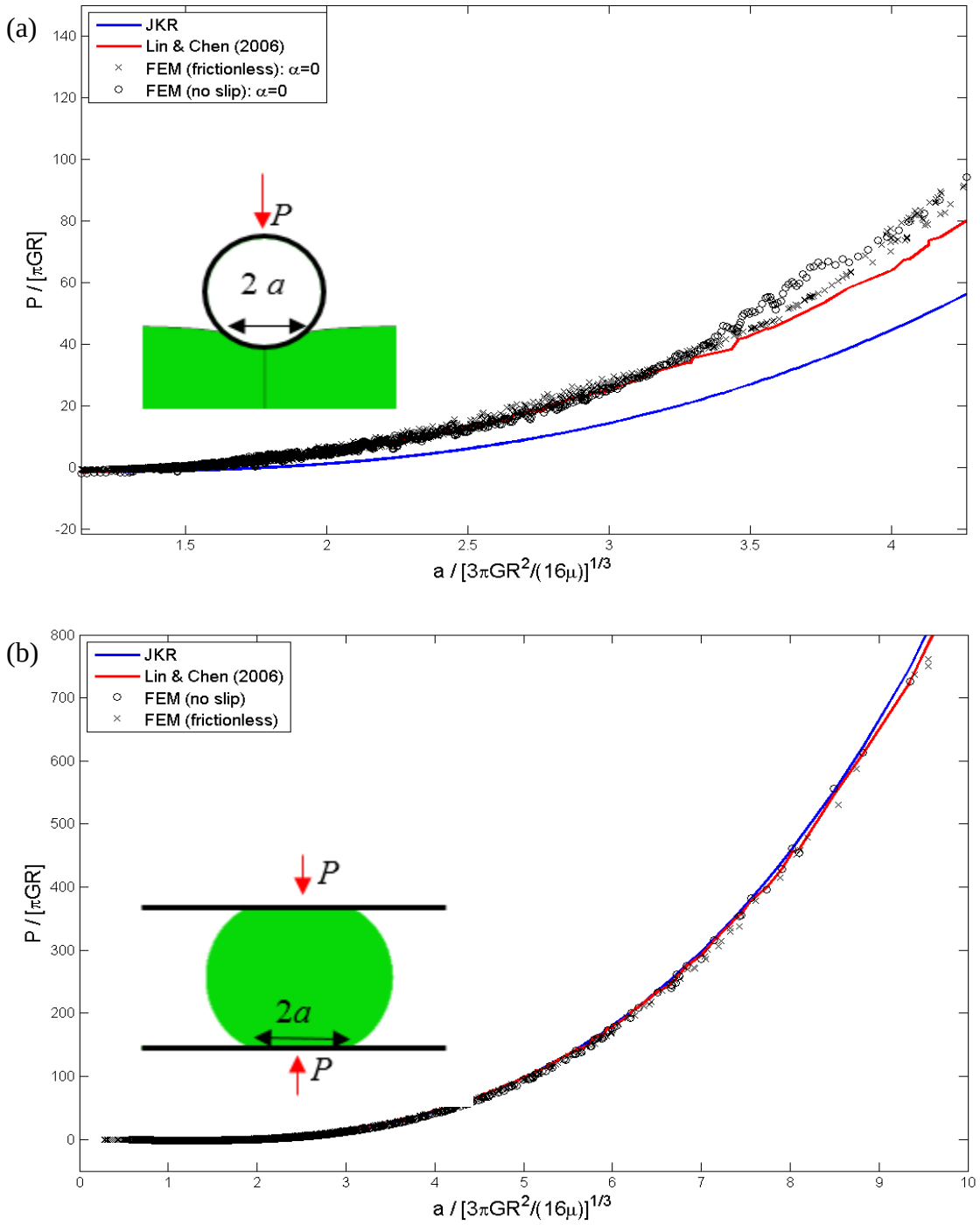

Figure 5.7. FEM results of adhesive contact are compared to JKR theory as well as Lin and Chen [16]: normalized load is plotted against normalized contact radius subject to frictionless

(x) or no-slip (o) conditions. (a) A rigid sphere and an elastic half space; (b) an elastic sphere and two rigid plates.

To further explore the coupled effect of surface tension and large deformation, we exam the relation between $G/\mu R$ and a/R at different values of $P/\mu R^2$ and α in Fig. 5.8 - 5.10.

Fig. 5.8a, b present FEM results at $\alpha = 1$, which falls in the range of elasto-capillary numbers that are typically seen in experimental studies [13, 15] of soft gels. Three normalized external loads $P/\mu R^2$ are considered, including a pushing force of $P/\mu R^2 = 1$, zero external load $P/\mu R^2 = 0$ (consistent with experiments reported in [13]) and a large pulling force of $P/\mu R^2 = -1$ (consistent with experiments reported in ref. 15). It shows in Fig. 5.8a, b that whether the contact is frictionless or no-slip has significant influence on the relation between the energy release rate and contact radius - at a given load, a much higher energy release rate is needed to maintain the same contact radius for frictionless contact. This phenomenon is due to slipping of contacting surface. One has to substantial increase the applied compressive load in step 2 so that at the end of the step 3, the contact radius (after slip) is the same as the no slip contact case. This phenomenon is not reflected in Fig. 5.7a, b, because the normalized variables on both axes involves the energy release rate. Fig. 5.8a, b also compare the prediction of Hui *et al.*'s small strain theory (SST) [21].

Fig. 5.8a shows that the SST adhesion theory for no slip contact is accurate as long as the contact radius is less than half of the sphere radius. On the other hand, Fig. 5.8b shows that the SST is surprisingly good at describing the no-slip contact of an elastic sphere and rigid plates - its prediction agrees with no-slip FEM results to a much larger contact radius (a/R~1), even though it was initially derived for a rigid sphere contacting with an elastic half space. Details of computing

energy release rate based on the SST are given in the SI. Here we noted that contact area is computed as $A = \pi a^2$ in the SST, which is valid for contact of an elastic sphere between rigid plates. For large contact of a rigid sphere and an elastic half space, this approximation underestimates contact area for a given contact radius, and will lead to an underestimation of the energy release rate.

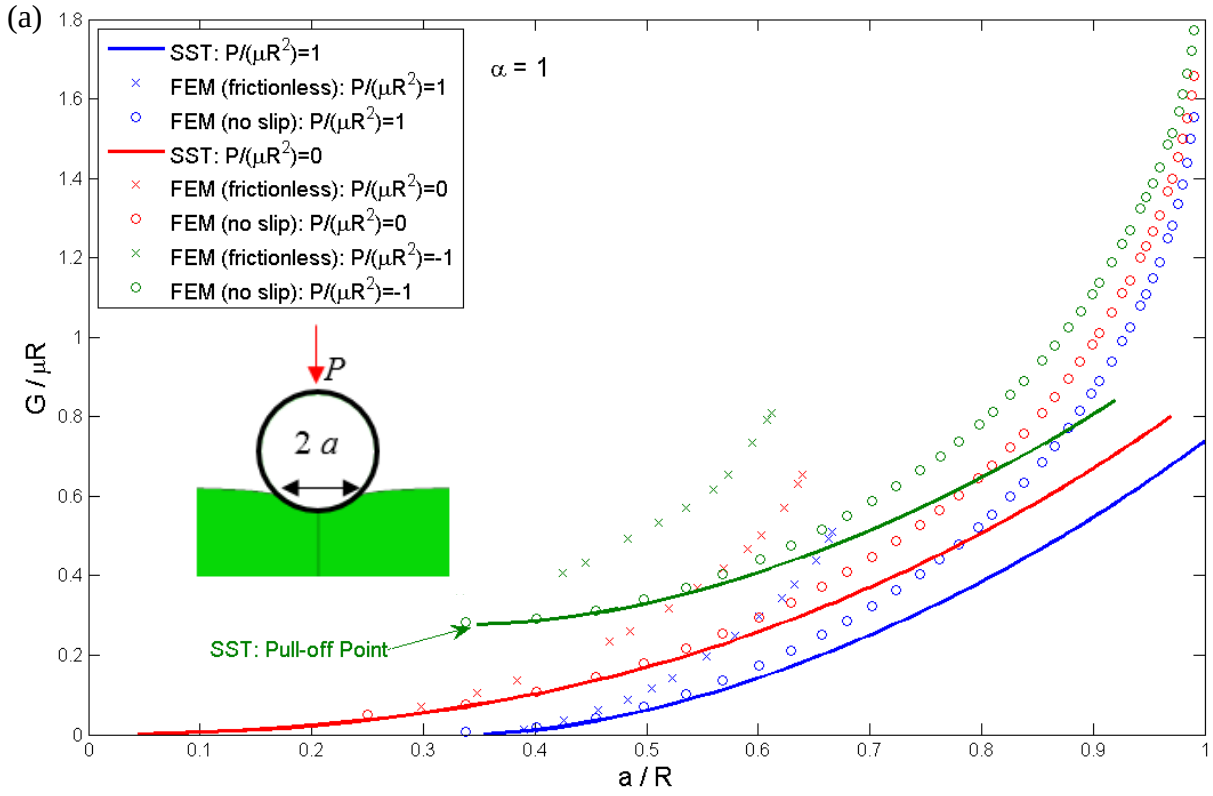

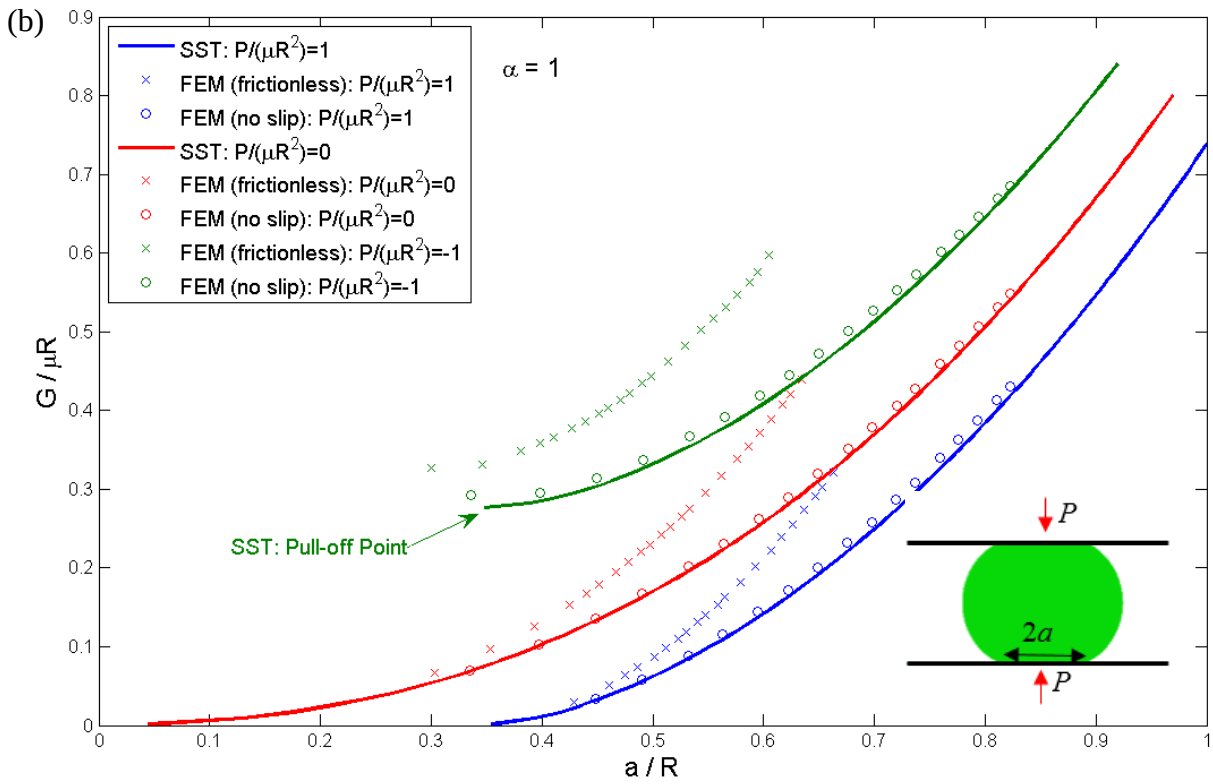

Figure 5.8. Results of adhesive contact at α=1: normalized energy release rate is plotted against normalized contact radius subject to frictionless (x) or no-slip (o) conditions. (a) A rigid sphere and an elastic half space; (b) an elastic sphere and two rigid plates. Predictions made by the SST are plotted in solid lines.

In Fig. 5.9 and 5.10, we varied the value of α while keeping the external loading condition constant - zero load in Fig. 5.9 and $P/\mu R^2 = -1$ in Fig. 5.10. Consistent with Fig. 5.8, higher energy release rate is required to maintain the same contact radius if the interface is frictionless. In particular, when α=10 (in Fig. 5.9a and 5.10a), the compressive force required to produce the same contact radius as the no slip contact case, resulting in deformation so large that it exceeds the capability of our finite element model. Hence the results of frictionless contact at α=10 are missing from Fig. 5.9a and 5.10a. The SST is again accurate to much larger contacts for the geometry in Fig. 5.9b and 5.10b. In addition, for the geometry in Fig. 5.9b and 5.10b (elastic sphere between

rigid plates), the SST tends to overestimate the energy release rate at a given contact radius for no-slip contact when $\alpha < 1$. In all other cases (also see Fig. 5.9a and 5.10a), the SST underestimates the energy release rate.

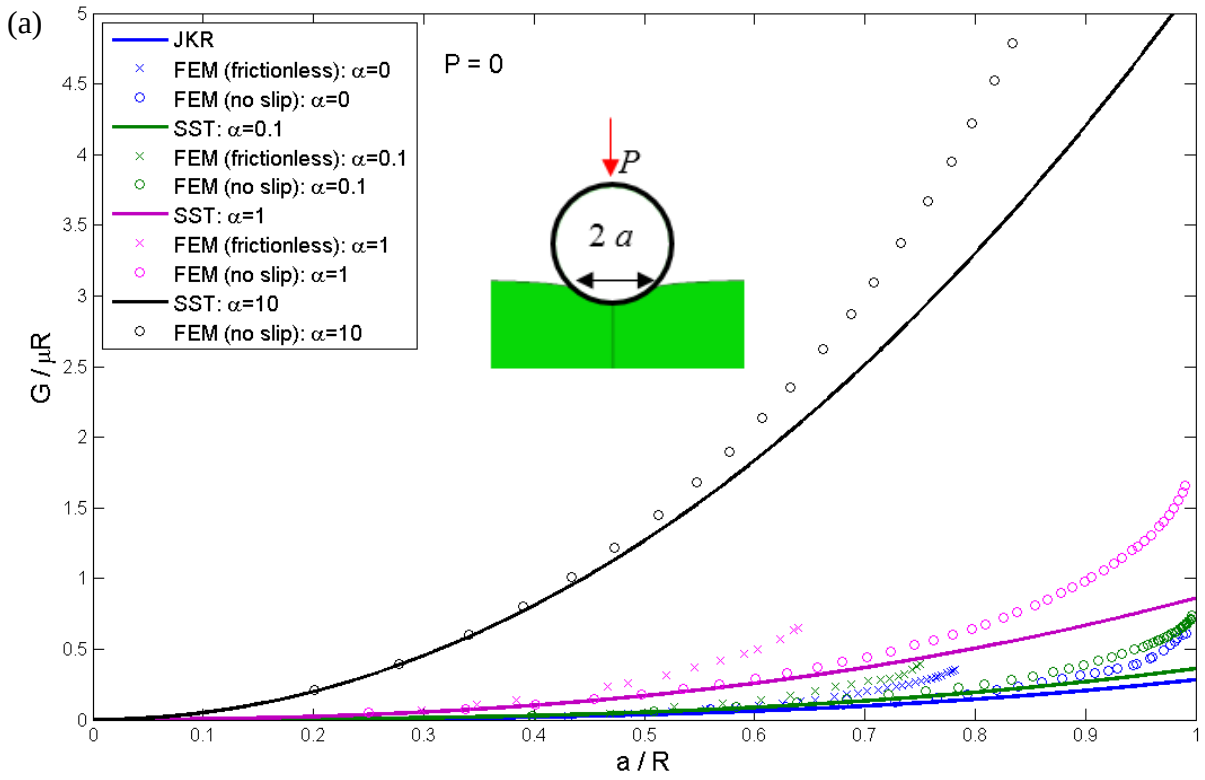

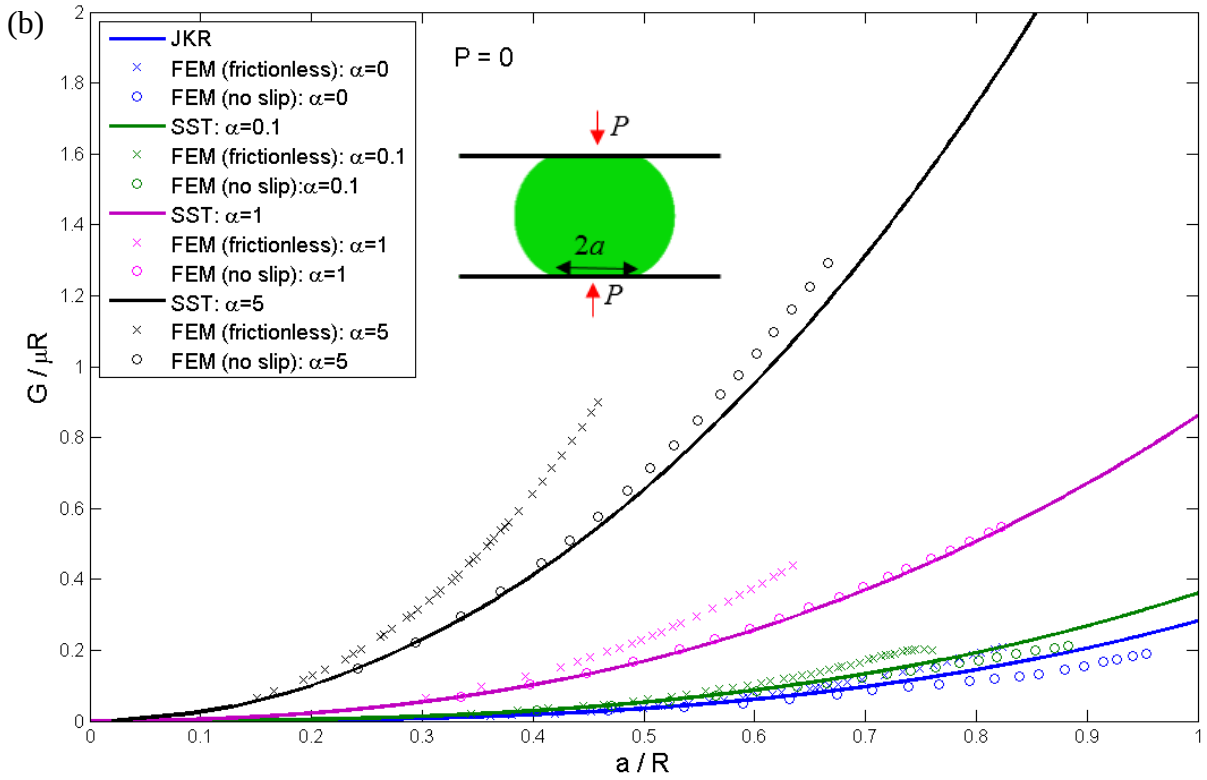

Figure 5.9. Results of adhesive contact at zero load: normalized energy release rate is plotted against normalized contact radius subject to frictionless (x) or no-slip (o) conditions. (a) A rigid sphere and an elastic half space; (b) an elastic sphere and two rigid plates. Predictions made by the SST are plotted in solid lines.

(a)

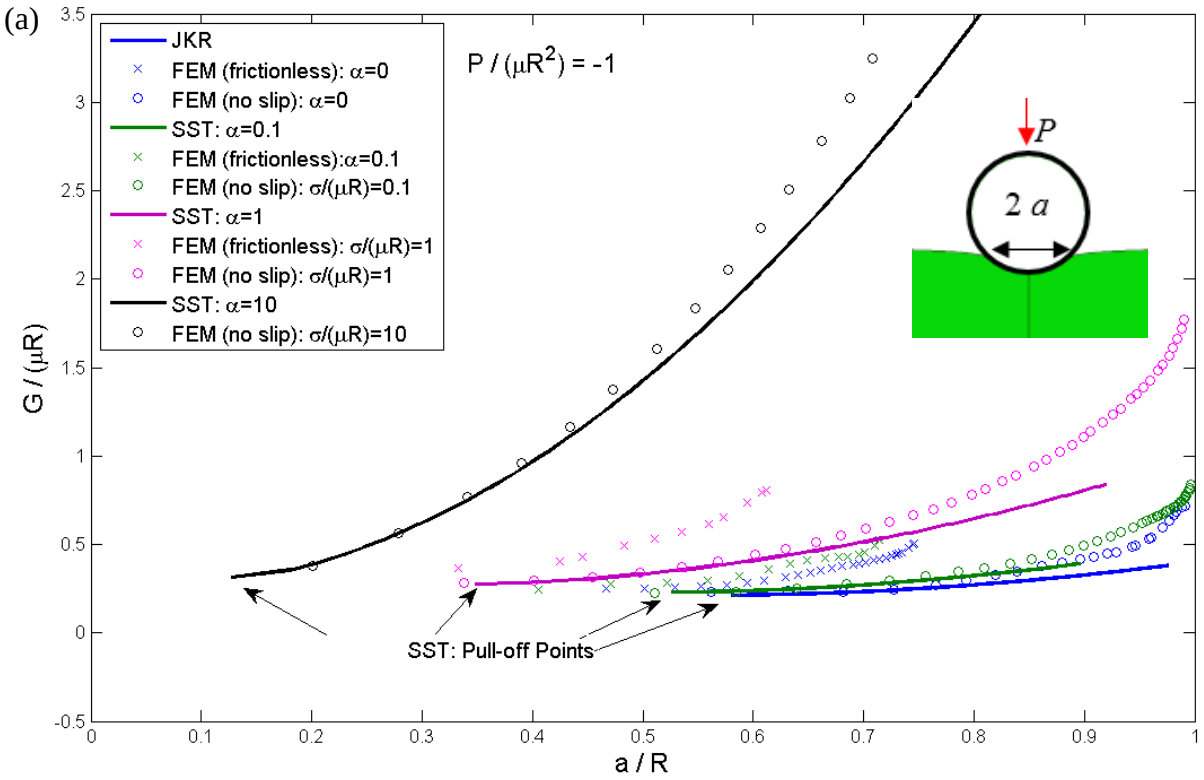
JKR
FEM (frictionless): α=0
FEM (no slip): α=0
SST: α=0.1
FEM (frictionless):α=0.1
FEM (no slip): σ/(μR)=0.1
SST: α=1
FEM (frictionless): σ/(μR)=1
FEM (no slip): σ/(μR)=1
SST: α=10
FEM (no slip): σ/(μR)=10
P / (μR^2) = -1
P
2 a
SST: Pull-off Points
G / (μR)
a / R
3.5
3
2.5
2
1.5
1
0.5
0
-0.5
0
0.1
0.2
0.3
0.4
0.5
0.6
0.7
0.8
0.9
1

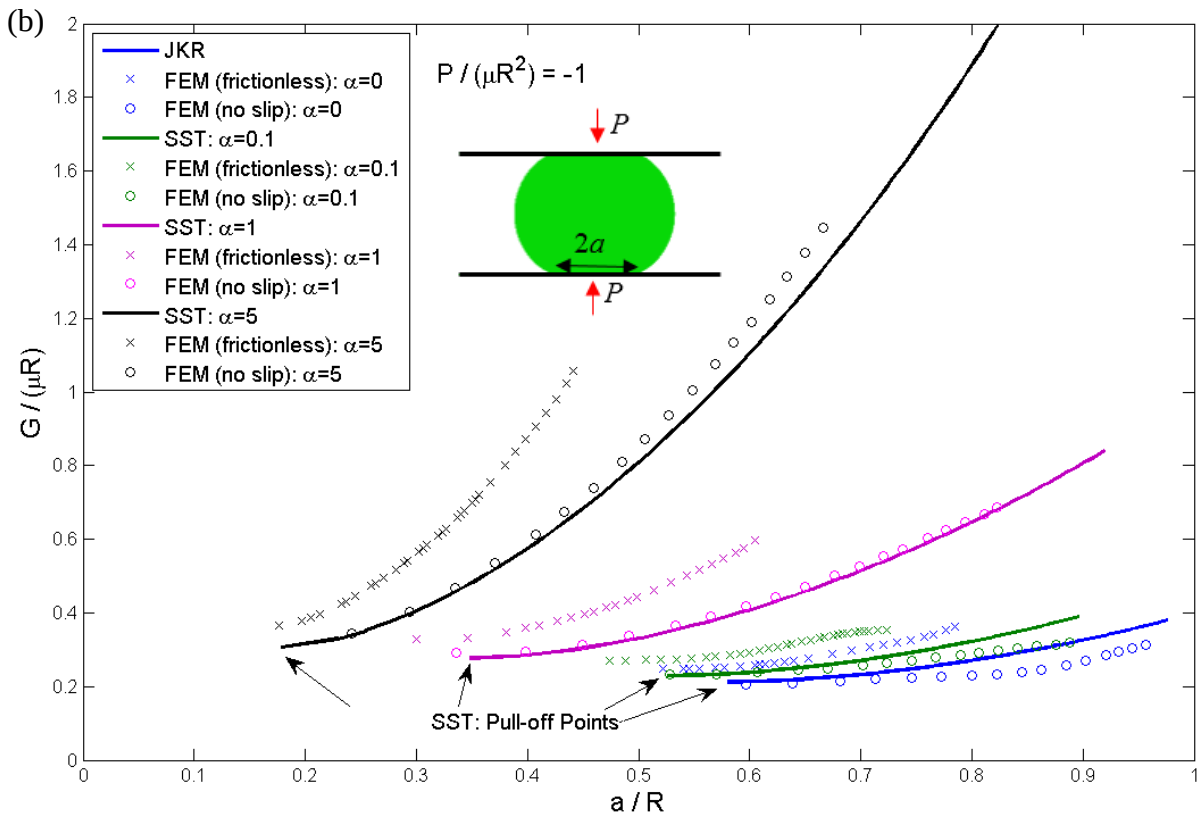

Figure 5.10. Results of adhesive contact at normalized load of -1: normalized energy release rate is plotted against normalized contact radius subject to frictionless (x) or no-slip (o) conditions. (a) A rigid sphere and an elastic half space; (b) an elastic sphere and two rigid plates. Predictions made by the SST are plotted in solid lines.

An important aspect of the SST proposed by Hui *et al.* [21] is that if the load P and contact radius a are normalized by the pull-off load $\hat{P} = \dfrac{P}{(3/2)\pi W_{ad} R}$ and the pull-off contact radius $\hat{a} = \dfrac{2a}{\left(9\pi W_{ad} / 4\mu\right)^{1/3} R^{2/3}}$ in the elasticity dominant limit respectively, then the relationship between them depends only on the single parameter $\omega = \dfrac{\sigma / \mu R}{\left(9\pi W_{ad} / 4\mu R\right)^{1/3}}$. To check if this result (equation (A.5.1) in Appendix 5) holds in large contact, we interpolated FEM results for three different

values of ω (0.1, 1 and 5) and plot $\hat{a}$ versus $\hat{P}$ in Fig. 5.11. The interpolated FEM no slip contact results agree well with the stable branch of equation (A.5.1) in Appendix, which is derived based on no slip contact. In particular, this agreement improves with increasing ω, where surface tension is expected to dominate. Consistent with results of non-adhesive contact in Fig. 5.3a, b, SST tends to underestimate load for a given contact radius expect for the case of an elastic sphere between rigid plates (Fig. 5.11b) and ω is small.

(a)

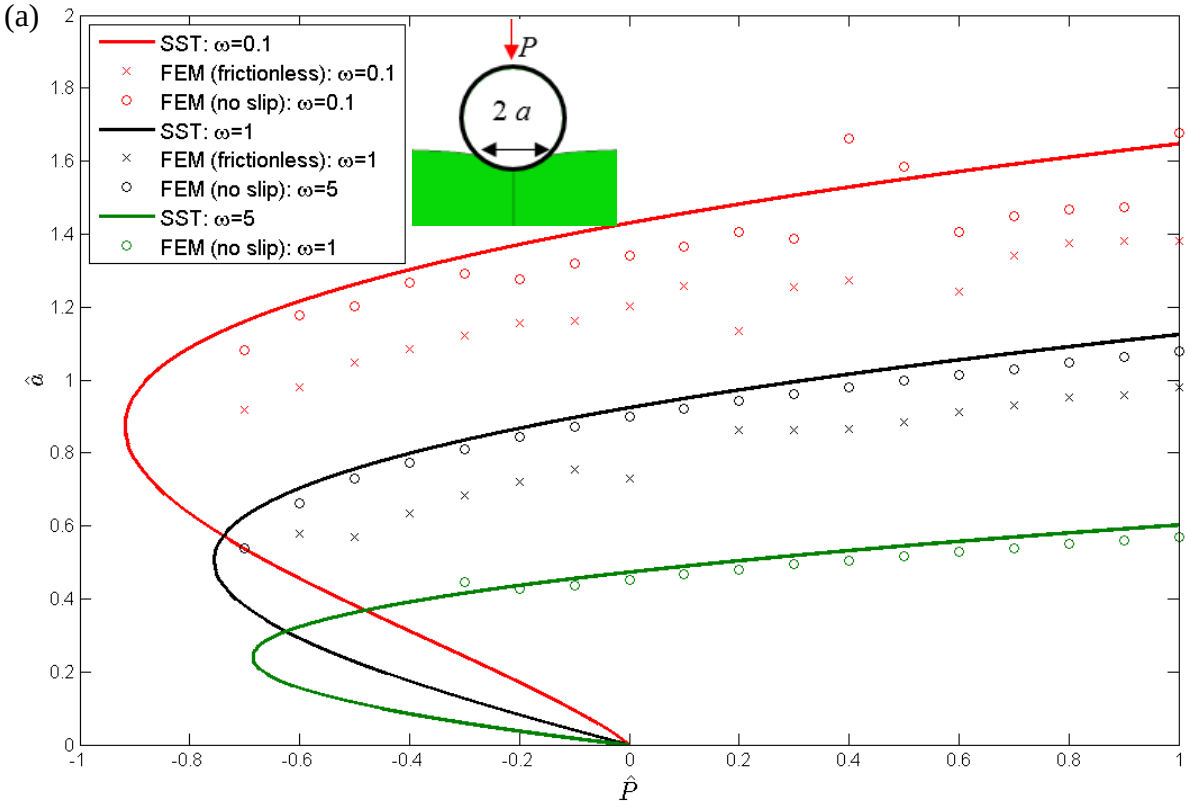

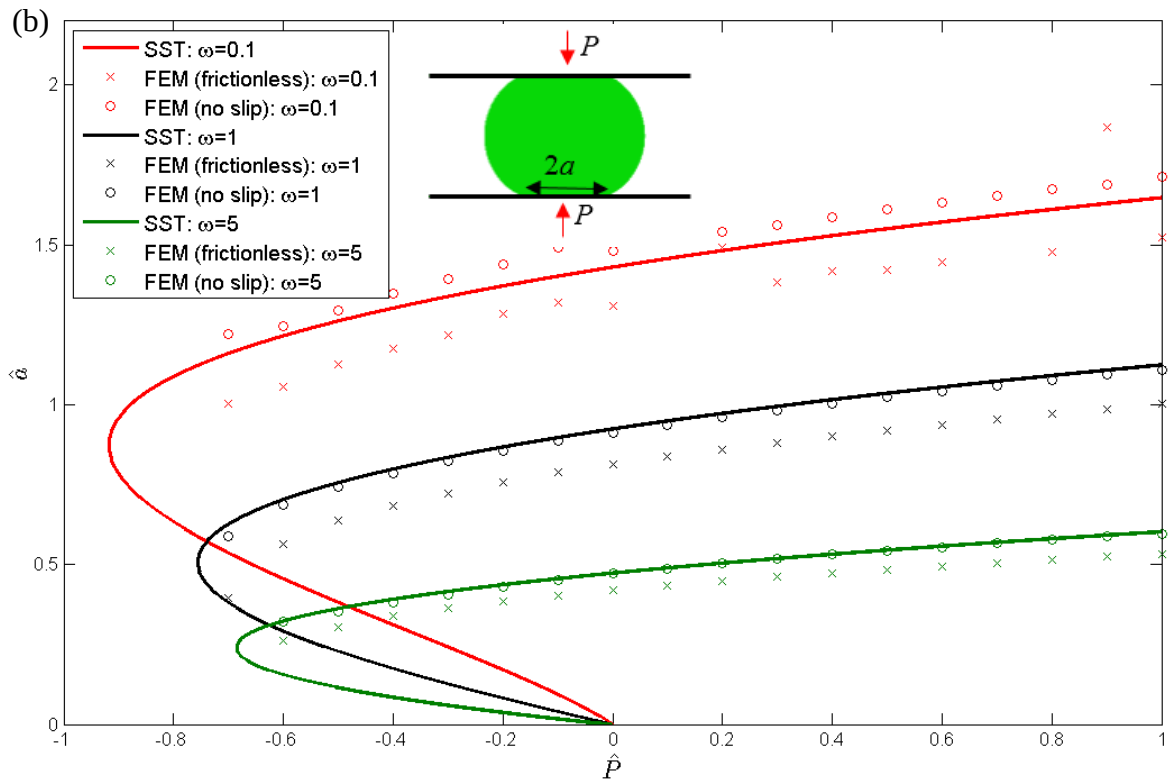

Figure 5.11. Results of adhesive contact: normalized contact radius is plotted against normalized load in systems with varied ω subject to frictionless (x) or no-slip (o) conditions. (a) A rigid sphere and an elastic half space; (b) an elastic sphere and two rigid plates. FEM results are interpolated and predictions made by the SST (equation (1) in SI) are plotted in solid lines.

5.3. Conclusions and Discussion

We study contact mechanics between (a) a rigid sphere and an elastic half space and (b) an elastic sphere and rigid plates. Using the finite element method, we are able to simulate contacts with either frictionless or no-slip contact condition beyond the small strain limit. The effect of surface tension is incorporated in our model using a set of user-defined surface elements on the free surface of the elastic body. We assume a constant surface tension on elastic surfaces both inside and

outside the contact. We study both the non-adhesive and adhesive contacts in this work and compare our finite element results to (1) the classic Hertz and JKR theories; (2) Lin and Chen's [16] finite element study on frictionless contacts without considering surface tension outside the contact; (3) Hui *et al.*'s [21] small strain theory (SST) on no-slip contacts incorporating the effect of surface tension. The key findings of our study are listed below:

For non-adhesive contact problems:

1. Our results of frictionless contact in the absence of surface tension agree well with Lin and Chen [16].
2. The two contact conditions lead to similar results up to very large contact.
3. As far as the load versus contact radius is concerned, our results show that the SST is an excellent approximation for no-slip contact, at least when $a_H / R < 0.5$. The normalized load $3P_H R/\left(16\mu a_H^3\right)$ can be determined by a single parameter $\beta = \sigma / 2\mu a_H$ as described in equation (A.5.3) when $a_H / R < 0.5$.
4. The SST gives reasonable predictions of indentation depth *only* for the non-adhesive contact between a rigid sphere and an elastic half space when $a_H / R < 0.5$ at smaller values of the elasto-capillary number, e.g. $\alpha \le 1$. The indentation depth versus contact radius relation deviates considerably from the SST for the contact between an elastic sphere and two rigid plates. This is because the finite-size elastic sphere can be represented as an elastic half space (an assumption of SST) only when $a_H / R << 1$. The breakdown of this assumption leads to overestimation of indentation depths since the sphere becomes stiffer

with increasing contact area. Noticeably, the computation of indentation depth in the SST is much more sensitive to the breakdown of this assumption than the load calculation.

For adhesive contact problems:

1. In the absence of surface tension and frictionless contact, we show that our FEM result of load versus contact radius relation agrees with Lin and Chen [16].
2. At a given external load, the SST's prediction of the energy release rate versus contact radius relation is consistent with our FEM results of no-slip contact when $a_H / R < 0.5$.
3. Even though SST is originally derived for the contact between a rigid sphere and an elastic half space, it works surprisingly well for the contact between an elastic sphere and two rigid plates. Especially at $\alpha = 1$, SST's prediction of no-slip contact agrees well with our FEM results up to a contact radius of $a / R \sim 1$, much better than the case of a rigid sphere in adhesive contact with an elastic half space.
4. In contrast to non-adhesive contact, frictionless contact leads to substantially smaller contact radius for a given energy release rate and external load.

There are several limitations in this work. In our finite element model, the work of adhesion cannot be prescribed directly. Instead, we calculate the energy release rate of the contact configuration. Therefore the computational cost is very high because a very large number of simulations are required to interpolate the results accurately. We account for material nonlinearity using a neo-Hookean constitutive model, which tends to underestimate strain hardening at very large

deformation. In practice, there is no difficulty extending our numerical study to more realistic elastic model which correctly captures strain hardening behavior. In our finite element analysis, surface stress is assumed to be isotropic and independent of stretch, which may not be true in real surfaces. Although our user-defined surface elements can be modified to capture the dependence of surface stress on surface strain, there are very limited experimental data on this dependence. Furthermore, frictionless and no-slip conditions considered in this work are two idealized situations, in practice, partial slip can occur on the surface. The interrelation between friction, adhesion and surface stress remains an unsolved problem.

Acknowledgement

This work was supported by the U.S. Department of Energy, Office of Basic Energy Sciences, Division of Materials Sciences and Engineering under Award DE-FG02-07ER46463.

Appendix 5 Review of Hui et al.'s Small Strain Theory (SST)

In this section we outline the theoretical approach proposed by Hui *et al.* [21] to incorporate surface tension effect into JKR theory in small deformation regime. For detailed derivation of their result, consult [21].

In the spirit of JKR theory, Hui *et al.*'s treatment of adhesive interactions is also based on an energy balance. The air gap outside the contact region is viewed as an external crack. The indentation load to contact radius relation is determined at equilibrium by equating the energy release rate G of the external crack to the interfacial work of adhesion W_{ad}. Specifically, they considered a situation where a rigid sphere of radius R was brought into contact with an elastic half space of shear modulus μ and surface tension σ under the action of a vertical load P. For simplicity, they assumed a no-slip boundary condition that allows one to consider only the surface tension of the half space surface outside the contact.

Using the formulation of non-adhesive contact of a rigid sphere to an elastic half space given by Long *et al.* [26] as a starting point, a surface tension dependent 'Hertz-like' relation between load P_H, indentation depth δ_H and contact radius a was obtained. The subscript 'H' refers to non-adhesive 'Hertz-like' contact. This relation leads to an expression of contact compliance $C(a) = d\delta_H / dP_H$, which determines the change of potential energy of the system per unit change in contact area, i.e. the energy release rate $G = -\frac{1}{4\pi a}\frac{dC}{da}\left(P - P_H\right)^2$ [27].

Notably, Hui *et al.* [21] introduced a new normalization scheme, in which the indentation load P and contact radius a are normalized by the magnitude of pull-off load and pull-off contact radius in the limit of zero surface tension.

$$\hat{P} = \frac{P}{(3/2)\pi W_{ad} R};\ \hat{a} = \frac{2a}{\left(9\pi / W_{ad} 4\mu\right)^{1/3} R^{2/3}};\ \hat{\delta} = \frac{12\delta}{\left(9\pi / W_{ad} 4\mu\right)^{2/3} R^{1/3}};\ \beta = \frac{\sigma}{2\mu a}$$

With this normalization, the relation between indentation force and contact radius is found to depend on a single dimensionless parameter $\omega = \beta\hat{a}$. Equation (A.5.1) and (A.5.2) are the key results obtained in [21].

$$\hat{P} = \bar{P}_H(\beta)\hat{a}^3 - 2\sqrt{\frac{\hat{a}^3}{\Lambda(\beta)}} \tag{A.5.1}$$

$$\hat{\delta} = 3\hat{a}^2\bar{\delta}_H(\beta) - 4\phi(\beta)\sqrt{\frac{\hat{a}}{\Lambda(\beta)}} \tag{A.5.2}$$

where

$$\bar{P}_H(\beta) = \frac{3P_H R}{16\mu a^3} \approx 1 + \frac{3\pi\beta}{4}\left[\frac{\beta^2 + 0.6016\beta + 0.0171}{\beta^2 + 0.3705\beta + 0.0063}\right] \tag{A.5.3}$$

$$\bar{\delta}_H(\beta) = \frac{\delta_H R}{a^2} \approx 1 + \frac{1}{3}\ln\left[1 + 6.582\beta + 2.759\beta^2 + 0.3782\beta^3\right] \tag{A.5.4}$$

$$\begin{cases} \Lambda(\beta) = \phi(\beta) + \beta\dfrac{d\phi(\beta)}{d\beta} \\ \phi(\beta) = \dfrac{0.6425\beta^2 + 4.284\beta + 1}{0.2039\beta^3 + 3.994\beta^2 + 6.011\beta + 1} \end{cases} \tag{A.5.5}$$

Equations (A.5.3) and (A.5.4) depict a non-adhesive contact behaviour assuming no-slip boundary condition inside the contacting region. As in JKR theory, Hui *et al.*'s analysis was based on small strain linear elastic theory, which requires $W_{ad} / \mu R$ to be much less than max{1, $\sigma / \mu R$ }.

References

[1]. Shull, K. R. (2002). Contact mechanics and the adhesion of soft solids. Materials Science and Engineering: R: Reports, 36(1), 1-45.

[2]. Liu, K. K. (2006). Deformation behaviour of soft particles: a review. Journal of Physics D: Applied Physics, 39(11), R189.

[3]. Claesson, P. M., Ederth, T., Bergeron, V., & Rutland, M. W. (1996). Techniques for measuring surface forces. Advances in colloid and interface science, 67, 119-183.

[4]. Lau, A. W. C., Portigliatti, M., Raphaël, E., & Léger, L. (2002). Spreading of latex particles on a substrate. EPL (Europhysics Letters), 60(5), 717.

[5]. Brochard-Wyart, F., & de Gennes, P. G. (2003). Unbinding of adhesive vesicles. Comptes Rendus Physique, 4(2), 281-287.

[6]. Greiner, C., del Campo, A., & Arzt, E. (2007). Adhesion of bioinspired micropatterned surfaces: effects of pillar radius, aspect ratio, and preload. Langmuir, 23(7), 3495-3502.

[7]. Frey, M. T., Engler, A., Discher, D. E., Lee, J., & Wang, Y. L. (2007). Microscopic methods for measuring the elasticity of gel substrates for cell culture: microspheres, microindenters, and atomic force microscopy. Methods in cell biology, 83, 47-65.

[8]. Hertz, H. (1881). On the contact of elastic solids. J. reine angew. Math, 92(110), 156-171.

[9]. Lo, C. M., Wang, H. B., Dembo, M., & Wang, Y. L. (2000). Cell movement is guided by the rigidity of the substrate. Biophysical journal, 79(1), 144-152.

[10]. Jacot, J. G., Dianis, S., Schnall, J., & Wong, J. Y. (2006). A simple microindentation technique for mapping the microscale compliance of soft hydrated materials and tissues. Journal Of Biomedical Materials Research Part A, 79(3), 485-494.

[11]. Engler, A., Bacakova, L., Newman, C., Hategan, A., Griffin, M., & Discher, D. (2004). Substrate compliance versus ligand density in cell on gel responses. Biophysical journal, 86(1), 617-628.

[12]. Johnson, K. L., Kendall, K., & Roberts, A. D. (1971, September). Surface energy and the contact of elastic solids. In Proceedings of the Royal Society of London A: Mathematical, Physical and Engineering Sciences (Vol. 324, No. 1558, pp. 301-313). The Royal Society.

[13]. Style, R. W., Hyland, C., Boltyanskiy, R., Wettlaufer, J. S., & Dufresne, E. R. (2013). Surface tension and contact with soft elastic solids. Nature communications, 4.

[14]. Chakrabarti, A., & Chaudhury, M. K. (2013). Direct measurement of the surface tension of a soft elastic hydrogel: Exploration of elastocapillary instability in adhesion. Langmuir, 29(23), 6926-6935.

[15]. Jensen, K. E., Sarfati, R., Style, R. W., Boltyanskiy, R., Chakrabarti, A., Chaudhury, M. K., & Dufresne, E. R. (2015). Wetting and phase separation in soft adhesion. Proceedings of the National Academy of Sciences, 112(47), 14490-14494.

[16]. Lin, Y. Y., & Chen, H. Y. (2006). Effect of large deformation and material nonlinearity on the JKR (Johnson–Kendall–Roberts) test of soft elastic materials. Journal of Polymer Science Part B: Polymer Physics, 44(19), 2912-2922.

[17]. Long, J. M., & Wang, G. F. (2013). Effects of surface tension on axisymmetric Hertzian contact problem. Mechanics of Materials, 56, 65-70.

[18]. Xu, X., Jagota, A., & Hui, C. Y. (2014). Effects of surface tension on the adhesive contact of a rigid sphere to a compliant substrate. Soft Matter, 10(26), 4625-4632.

[19]. Cao, Z., Stevens, M. J., & Dobrynin, A. V. (2014). Adhesion and wetting of nanoparticles on soft surfaces. Macromolecules, 47(9), 3203-3209.

[20]. Salez, T., Benzaquen, M., & Raphaël, É. (2013). From adhesion to wetting of a soft particle. Soft Matter, 9(45), 10699-10704.

[21]. Hui, C. Y., Liu, T., Salez, T., Raphael, E., & Jagota, A. (2015, March). Indentation of a rigid sphere into an elastic substrate with surface tension and adhesion. In Proc. R. Soc. A (Vol. 471, No. 2175, p. 20140727). The Royal Society.

[22]. Carrillo, J. M. Y., & Dobrynin, A. V. (2012). Contact mechanics of nanoparticles. Langmuir, 28(29), 10881-10890.

[23]. Long, J., Wang, G., Feng, X. Q., & Yu, S. (2016). Effects of surface tension on the adhesive contact between a hard sphere and a soft substrate. International Journal of Solids and Structures, 84, 133-138.

[24]. Johnson, K. L., & Johnson, K. L. (1987). Contact mechanics. Cambridge university press.

[25]. Hui, C. Y., & Jagota, A. (2013). Surface tension, surface energy, and chemical potential due to their difference. Langmuir, 29(36), 11310-11316.

[26]. Long, J. M., & Wang, G. F. (2013). Effects of surface tension on axisymmetric Hertzian contact problem. Mechanics of Materials, 56, 65-70.

[27]. Vajpayee, S., Hui, C. Y., & Jagota, A. (2008). Model-independent extraction of adhesion energy from indentation experiments. Langmuir, 24(17), 9401-9409.

CHAPTER 6

SURFACE DEFORMATION OF AN ELASTIC SUBSTRATE IN CONTACT WITH A RIGID SPHERE: EFFECT OF SURFACE TENSION AND LARGE DEFORMATION*

Abstract

We study the profile of the substrate surface when a rigid sphere is pulled away from a thick compliant substrate. A finite element model is used to estimate surface deformation for given contact radius and indentation depth. Surface tension effect is implemented by a set of user-defined surface elements attached to the free surface of the substrate. An incompressible neo-Hookean material is used to account for material nonlinearity in large deformation setting. The finite element results are also used to fit the data collected from an experiment, where a glass sphere is pulled from a compliant PDMS gel.

---

* Xu, X., Jagota, A. and Hui, C.Y., (2016)

6.1 Introduction

The study of solid adhesion is of numerous practical implications, from the design of adhesives to understanding the interactions between cells or tissues in biological systems [1-4]. A common approach of modelling adhesive solid contact is to use the classical Johnson-Kendall-Roberts (JKR) theory [5]. However, recent experimental studies on some very compliant materials (with moduli on the order of kPa) such as hydrogels [6] and silicone gels [2, 7] showed considerable deviations from the JKR prediction. Theoretical analyses argue that such discrepancy can be attributed to the omission of the solid-air surface tension σ from the original JKR theory [8-12]. For a rigid sphere of radius R in contact with an elastic substrate of shear modulus μ, the importance of solid-air surface tension outside the contact can be characterized by the elastocapillary number $\alpha = \sigma/(\mu R)$. Small α favours elasticity and the contact behaviour approaches to that described by the JKR theory. Whereas large α favours surface tension, and the JKR theory fails to capture the correct contact mechanics.

Style *et al.* [2] have performed adhesive contact experiments by indenting rigid glass spheres onto thick silicone gel substrates. In the absence of external load, they reported a transition from an elasticity-dominant regime where the adhesion-driven deformation is primarily resisted by bulk elasticity to a surface-tension-dominant regime where the adhesion-driven deformation is primarily resisted by the substrate-air surface tension. This transition has also been captured by several numerical studies [9, 13]. In particular, Xu *et al.* [13] have created finite element models (FEM) to simulate Style *et al.*'s indentation test [2]. Their FEM models incorporated both the substrate-air surface tension and nonlinear-large deformation elasticity. They computed the energy release rate for the problem at zero external load and obtained approximate relations between contact radius

and sphere radius. Their numerical results are in good agreement with those reported in Style *et al.*'s experiment. Cao *et al.* [9] also reported a similar relation between a and R using molecular dynamics simulation.

This work is stimulated by a follow-up experiment to Style *et al.*'s performed by Jensen *et al.*, where a rigid glass sphere of radius R was brought into contact to a soft PDMS substrate with thickness much larger than R. The sphere was then retracted to reach different equilibrium positions and the surface profiles of the substrate were imaged (see Fig. 6.1a). A same experiment set-up was reported in Ref. 7. Here we use a sphere radius R = 17.4 μm, a shear modulus of the substrate μ = 1.9 kPa, a Poisson's ratio υ = ½ and the surface tension σ = 20 mN/m, consistent with the values reported in Ref. 7. Therefore the elasto-capillary number is $\alpha \sim 0.6$. Jensen *et al.* observed phase separation [7] of the PDMS gel in the vicinity of contact line, as illustrated schematically in Fig. 6.1b. Interestingly, the phase separation ceased to exist as the sphere was pulled to a higher extent, presumably due to retraction of liquid PDMS back into the solid network. The contact radius (measured at the liquid-sphere contact line if phase separation existed, see Fig. 6.1b) also decreased slightly as the sphere was pulled up. In this work, we attempt to model this experiment with finite element method (FEM) and predict the displacement profile of the substrate surface outside the contact region. The experiment details will be reported in a separate paper.

While most of the studies on the contact between a rigid sphere and an elastic substrate focus on the relation between contact radius a, indentation load P, and indentation displacement δ, very few studies focus on the displacement profile of the soft substrate outside the contact. In the original JKR theory, where substrate-air surface tension is neglected, one can compute the displacements

of the substrate surface outside the contact region by superimposing the Hertz displacement, the displacement due to a flat rigid punch and that under a tensile force [14]. The result is given in equation (6.1),

$$u_z^{JKR}(r) = -2\mu(1-\nu)\left(\frac{P_H - P}{\pi a}\right)\sin^{-1}\left(\frac{a}{r}\right) + \frac{a^2}{\pi R}\left[\sqrt{(r/a)^2 - 1} + \left(2 - \left(\frac{r}{a}\right)^2\right)\sin^{-1}\left(\frac{a}{r}\right)\right], \quad \frac{r}{a} > 1$$

(6.1)where $P_H = \frac{16a^3\mu}{3R}$ is the Hertzian load and ν the Poisson's ratio of the substrate. Hajji [15] and Gao *et al.* [16] extended the Boussinesq solution with the effect of surface stress on the elastic half space. However, their results cannot be expressed in closed form, such as that given by (6.1). In addition, the displacements in Jensen *et al.*'s experiments are comparable to the radius of the sphere, which brings into doubt the validity of using a small strain theory. As will be shown below, the small strain assumption limits their application to describe displacement profiles of the soft substrate surface. Here we use finite element method to accommodate the large deformation observed in Jensen *et al.*'s experiments. Our FEM set-up is similar to that used by Xu *et al.* [13].

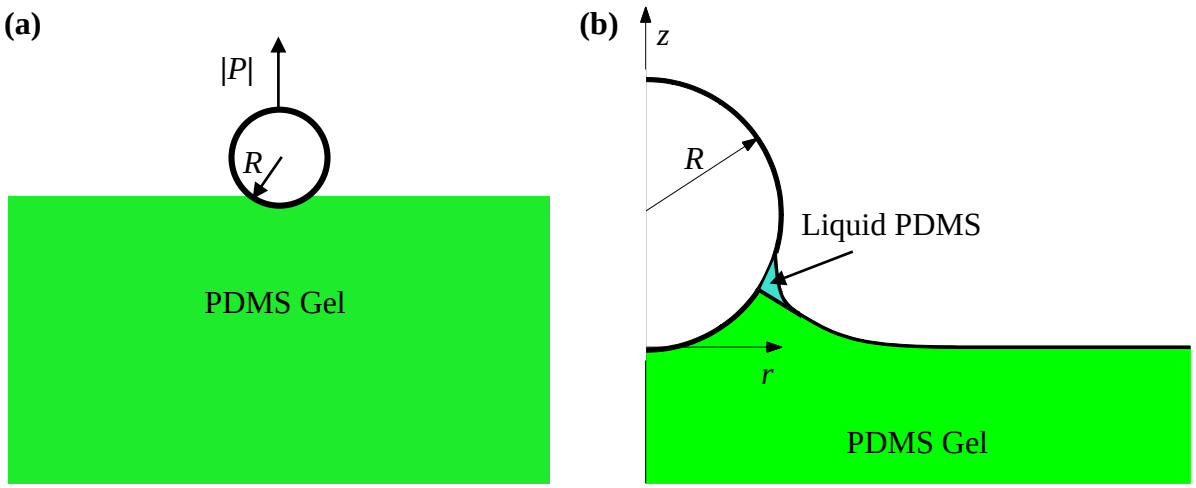

Figure 6.1. (a) Schematics of Jensen *et al.*'s experiments, where a rigid sphere is in contact of a soft PDMS gel. (b) A close-up view of the contact line, where phase separation of the substrate occurred.

6.2 Finite Element Model

To capture the nonlinear large deformation, we model the thick elastic substrate as an incompressible neo-Hookean half space, whose strain energy density W is given by

$$W = \frac{\mu}{2}(I_1 - 3) \tag{6.2}$$

where I_1 is the trace of Cauchy-Green strain tensor.

The substrate-air surface tension is introduced to the system by augmenting the finite element model with a set of user-defined axisymmetric 2-node linear surface elements [13], which discretize the free surfaces of the elastic half space. These user defined surface elements transmit surface tractions caused by the curvature of the deformed surface to the elastic bulk. In this study, we

assume isotropic and homogeneous substrate surface, in which surface stress can be represented by a single constant surface tension σ independent of surface deformation and composition. Since the contact radius in the experiment only varied slightly as the sphere is pulled up, we assume a no-slip contact condition.

To simulate adhesive contact, we employed the following loading scheme: (step 1) surface tension is applied incrementally to the surface elements and held at the final value σ in the subsequent steps. No deformation occurs in this step as the substrate is a half space, and it is performed first as a matter of convenience; (step 2) a vertical load is applied incrementally on the north pole of the rigid sphere, pushing it into the elastic half space until a finite contact radius a is obtained; (step 3) the vertical load in the system is reduced incrementally to a final value of P (negative value of P indicates pulling force) while no separation of previously contacting nodes from the rigid surface is allowed. The no-slip boundary condition prohibits sliding of the contacting surfaces over each other. As a result the contact radius remains constant at a during the last step. Fig. 6.2 shows some typical deformations at the end of each step.

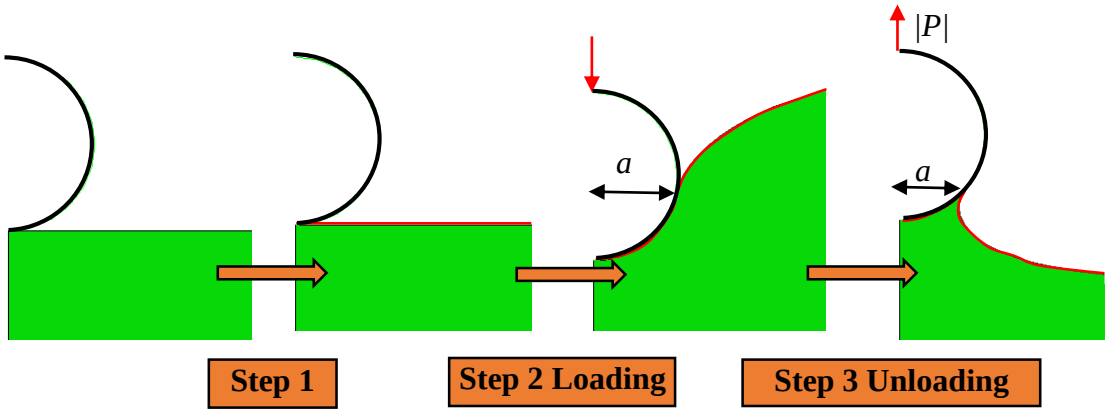

Figure 6.2. Deformation of the elastic parts after each loading step in a simulation with α = 0.6. The thin red layers on the free surface after step 1 symbolizes non-zero surface stress.

The effect of substrate-air surface tension on deformation profile of the substrate surface outside the contact can be illustrated in Fig. 6.3, where we plot the deformed substrate surfaces at different elasto-capillary number $\alpha = \sigma / \mu R$. In Fig. 6.3, the normalized contact radius is fixed at a/R = 0.75 and the normalized indentation displacement is δ/R = 0.31 (to be consistent with the experiment, we take δ>0 upwards even though an upward force is negative in FEM simulation). Fig. 6.3 shows that increasing α results in a more gradual decrease in vertical displacement as it moves away from the contact line, suggesting a stiffer interface between the soft substrate and air. This is to be expected, since increasing surface tension adds resistance.

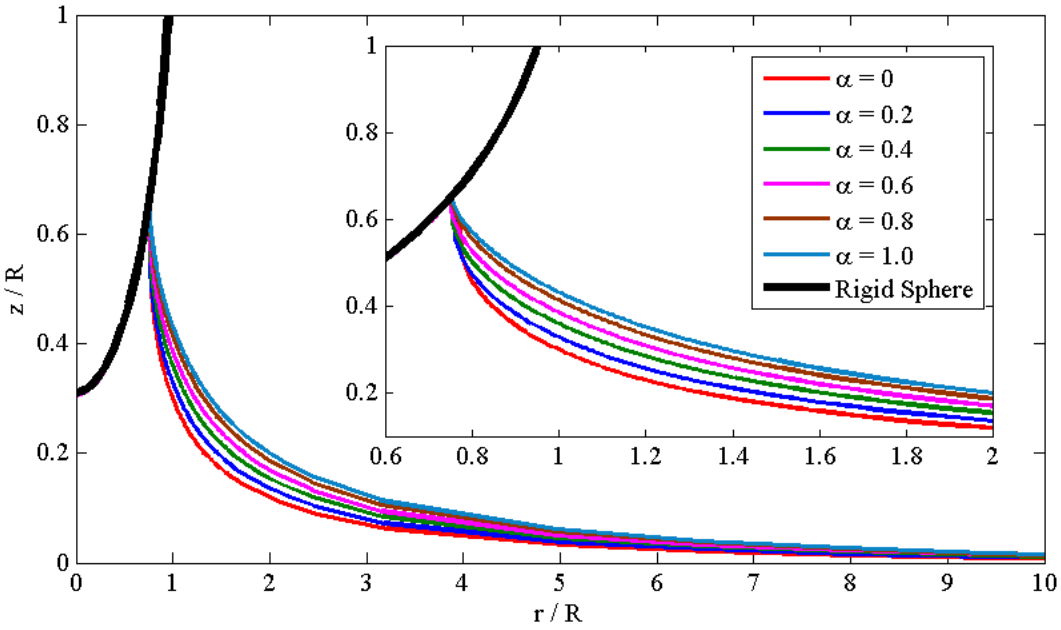

Figure 6.3. FEM results of the deformed substrate surface profiles at various values of the elasto-capillary number α at a/R = 0.75 and δ/R = 0.31.

In addition to the elasto-capillary number α, the deformed surface profile outside the contact is also sensitive to the contact radius and indentation displacement. Experimentally, it is challenging to precisely determine the position of contact line. This is particularly true if phase separation

occurs, where two different contact lines present (liquid PDMS-sphere contact line and solid PDMS-sphere contact line). From a computational perspective, our model assumes a homogeneous elastic substrate and hence cannot model the phase separation at the contact line observed in Jensen et al.'s experiment. It is therefore important to understand the sensitivity of the FEM deformed profile to variations of contact radius and indentation displacement. Results are shown in Fig. 6.4 and 6.5 for $\alpha=0.6$. Fig. 6.4 shows the change in surface displacement when the contact radius is varied by ±5%. This corresponds to an error of approximately ±0.5 μm in contact radius in Jensen *et al.*'s experiment. Similarly, Fig. 6.5 shows the change in surface displacement when the indentation displacement is varied by ±5%, corresponding to about ±0.2 μm in indentation displacement in the experiment. The surface of the sphere is indicated by black lines in the figures. The solid magenta lines in both figures correspond to no variations where $a/R = 0.75$ and $\delta/R = 0.31$ (Fig. 6.4a, 5) and $\delta/R = 1$ in Fig. 6.4b. A comparison between Fig. 6.4 and 6.5 shows that the FEM displacement profile is much more sensitive to the contact radius (Fig. 6.4) than indentation displacement (Fig. 6.5). In both cases, these variations only affect the surface profiles close to the contact line.

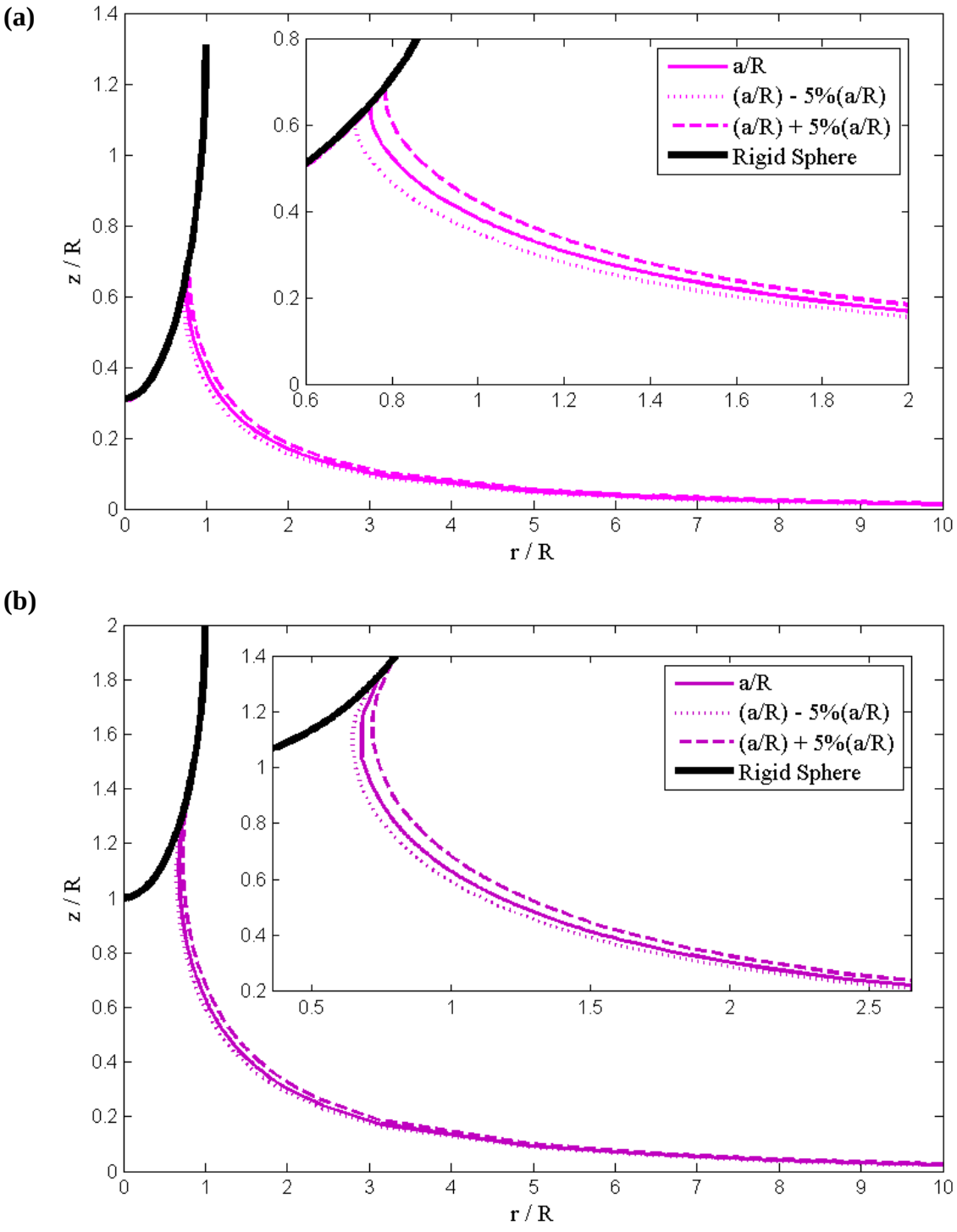

Figure 6.4. FEM deformed substrate surface profiles at $\alpha = 0.6$. The normalized contact radius is varied at ±5% of $a/R = 0.75$ and the indentation displacements are (a) $\delta/R = 0.31$; (b) $\delta/R = 1$.

The rigid sphere surface is indicated by the black line and the solid magenta line corresponds to no variations in a/R = 0.75. The inset is a close-up view of the local surface displacement profiles.

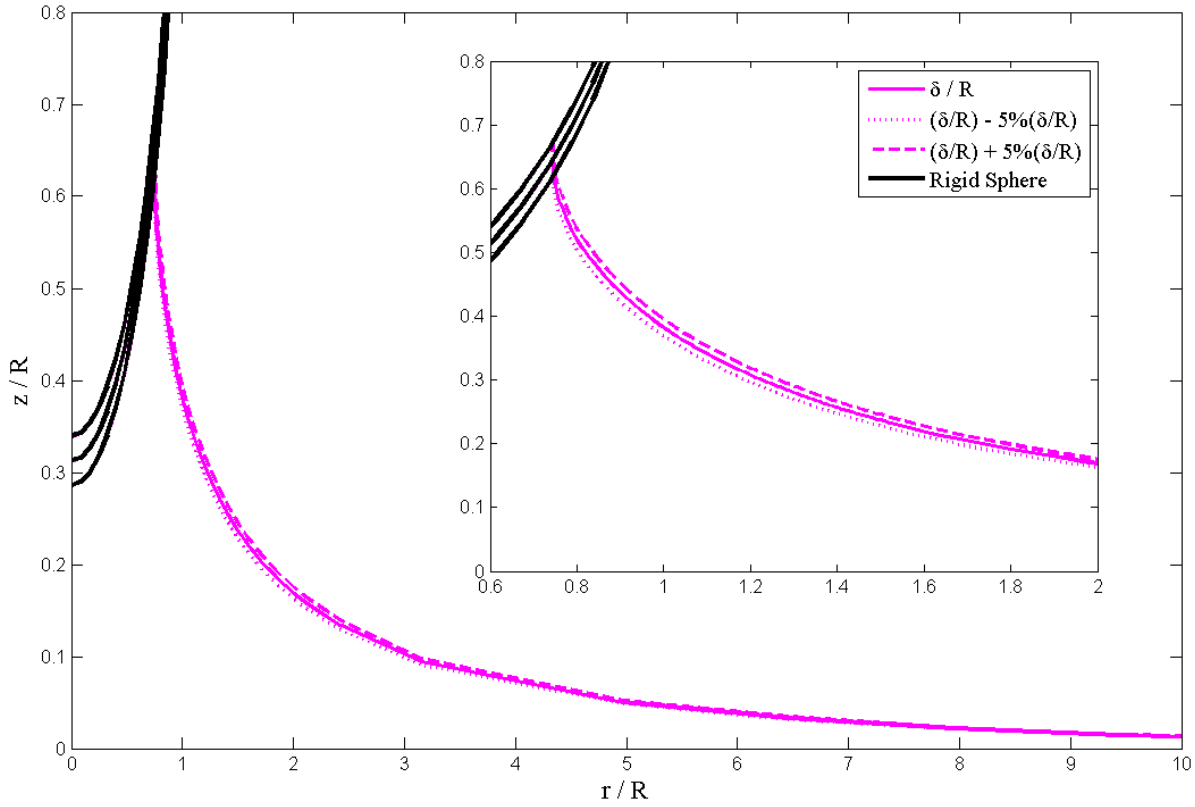

Figure 6.5. FEM results of the deformed substrate surface profiles at α = 0.6 and a/R = 0.75. The normalized sphere displacement is varied ±5% of δ/R = 0.31. The rigid sphere surfaces are indicated by the black lines and the solid magenta line corresponds to no variations in δ/R = 0.31. The inset is a close-up view of the local surface displacement profiles.

Since the effect of contact radius and indentation displacement is confined to the vicinity of the contact line, our FEM should give accurate predictions on the surface displacement at distances more than one spherical radius away from the contact line. In Jensen *et al.*'s experiment, as the sphere was pulled up, phase separation at the contact line ceased to exist and the contact radius slowly decreased. Hence in our FEM, we use the minimum measured contact radius $a_{min} \sim 0.75R$ (measured at the highest pulling force) for all sphere displacements, assuming the solid PDMS-

sphere contact line stays at $a/R = a_{min}/R$ during pulling. We attribute the discrepancies between the actual measured contact radius and a_{min} to phase separation. This assumption is consistent with the no slip boundary condition used in our simulation.

6.3 Results

Fig. 6.6 shows the predicted surface profiles at twelve different positions to which the sphere is pulled. We carry out the FEM simulations with two elasto-capillary numbers $\alpha = 0$ and $\alpha = 0.6$, representing the substrate to have zero surface tension or the same surface tension as its liquid phase respectively. Together with FEM results, we also plot the predictions made by the original JKR theory without surface tension (equation 6.1) as well as the numerically computed displacement profile based on the small strain theory (SST) proposed by Hui *et al.* [8], which extends JKR theory to include surface stress outside the contact.

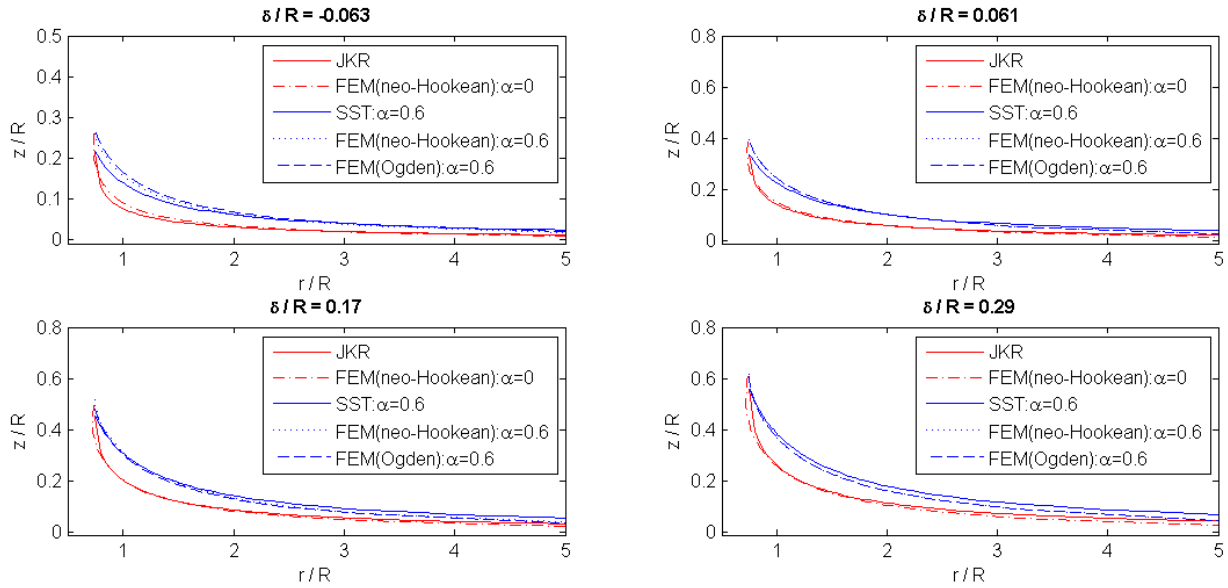

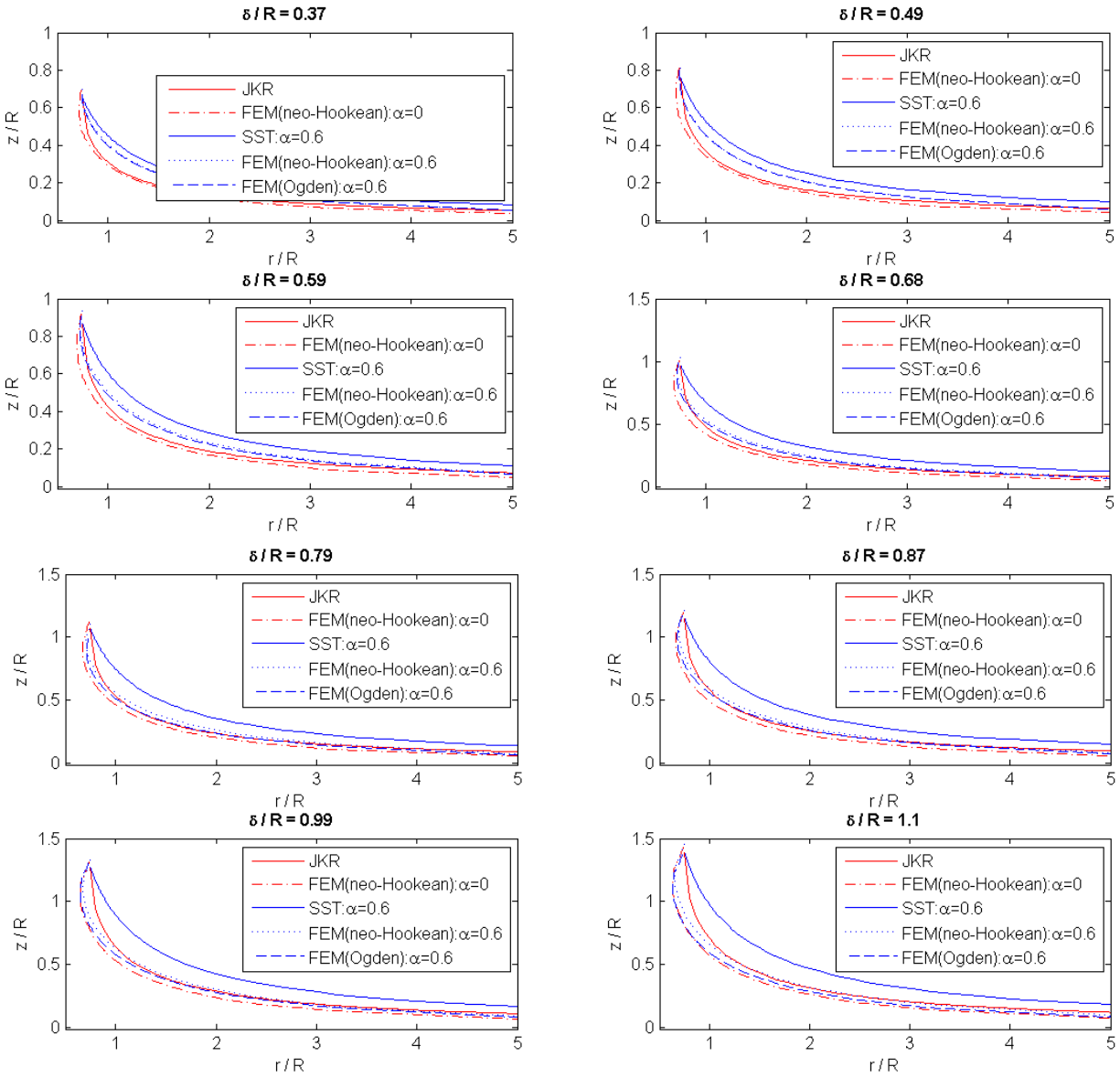

Figure 6.6 Comparison of the deformed surface profiles predicted by JKR theory without surface tension (red solid line), Hui et al.'s small strain modified JKR theory with surface tension (SST, blue solid line), FEM with neo-Hookean material at α = 0 (red dash-dot line), FEM with neo-Hookean material at α = 0.6 (blue dotted line) as well as FEM with Ogden material at α = 0.6 (blue dashed line). The contact radius is fixed at $a/R = a_{min}/R = 0.75$ in all calculations, where a_{min} is the minimum contact radius observed in the experiment at the highest sphere position. The sphere is pulled up from left to right, top to bottom.

In Jensen *et al.*'s experiment [7], the substrate surface showed a necking surface profile close to the contact line, where two material points on the deformed surface occupy the same radial position. The necking region is not predicted by the original JKR theory nor by Hui *et al.*'s small strain modified JKR theory. The surface profiles predicted using a neo-Hookean material model at α = 0.6 in FEM exhibit necking only when $\delta/R > 0.6$. However in Jensen *et al.*'s experiments [7], necking was observed even at small δ/R, suggesting that the neo Hookean material model is stiffer than the PDMS gel, i.e. some sort of local strain softening is needed to produce the neck region observed in experiments. In other words, increasing the strain hardening behaviour of the substrate or using surface tension which increases with surface stretch will exaggerate the difference between simulations and experiments. Kim *et al.* [17] have shown that the second-order Ogden model is preferable for analysing the PDMS structure. Hence we repeat our FEM simulations using an incompressible second-order Ogden material model (see Appendix 6) which is strain softening. The strain energy density of this Ogden material is

$$W_{Ogden} = \frac{\mu}{4}\left(\lambda_1^2 + \lambda_2^2 + \lambda_3^2 - 3\right) + \mu\left(\lambda_1 + \lambda_2 + \lambda_3 - 3\right) \tag{6.3}$$

At α = 0.6, both materials gives similar surface profiles (Fig. 6.6) at lower pulling positions $\delta/R <$ 0.5. However as the sphere is pulled to higher positions, the strain softening Ogden material model predicts larger necking regions close to the contact line and hence may produce surface profiles closer to the experimental results.

6.4 Discussion

In this work, we use finite element method to predict surface displacement outside the contact between a rigid sphere and a soft substrate. We also attempt to qualitatively compare the FEM results to the results of an experiment performed by Jensen *et al.*[7], in which a glass sphere is lifted from a very compliant PDMS gel. The JKR theory and Hui *et al.*'s small strain theory [8] are also assessed to predict the profile and results are compared with the FEM results. In general, based on the deformation predicted close to the contact line, the FEM results seems to qualitatively fit the experimental data better than small strain theories, especially when a strain softening 2nd order Ogden material is used.

The comparison with experiments is not without difficulties. The Ogden material model used in our FEM simulation is only a conjecture. More mechanical tests on the gel are required to fit the material parameters in a more appropriate Ogden model. Our FEM shows that surface deformation outside the contact is very sensitive to contact radius, which can be difficult to measure with a high degree of accuracy. In addition, phase separation was observed at the contact line, hence it is difficult to determine the exact location of solid-solid contact, notwithstanding that our model do not account for phase separation. Finally, it is likely that a small amount of slip can take place near the contact line and again it is difficult to be accounted for in our FEM model.

Acknowledgements

We thank Katharine E. Jensen and Eric R. Dufresne for providing their experimental data and helpful discussions and comments. This work was supported by the U.S. Department of Energy, Office of Basic Energy Sciences, Division of Materials Sciences and Engineering under Award DE-FG02-07ER46463.

Appendix 6 Supplementary Information

The incompressible 2nd order Ogden model. We used an incompressible second order Ogden material model for the elastic substrate. The strain energy density of such material is

$$W = \frac{\mu}{4}\left(\lambda_1^2 + \lambda_2^2 + \lambda_3^2 - 3\right) + \mu\left(\lambda_1 + \lambda_2 + \lambda_3 - 3\right) \tag{A.6.2}$$

where λ_i's are the stretch ratios and μ the initial shear modulus.

Considering a uniaxial test on this material, incompressibility gives

$$\lambda_1 = \lambda, \quad \lambda_2 = \lambda_3 = \frac{1}{\sqrt{\lambda}} \tag{A.6.3}$$

First Piola Kirchhoff stress **P** is

$$\mathbf{P} = -p\mathbf{F}^{-T} + \frac{\partial W}{\partial \mathbf{F}} \tag{A.6.4}$$

where **F** is the deformation gradient.

Assuming all the other components of P_{ij} are zero except P_{11}, where by equilibrium,

$$P_{11} = P, P_{22} = 0, P_{33} = 0 \tag{A.6.5}$$

Thus
$$\frac{p}{\lambda_2} + \frac{\partial W}{\partial \lambda_2} = 0 \Rightarrow p = -\lambda_2 \frac{\partial W}{\partial \lambda_2}$$
$$P = \frac{-\lambda_2}{\lambda}\frac{\partial W}{\partial \lambda_2} + \frac{\partial W}{\partial \lambda} = -\frac{1}{\lambda^{3/2}}\frac{\partial W}{\partial \lambda_2} + \frac{\partial W}{\partial \lambda} \tag{A.6.6}$$

Substituting equation (A.6.2) into (A.6.6), we obtain the relation between pressure P and stretch ratio λ in equation (A.6.7) and plot it in Fig. A.6.1.

$$P = \mu\left(-\frac{1}{2\lambda^2} - \frac{1}{\lambda^{3/2}} + \frac{\lambda}{2} + 1\right) \tag{A.6.7}$$

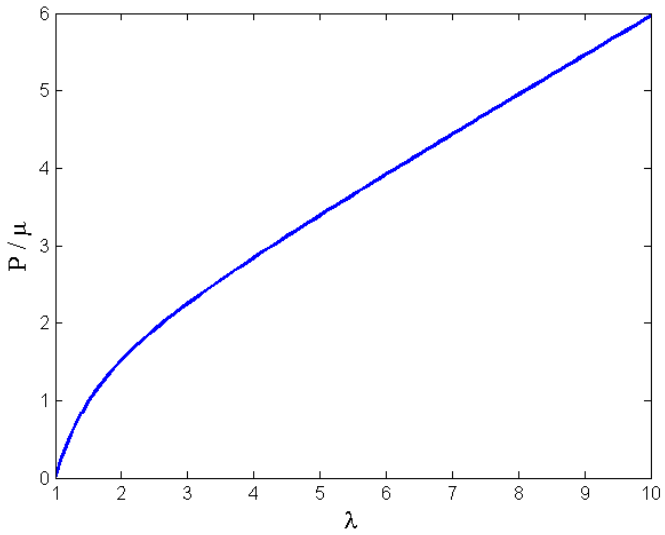

Figure A.6.1. Plot of normalized stress against stretch ratio in a uniaxial tensile test of the 2nd order Ogden model.

Mean curvature (H) of the deformed surface outside contact. The mean curvatures of lower pulling cases in Jensen *et al.*'s [7] experiments exhibit some plateaus close to the contact line. We compute the mean curvature of the surface profiles at $a/R = 0.75$ and $\delta/R = 0.31$ predicted by FEM using a neo-Hookean material model with different values of α (in Fig. A.6.2). To do so, we first fit the profile with an 8th order polynomial $z_{fit}(r)$. Then we compute the local mean curvature $H(s)$ of the fitted profile, where s is the arc length calculated from the contact line. Clearly, there is no sign of a possible plateau feature in the FEM (neo-Hookean) results.

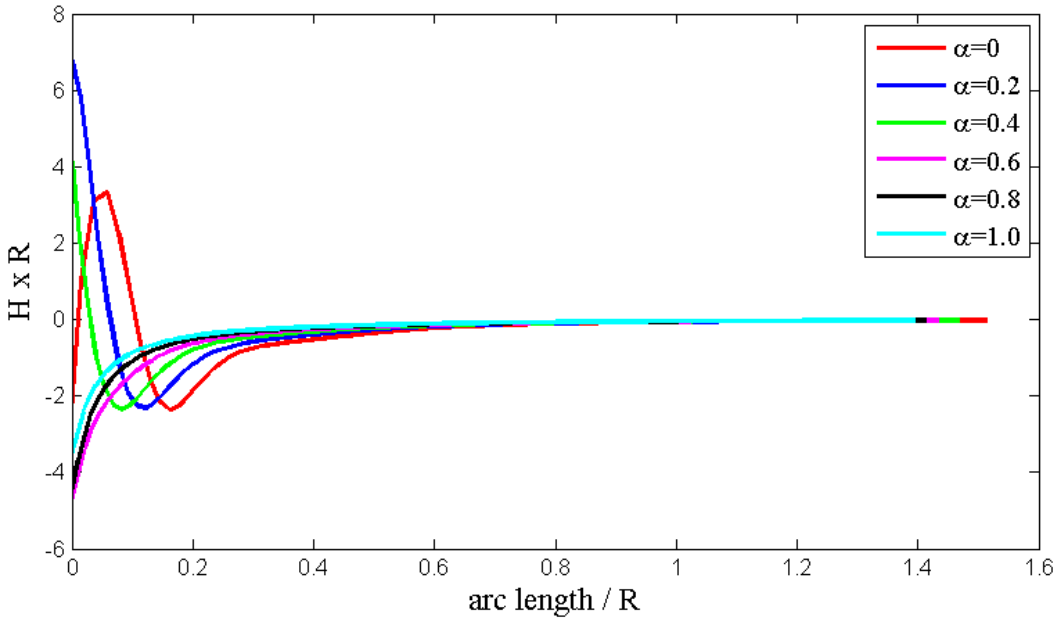

Figure A.6.2. Normalized mean curvatures as a function of normalized arc length of the FEM results at $a/R = 0.75$ and $\delta/R = 0.31$

References

[1]. Shull, K. R. (2002). Contact mechanics and the adhesion of soft solids. Materials Science and Engineering: R: Reports, 36(1), 1-45.

[2]. Style, R. W., Hyland, C., Boltyanskiy, R., Wettlaufer, J. S., & Dufresne, E. R. (2013). Surface tension and contact with soft elastic solids. Nature communications, 4.

[3]. Liu, K. K. (2006). Deformation behaviour of soft particles: a review. Journal of Physics D: Applied Physics, 39(11), R189.

[4]. Brochard-Wyart, F., & de Gennes, P. G. (2003). Unbinding of adhesive vesicles. Comptes Rendus Physique, 4(2), 281-287.

[5]. Johnson, K. L., Kendall, K., & Roberts, A. D. (1971, September). Surface energy and the contact of elastic solids. In Proceedings of the Royal Society of London A: Mathematical, Physical and Engineering Sciences (Vol. 324, No. 1558, pp. 301-313). The Royal Society.

[6]. Chakrabarti, A., & Chaudhury, M. K. (2013). Direct measurement of the surface tension of a soft elastic hydrogel: Exploration of elastocapillary instability in adhesion. Langmuir, 29(23), 6926-6935.

[7]. Jensen, K. E., Sarfati, R., Style, R. W., Boltyanskiy, R., Chakrabarti, A., Chaudhury, M. K., & Dufresne, E. R. (2015). Wetting and phase separation in soft adhesion. Proceedings of the National Academy of Sciences, 112(47), 14490-14494.

[8]. Hui, C. Y., Liu, T., Salez, T., Raphael, E., & Jagota, A. (2015, March). Indentation of a rigid sphere into an elastic substrate with surface tension and adhesion. In Proc. R. Soc. A (Vol. 471, No. 2175, p. 20140727). The Royal Society.

[9]. Cao, Z., Stevens, M. J., & Dobrynin, A. V. (2014). Adhesion and wetting of nanoparticles on soft surfaces. Macromolecules, 47(9), 3203-3209.

[10]. Salez, T., Benzaquen, M., & Raphaël, É. (2013). From adhesion to wetting of a soft particle. Soft Matter, 9(45), 10699-10704.

[11]. Carrillo, J. M. Y., & Dobrynin, A. V. (2012). Contact mechanics of nanoparticles. Langmuir, 28(29), 10881-10890.

[12]. Long, J., Wang, G., Feng, X. Q., & Yu, S. (2016). Effects of surface tension on the adhesive contact between a hard sphere and a soft substrate. International Journal of Solids and Structures, 84, 133-138.

[13]. Xu, X., Jagota, A., & Hui, C. Y. (2014). Effects of surface tension on the adhesive contact of a rigid sphere to a compliant substrate. Soft Matter, 10(26), 4625-4632.

[14]. Maugis, D. (2013). Contact, adhesion and rupture of elastic solids (Vol. 130). Springer Science & Business Media.

[15]. Hajji, M. A. (1978). Indentation of a membrane on an elastic half space. Journal of Applied Mechanics, 45(2), 320-324.

[16]. Gao, X., Hao, F., Fang, D., & Huang, Z. (2013). Boussinesq problem with the surface effect and its application to contact mechanics at the nanoscale. International Journal of Solids and Structures, 50(16), 2620-2630.

[17]. Kim, T. K., Kim, J. K., & Jeong, O. C. (2011). Measurement of nonlinear mechanical properties of PDMS elastomer. Microelectronic Engineering, 88(8), 1982-1985.

CHAPTER 7

RECOMMENDATION FOR FUTURE WORK

The work described in this dissertation has been concerned with the effect of surface tension, especially the solid-air surface tension, on deformation of soft solids. Although the results presented here have demonstrated that the role of surface tension becomes significant when the solid is compliant and the length scale is small, it could be further studied in a number of ways:

Using the current finite element model to study solid contact angle. This is an on-going project, which studies the relations between elasto-capillary number and the solid contact angle. We use finite element models to simulate a spherical soft solid placed on a rigid plate and deformed by both gravitational load and the adhesion between the sphere and the plate surfaces. Experimentally, a very soft hydro-gel sphere is placed on glass slides with surfaces chemically treated to exhibit different hydrophobicity.

Extending the finite element model to include strain-dependent surface stress. All the finite element results present in this work are under the assumption that the surface stress is constant and isotropic, independent of the deformation. This may not be true in general (see Hui & Jagota, *Langmuir* 2013). By incorporating a strain-dependent surface stress in the user-defined surface elements, we could obtain some interesting results.

Extending thin film indentation test to compressible materials. A correct treatment of elasto-capillarity requires distinguishing between the surface energy and the surface stress. It has been pointed out that the compressibility of the interfacial region, through the Poisson ratio near the interface, determines the difference between surface stress and surface energy. If we could extend the indentation test and analysis to thin films of compressible solids, it may help to experimentally verify the statement.

Improving the mesh density of our finite element model to study the stress field close to a contact line. We are interested in the effect of surface tension on the stress field in proximity to a contact line. By refining the existing finite element model of the contact geometry, we could get some more reliable results.